Title
Anion Photoelectron Spectroscopy of Exotic Species

Author
Yen, Terry A.

Publication Date
2010

Peer reviewed|Thesis/dissertation

Anion Photoelectron Spectroscopy of Exotic Species

By

Terry A. Yen

A dissertation submitted in partial satisfaction

of the requirements for the degree of

Doctor of Philosophy

in

Chemistry

in the

GRADUATE DIVISION

of the

UNIVERSITY OF CALIFORNIA, BERKELEY

Committee in charge:

Professor Daniel M. Neumark, Chair

Professor Stephen R. Leone

Professor Dmitry Budker

Fall 2010

Anion Photoelectron Spectroscopy of Exotic Species

by

Terry A. Yen

Abstract

Anion Photoelectron Spectroscopy of Exotic Species

By

Terry A. Yen

Doctor of Philosophy in Chemistry

University of California, Berkeley

Professor Daniel M. Neumark, Chair

Anion photoelectron spectroscopy is performed on a variety of small, unstable species in both the gas and condensed phases. For the gas-phase studies, the properties of the astrophysically significant molecules C_3N^- and C_5N^- and the biologically meaningful deprotonated DNA nucleobases were investigated. Spectra of C_3N^- and C_5N^- were obtained at 283 nm using slow electron velocity-map imaging and at 213 nm using field-free time-of-flight, respectively. Adiabatic electron affinities for both species, a term value for the first excited state of C_5N, and vibrational frequencies for the degenerate cis and trans bending modes of C_3N were determined. Spectra of deprotonated thymine and deprotonated cytosine at 213 nm were obtained to explore their excited state dynamics to understand the photostability of DNA.

For the condensed phase studies, a new spectrometer, the liquid microjet apparatus, was assembled and used to measure the vertical binding energy of the solvated electron. A microjet flowing a salt solution intersects a laser at either 266 nm or 213 nm. Two photons from a single nanosecond laser pulse are used to first generate solvated electrons using charge-transfer-to-solvent excitation and to then eject them into vacuum, where they are detected using field-free time-of-flight.

Contents

List of Figures

List of Tables

There is a subset of specially selected folks I want to graciously genuflect before and thank repeatedly for helping me keep the fraction of sanity I have remaining:

- Dan Neumark for his guidance and sharp intellect
- Michelle Haskins for being such a sweet gem, for always having an inspiring and positive attitude, for her constant supply of chocolate, and for being exceptionally helpful with all difficulties associated with purchase orders, repairs, bureaucratic logistics, etc.
- Natasha Vidangos for her friendship, the millions of pep-talk meals over the past five years, and her overabundant compassion, understanding and brilliant ability to pull jaw-droppingly beautiful, well-articulated ideas/statements out of her other end.
- Susan Rode for helping me improve my attitudes and mentality about life
- Alex Shreve for being my not-gay gay best friend and reason #2 for getting out of bed in the mornings. Reason #1 is the pumpkin chocolate chip muffins sold at the Coffee Lab.
- The guy who works at the Coffee Lab for saving me a pumpkin chocolate chip muffin every day and for being reason #1 for getting out of bed in the mornings.
- Brad(ley) Parsons for being an endearing jerk and one of the best teachers I've had
- Phil Simon and Eric Granlund (and the machinists at the machine shop) for being so patient with me and my inability to quickly grasp mechanical concepts
- Tara Yacovitch for her enthusiasm, the "Canadian-ness" aboot her, her vegan cookies, and for being next door so Alex and I can harass her for amusement
- Amy Brunsvold for being non-traditional in every possible way and for making my third year infinitely more enjoyable by "helping" me discover how much I enjoy cheap beer during the brief time she was with us before she found true love at Kip's
- Ingrid Chen for her limitless generosity, independence and bold self-assuredness
- Craig Schwartz for telling me to chill and for the expensive dinners (on his parents)
- Kim Kam for her ability to always see the good in everyone and her "jokes" that make me "chuckle" gleefully for hours on end
- Carrie Miller for her perpetual (and from my perspective, completely unfounded) belief in me
- Wendy DeTata for her boundless bubbliness and optimism
- Mrs. Pieters for her unconditional love and for being my penultimate role model

- Katie Dyl, Kathryn Hsu and Anna Sczaniecka for their faith, support, friendship and love
- Miling Yan for her inspiring unwavering self-confidence, sharp, no-nonsense wit that never ceases to amuse me, and for Pumpkin
- Mr. Pumpkin Yen the cat for being my super cuddly, highly annoying, little fuzzy buddy
- My mom and dad for giving birth to me; my sister Gail Yen for being born and alive and much more mature than I will ever be
- Baked goods of all kinds for giving me a reason to live
- Walgreen's for its dollar deals and 1 lb bags of M&Ms
- Wushu and Capoeira for making me not 100000" wide

THANK YOU THANK YOU SOOOO MUCH!!!!!!!

Chapter 1

Introduction

Anion photoelectron spectroscopy is an extremely versatile technique that provides invaluable insight into the structural and spectroscopic details of molecules, as demonstrated by the breadth of research presented here. The research described in later chapters is primarily focused on species that are particularly unstable, historically complicating efforts to study them experimentally. Many form stable negative ions and are thus very amenable to being probed by anion photoelectron spectroscopy, a method that lends itself to numerous applications due to its ability to probe neutral states with different multiplicities, its inherent mass selection capability and its ability to resolve vibrational features. The systems studied span over two states of matter, with some in the gas phase (C_3N^-, C_5N^-, deprotonated DNA nucleobases) and others in the condensed phase (the solvated electron), they require a wide range of photodetachment energies (ultraviolet wavelengths to vacuum ultraviolet wavelengths), and they represent an attempt to understand both important biological phenomena (photostability of DNA, radiation damage) and the fundamental conceptual issue of how the properties of matter evolve with size.

The following sections discuss the main motivations behind the works discussed. The principles of anion photoelectron spectroscopy are also outlined and their applications discussed. Chapter 2 highlights the operating principles of a new apparatus we built, the liquid microjet apparatus. This novel spectrometer opens up a fresh set of experimental capabilities for anion photoelectron spectroscopy as it makes its foray into studying condensed phase systems. Chapter 3 presents some preliminary results we obtained using the liquid microjet apparatus on the solvated electron in methanol. We measure its vertical binding energy (VBE) and discuss our initial results in the context of work performed on negatively charged methanol clusters and a recent measurement by another group of scientists. Chapter 4 covers our experiments using the negative ion photoelectron spectrometer on deprotonated thymine and cytosine. These experiments serve a dual purpose: (1) to elucidate the processes behind the photostability of DNA and (2) to prepare our spectrometer for future studies at high photon energies. Chapter 5 describes our attempt to generate vacuum ultraviolet light (118.2 nm). This chapter extends the modifications we made from the experiments described in the previous chapter by applying them to the study of indium phosphide clusters at high photon

energies. Finally, chapter 6 introduces a different class of systems, the carbon nitride clusters. Specifically, we analyze the photoelectron spectra of C_3N^- and C_5N^- obtained using two methods: our negative ion photoelectron spectrometer and the slow electron velocity-map imaging spectrometer. We determine adiabatic electron affinities of the neutral radicals, the term energy of the first excited state of C_5N, and vibrational frequencies for *cis* and *trans* bending modes of C_3N^-.

1.1 Anion photoelectron spectroscopy of solvated electrons

Solvated electrons, hailed as the simplest quantum solute [1], are important for two main reasons: (a) they play a significant role in radiation chemistry and biology [2], and (b) on a more fundamental level, they serve as benchmarks for understanding the physical and chemical basis of solvation. For example, solvated electrons in water, more commonly known as hydrated electrons, are formed in living cells by ionizing radiation and are highly reactive. Their existence leads to the formation of radicals, which have great potential for lethal genetic damage. Solvated electrons have different binding motifs, which once better understood, will provide new insights into the number of as yet poorly comprehended biological processes.

Until very recently, the energetics and dynamics of solvated electrons remained a mystery that could be only partly solved with complementary gas-phase studies on negatively charged clusters, where the excess electron is bound to a known number of solvent molecules. With the current experimental data dedicated to solvated electrons in bulk liquid, the energetics and relaxation timescales of solvated electrons have been estimated by extrapolation of the values observed for the negatively charged clusters. Not surprisingly, the values obtained using a wide variety of methods vary strongly with cluster size. Complicating matters, there is strong evidence for the existence of various binding motifs. Different experimental conditions produce different cluster isomers [3-10]. This coexistence of isomers is thus a confounding factor for an unambiguous extrapolation of experimental cluster properties to yield reliable values for bulk solvents. Another, even more central confounding factor is the following highly controversial issue of cluster science: how do we and can we extrapolate the properties of finite clusters to the bulk size regime? In the case of solvated electrons, the conceptual issue we aim to address by directly obtaining information about the solvated electron is thus to ascertain the "missing link" between clusters of the form $(S)_n^-$, where S is a solvent such as water or methanol, and the bulk solvated electron.

Directly measuring the energetics and relaxation timescales of solvated electrons has been tricky because spectroscopy proves most useful under high- or ultrahigh-vacuum conditions, which is seemingly incompatible with most liquids that have substantial vapor pressures. However, all this changed when Faubel developed the liquid microjet technique [11]. These jets function by forcing the liquid or solvent at high pressure through a very small orifice into the vacuum chamber. The surface area of the microjet is small enough such that the chamber can pull a reasonable vacuum with reasonably sized pumps.

The primary focus of the work described in Chapter 3 is on the direct determination of the vertical binding energy (VBE) of solvated electrons in methanol, that is, the energy needed to eject a solvated electron from the bulk methanol solvent into vacuum without a change in the solvent configuration. We have previously measured the VBE of the hydrated electron, which is described in A.T. Shreve's paper [12].

1.2 Anion photoelectron spectroscopy at 213 nm

Continuing along the theme expressed in Section 1.1, this section discusses our gas-phase efforts towards investigating how the electronic/vibrational structure of clusters evolves with size. Specifically, we wanted to examine indium phosphide (InP), which has become an important class of the III-V semiconductors because of their growing application in popular electronic and photonic devices. Experiments have been performed on small $In_xP_y^-$ cluster anions [13-16], but they have not yet revealed features that could be readily correlated to the bulk electronic structure. There are two possibilities to explain this lack of correlation: (1) the clusters studied are too small and (2) for the bare cluster anions studied in the photoelectron experiments, a large fraction of the atoms lie on the surface rather than the interior of the cluster, resulting in a large number of low-lying unoccupied surface states where the excess electron could reside. The crystalline structure of the bulk material is unlikely to be the one that is adopted by the bare cluster anions, since the surface atoms in the bulk are more prone to taking up bonding configurations that minimize the number of dangling bonds. With these considerations in mind, we decided to focus on probing the more strongly bound molecular orbitals in the bare clusters to see if there are any correlations with the valence band structure in the bulk InP. The initial study performed by Meloni, et al. [14] was extremely promising. To explore further and gain a more complete picture, higher photon energies, specifically 118.2 nm (10.5 eV), were required. Chapter 5 discusses our method of generating vacuum ultraviolet light.

In preparation for these high photon energy studies, we studied I_2^- at 213 nm (5.8 eV) [17], which is not described here. Chapter 4 gives a preliminary look at a high photon energy (213 nm, 5.8 eV) study of the deprotonated DNA nucleobases thymine and cytosine. This is an extension of previous work on these systems at 355 nm (3.5 eV) [18], which yielded electron affinities of the deprotonated radicals and the bond dissociation energy for the N – H bond that is broken, bringing new insight into the mechanism behind the irreducible single- and double-strand breaks ionizing UV radiation can cause to DNA. To further understand the profound biological consequences of UV-induced genetic damage and the photochemistry of DNA, new research at 213 nm was conducted on these deprotonated systems.

1.3 Anion photoelectron spectroscopy of cyanopolyacetylides

Circumstellar envelopes of evolved stars are chemically rich environments. They are created by extensive mass loss in the later stages of stellar evolution, which is caused by thermal pulses in the star interior and radiation pressure on dust [19, 20]. Due to the low temperature of the star and long timescales over which mass loss transpires, molecules and dust form in the envelopes and are gently blown into the interstellar medium (ISM). Nearly 80% of the mass of the ISM is material originating from these envelopes.

A wide range of physical conditions pervades circumstellar envelopes [21]. Near the stellar protosphere, the envelope material is all gaseous, found in dense concentrations ($n \sim 10^{10}$ cm^{-3}) and warm, with temperatures at approximately 1500 K. As one moves further away from the star core, expansion and cooling become prominent processes. Dust starts to form and beyond the dust formation zone, the temperature and density continue to drastically decrease such that at the outer edges of the envelope, temperatures are at approximately 25 K and densities at $n \sim 10^5$ cm^{-3} [22, 23]. The inner parts of the envelope are abundant with stable closed-shell species, while the outer parts, dominated by photochemistry from photons and cosmic rays, are flush with radical species.

These envelopes are especially common around asymptotic giant branch (AGB) stars and red supergiants (RSGs). AGB stars have low and intermediate initial mass with effective temperatures near 2000 – 3500 K. In the late stages of their lives, all the hydrogen in the stellar cores of these AGB stars has been converted to helium and the cores start to gravitationally contract [21]. The contraction ignites the hydrogen and the star enters its red giant branch phase. As the contraction continues, the envelope of the star expands and becomes convectively unstable. At a certain point, the helium making up the core ignites and the fusion of helium produces ^{12}C and ^{16}O in the core. Eventually, all the helium in the core is exhausted and all that is left behind is a oxygen- and carbon-rich core surrounded by helium- and hydrogen-burning shells. The helium shell ignites periodically, giving rise to what is called "thermal pulses", which aid in ejecting material from the star and creating the circumstellar envelope [24, 25]. Astonishingly, AGB stars lose up to 80% of their original mass to the circumstellar envelope.

Circumstellar envelopes are studied mainly by infrared and millimeter/submillimeter astronomy. Studies over the past several decades have yielded a wealth of chemical information. Thus far, over 50 different chemical species have been found in the envelope of the most well-known and brightest AGB star, IRC + 10216. The recent discoveries of the C_3N and C_5N radicals [26, 27] and of the C_3N^- and C_5N^- anions [28, 29] in the circumstellar envelope around IRC + 10216 have prompted much interest in characterizing the properties of the linear carbon chains of the type $C_{2n+1}N$. In particular, the C_3N radical and C_3N^- anion are key cyanopolyacetylides and important drivers of interstellar chemistry.

Chapter 6 describes our work on these two species. Isoelectronic and chemically similar to carbon hydride chains, which are discussed thoroughly in the thesis of S. M. Sheehan [30], there still remains much work to be done in the identification of various interstellar molecules. The study of vibrational and electronic spectroscopy of interstellar radicals thus continues to be an important component of astrophysical research, aiding in the observation of interesting chemical species in the universe.

1.4 Principles of anion photoelectron spectroscopy

Several detailed reviews of the technique of anion photoelectron spectroscopy have been written [31, 32], including those in the theses of S. M. Sheehan [30] and A. Weaver [33]. A brief summary is presented here.

1.4.1 Basic principles

The fundamental principle governing anion photoelectron spectroscopy is the photoelectric effect. An anion absorbs a photon with enough energy to overcome the attractive force binding the electron to the neutral core such that it ejects the electron:

$$M^- + h\nu \rightarrow M + e^- \tag{1}$$

where $h\nu$ is the photon energy and M^- and M are the negative ion and neutral species, respectively. The kinetic energy (eKE) of the emitted electron is given by the difference between the photon energy and its binding energy (eBE):

$$eKE = h\nu - eBE \tag{2}$$

The binding energy can be described as the transition energy between the initial state of the anion and the final state of the neutral molecules, or:

$$eBE = EA + E_{elec}^{(0)} + E_{rot}^{(0)} + E_{vib}^{(0)} - E_{elec}^{(-)} - E_{rot}^{(-)} - E_{vib}^{(-)} \tag{3}$$

where EA is the electron affinity and the $E_i^{(0)}$'s and $E_i^{(-)}$'s are the neutral and anion internal energies, respectively. For the experiments described in the later chapters, the rotational energies are ignored since they cannot be resolved in the spectra. By

measuring the kinetic energies of the photodetached electrons, we obtain information about the electronic and vibrational energies of the anion and neutral states involved in the transition.

Experimentally, we intersect a fixed-frequency laser with the system of interest, be it a liquid microjet or a beam of mass-selected anions. The kinetic energies of the detached photoelectrons are recorded and generally, most of the information we obtain from our spectra pertains to the neutral species, which oftentimes are short-lived, unstable species that form stable negative ions. Anion photoelectron spectroscopy thus has several advantages relative to other spectroscopic methods. In addition to not being limited to studying stable neutral molecules, using anion photoelectron spectroscopy allows us to mass-select the ion of interest, minimizing signal due to other ions. EA's, a fundamental quantity that is useful in thermochemical cycles, are reliably and precisely determined. Finally, the selection rules are more "relaxed" compared to those of optical spectroscopy; we can observe transitions to neutral electronic states of different spin multiplicity. For example, a triplet anion can produce both doublet and quartet neutral states. This last advantage of anion photoelectron spectroscopy stems from the tenet that the ejection of an electron is a one-electron process, with no further rearrangement of the electrons in the neutral core. Consequently, the selection rule for electron spin is $\Delta S = \pm 1/2$.

1.4.2 Analysis of anion photoelectron spectra

Two important quantities we are particularly interested in are the *adiabatic electron affinity* and the *vertical detachment energy* (or *vertical binding energy*). The adiabatic electron affinity of the neutral M is the energy required to make the transition from the (electronic, rotational and vibrational) ground state of the anion M^- to the (electronic, rotational, and vibrational) neutral ground state of the neutral M, or:

$$M^-(\mathrm{v}=0) + h\nu \rightarrow M(\mathrm{v}=0) + e^- \qquad (4)$$

All electron affinities mentioned in the later chapters are adiabatic electron affinities. The vertical detachment energy is defined as the difference between the (electronic, rotational and vibrational) ground state energy of the anion M^- and the neutral potential energy at the same internuclear distance.

Our spectra are analyzed using the Franck-Condon (FC) principle, which states that the ejection of an electron in a photodetachment process is very fast compared to the motion of the nuclei. That is, the neutral is formed with the nuclei in the same

configuration as in the parent anion state. As the neutral relaxes to its lowest-energy equilibrium geometry, the atoms oscillate about their equilibrium positions. Applying this principle along with the Born-Oppenheimer and rigid rotor approximations to the transition dipole moment integral, we obtain a term called the FC factor, which is the square of the overlap of the vibrational wavefunctions of the anion and the neutral:

$$\left|\left\langle \psi_{vib}^{(0)}(Q^{(0)}) \middle| \psi_{vib}^{(-)}(Q^{(-)}) \right\rangle\right|^2 \tag{5}$$

where the vibrational wavefunctions of the anion $\psi_{vib}^{(-)}(Q^{(-)})$ and neutral $\psi_{vib}^{(0)}(Q^{(0)})$ are functions of their respective normal coordinates $Q^{(-)}$ and $Q^{(0)}$. The FC factors determine the relative peak intensities of the photoelectron spectra. This is illustrated in Figure 1. The bottom axis represents the normal coordinate of a given vibrational mode. For an N-atom non-linear polyatomic molecule, there are 3N-6 vibrational modes; for an N-atom linear polyatomic molecule, there are 3N-5. The difference between the minima of the potential energy curves of the anion and neutral is the normal coordinate displacement, ΔQ. The FC intensity profile is sensitive to geometry and vibrational frequency changes between the anion and the neutral. Appreciable geometry changes between the anion and neutral (large changes in ΔQ) and/or in the vibrational frequencies result in extended progressions. The active vibrational modes will be those that resemble the movement of the nuclei. For example, if the bond angles are the same but the bond lengths have changed, then the stretching modes are excited. If there is no change in geometry between the anion and neutral ($\Delta Q = 0$), then only a sharp peak will appear in the photoelectron spectra, corresponding to the 0_0^0 transition.

Vibrationally excited anions, generated under some experimental conditions, can give rise to "hot band" transitions. These transitions are usually small in intensity and are found at higher eKE to the 0-0 band origin. They provide information about the energetics of the anion, though we aim to minimize them in our experiments to simplify our spectra, since they can cause spectral congestion and obfuscate the identification of band origins.

In addition to determining which modes are excited, we can also use FC factors to ascertain which quanta in each mode will be observed. For the totally symmetric vibrational ground state of the anion, the neutral vibrational wavefunctions that will give non-zero overlap integrals / FC factors are those representing all quanta of totally symmetric vibrations and only even quanta of non-totally symmetric vibrations.

To perform our FC simulations and analyze our photoelectron spectra, we use the simple harmonic oscillator model for the vibrational potentials. We make a further simplification, the "parallel mode approximation", which states that the normal modes in the anion and neutral are independent. The total wavefunction is then a product of 1-D vibrational wavefunctions ψ_i for the n vibrational modes of the molecule. If the system

has a significant degree of anharmonicity and its vibrational modes cannot be adequately represented by a harmonic model, then we can use the Morse oscillator model or if that also proves inadequate, we can model the vibrational potential with the appropriate function and calculate the vibrational wavefunctions, energies and FC factors numerically. Moreover, if the normal modes in the anion and neutral are sufficiently different, then a transformation between the modes in the anion ($Q^{(-)}$) and neutral ($Q^{(0)}$) must be taken into account, which is expressed as:

$$Q^{(-)} = \mathbf{J}Q^{(0)} + \mathbf{K} \tag{6}$$

This transformation includes the Duschinsky rotation, represented by the Duschinsky rotation matrix **J**, and is discussed in great depth in the thesis of S. M. Sheehan [30]. Briefly here, **K** is the normal coordinate displacement matrix containing the ΔQ's for each mode. In the parallel mode approximation, **J** is a unit matrix. When the frequencies and/or geometries change drastically between the anion and the neutral, then **J** has non-zero off-diagonal elements that cause mixing of the normal modes.

1.4.3 Photoelectron angular distribution

The angular distribution of photoelectrons for a one photon process is given by [34]:

$$\frac{d\sigma}{d\Omega} = \frac{\sigma_{\text{total}}}{4\pi}\left[1 + \frac{\beta}{2}(3\cos^2\theta - 1)\right] \tag{7}$$

where θ is the angle between the electric field of the laser and the direction of electron ejection, σ_{total} is the total photodetachment cross section, and β is the anisotropy parameter ($-1 < \beta < +2$). β provides information about the symmetry of the electronic orbital from which the electron was ejected and can thus be used to distinguish peaks in a photoelectron spectrum arising from different electronic transitions. The photodetachment selection rule is $\Delta l = \pm 1$. An electron detached from an *s* orbital ($l = 0$) becomes a *p* wave ($l = 1$) and gives a $\beta = 2$ and a $\cos^2\theta$ distribution. An electron detached from a *p* orbital ($l = 1$) can be either an *s* ($l = 0$) or *d* ($l = 2$) wave, which interfere to give a $\sin^2\theta$ distribution and a $\beta = -1$.

Depending on the detection method used to collect the photoelectrons, there are different ways to extract the angular information. For velocity-map imaging, the photoelectrons and their angular information are simultaneously collected and β can be obtained directly by fitting to Eqn 7. For other methods such as field-free time-of-flight, we collect photoelectrons in directions parallel and perpendicular to the electric field of the laser and use the following equation, where $I_{0°}$ and $I_{90°}$ are the peak intensities taken at θ = 0° and θ = 90° with respect to the laser polarization:

$$\beta = \frac{I_{0^\circ} - I_{90^\circ}}{\frac{1}{2} I_{0^\circ} + I_{90^\circ}} \tag{8}$$

References

1. Rossky, P.J. and J. Schnitker, *THE HYDRATED ELECTRON - QUANTUM SIMULATION OF STRUCTURE, SPECTROSCOPY, AND DYNAMICS.* Journal of Physical Chemistry, 1988. **92**(15): p. 4277-4285.
2. Sonntag, C.v., *The Chemical Basis of Radiation Biology*. 1987, London: Taylor and Francis.
3. Bragg, A.E., et al., *Hydrated electron dynamics: From clusters to bulk.* Science, 2004. **306**(5696): p. 669-671.
4. Coe, J.V., et al., *PHOTOELECTRON-SPECTROSCOPY OF HYDRATED ELECTRON CLUSTER ANIONS, (H2O)N-=2-69.* Journal of Chemical Physics, 1990. **92**(6): p. 3980-3982.
5. Coe, J.V., S.M. Williams, and K.H. Bowen, *Photoelectron spectra of hydrated electron clusters vs. cluster size: connecting to bulk.* International Reviews in Physical Chemistry, 2008. **27**(1): p. 27-51.
6. Hammer, N.I., et al., *How do small water clusters bind an excess electron?* Science, 2004. **306**(5696): p. 675-679.
7. Kammrath, A., et al., *Photoelectron imaging of large anionic methanol clusters: (MeOH)(n)(-) (n similar to 70-460).* Journal of Chemical Physics, 2006. **125**(17): p. 4.
8. Neumark, D.M., *Spectroscopy and dynamics of excess electrons in clusters.* Molecular Physics, 2008. **106**(16-18): p. 2183-2197.
9. Paik, D.H., et al., *Electrons in finite-sized water cavities: Hydration dynamics observed in real time.* Science, 2004. **306**(5696): p. 672-675.
10. Turi, L., W.S. Sheu, and P.J. Rossky, *Characterization of excess electrons in water-cluster anions by quantum simulations.* Science, 2005. **309**(5736): p. 914-917.
11. Winter, B. and M. Faubel, *Photoemission from liquid aqueous solutions.* Chemical Reviews, 2006. **106**(4): p. 1176-1211.
12. Shreve, A.T., T.A. Yen, and D.M. Neumark, *Photoelectron spectroscopy of hydrated electrons.* Chemical Physics Letters. **493**(4-6): p. 216-219.
13. Asmis, K.R., T.R. Taylor, and D.M. Neumark, *Electronic structure of indium phosphide clusters: anion photoelectron spectroscopy of InxPx- and Inx+1Px-(x=1-13) clusters.* Chemical Physics Letters, 1999. **308**(5-6): p. 347-354.
14. Meloni, G., et al., *Probing the connection between cluster and bulk electronic structure of InP using vacuum ultraviolet anion photoelectron spectroscopy.* Chemical Physics Letters, 2004. **392**(1-3): p. 90-94.
15. Rinnen, K.D., et al., *DIRECT INFRARED AND VISIBLE ABSORPTION-SPECTROSCOPY OF STOICHIOMETRIC AND NONSTOICHIOMETRIC CLUSTERS OF INDIUM-PHOSPHIDE.* Journal of Chemical Physics, 1992. **96**(6): p. 4088-4101.
16. Xu, C.S., et al., *ANION PHOTOELECTRON-SPECTROSCOPY OF SMALL INDIUM-PHOSPHIDE CLUSTERS (INXPY-X,Y=1-4).* Journal of Chemical Physics, 1994. **101**(6): p. 5406-5409.
17. Parsons, B.F., et al., *Photoelectron imaging of I-2(-) at 5.826 eV.* Journal of Chemical Physics, 2006. **125**(24): p. 6.

18. Parsons, B.F., et al., *Anion photoelectron imaging of deprotonated thymine and cytosine.* Physical Chemistry Chemical Physics, 2007. **9**(25): p. 3291-3297.
19. van Loon, J.T., et al., *An empirical formula for the mass-loss rates of dust-enshrouded red supergiants and oxygen-rich Asymptotic Giant Branch stars.* Astronomy & Astrophysics, 2005. **438**(1): p. 273-289.
20. Willson, L.A., *Mass loss from cool stars: Impact on the evolution of stars and stellar populations.* Annual Review of Astronomy and Astrophysics, 2000. **38**: p. 573-611.
21. Ziurys, L.M., *The chemistry in circumstellar envelopes of evolved stars: Following the origin of the elements to the origin of life.* Proceedings of the National Academy of Sciences of the United States of America, 2006. **103**(33): p. 12274-12279.
22. Keady, J.J., D.N.B. Hall, and S.T. Ridgway, *THE IRC +10216 CIRCUMSTELLAR ENVELOPE .1. MODELS FOR THE DUST AND GAS.* Astrophysical Journal, 1988. **326**(2): p. 832-842.
23. Truong, B., D. Morris, and Q.R. Nguyen, *CO (/b J/=1-0 and 2-1) mapping of IRC+10216: a hot core model for the gas kinetic temperature distribution and the mass-loss rate.* Astronomy and Astrophysics, 1991. **249**(2): p. 435-442.
24. Forestini, M. and C. Charbonnel, *Nucleosynthesis of light elements inside thermally pulsing AGB stars .1. The case of intermediate-mass stars.* Astronomy & Astrophysics Supplement Series, 1997. **123**(2): p. 241-272.
25. Herwig, F., *Evolution of asymptotic giant branch stars.* Annual Review of Astronomy and Astrophysics, 2005. **43**: p. 435-479.
26. Guelin, M., N. Neininger, and J. Cernicharo, *Astronomical detection of the cyanobutadiynyl radical C5N.* Astronomy and Astrophysics, 1998. **335**(1): p. L1-L4.
27. Guelin, M. and P. Thaddeus, *TENTATIVE DETECTION OF C3N RADICAL.* Astrophysical Journal, 1977. **212**(2): p. L81-L85.
28. Cernicharo, J., et al., *DETECTION OF C5N- AND VIBRATIONALLY EXCITED C6H IN IRC+10216.* Astrophysical Journal Letters, 2008. **688**(2): p. L83-L86.
29. Thaddeus, P., et al., *Laboratory and astronomical detection of the negative molecular ion C3N.* Astrophysical Journal, 2008. **677**(2): p. 1132-1139.
30. Sheehan, S.M. 2007.
31. Ervin, K.M. and W.C. Lineberger, *Photoelectron Spectroscopy of Molecular Anions*, in *Advances in Gas Phase Ion Chemistry*. 1992, JAI Press Inc. p. 121-166.
32. Chen, P., *Photoelectron Spectroscopy of Reactive Intermediates*, in *Unimolecular and Bimolecular Reaction Dynamics*, C.Y. Ng, T. Baer, and I. Powis, Editors. 1994, John Wiley & Sons Ltd. p. 372-425.
33. Weaver, A. 1991.
34. Cooper, J. and R.N. Zare, *ANGULAR DISTRIBUTION OF PHOTOELECTRONS.* Journal of Chemical Physics, 1968. **48**(2): p. 942-&.

Figure 1.1. Anion photoelectron spectroscopy

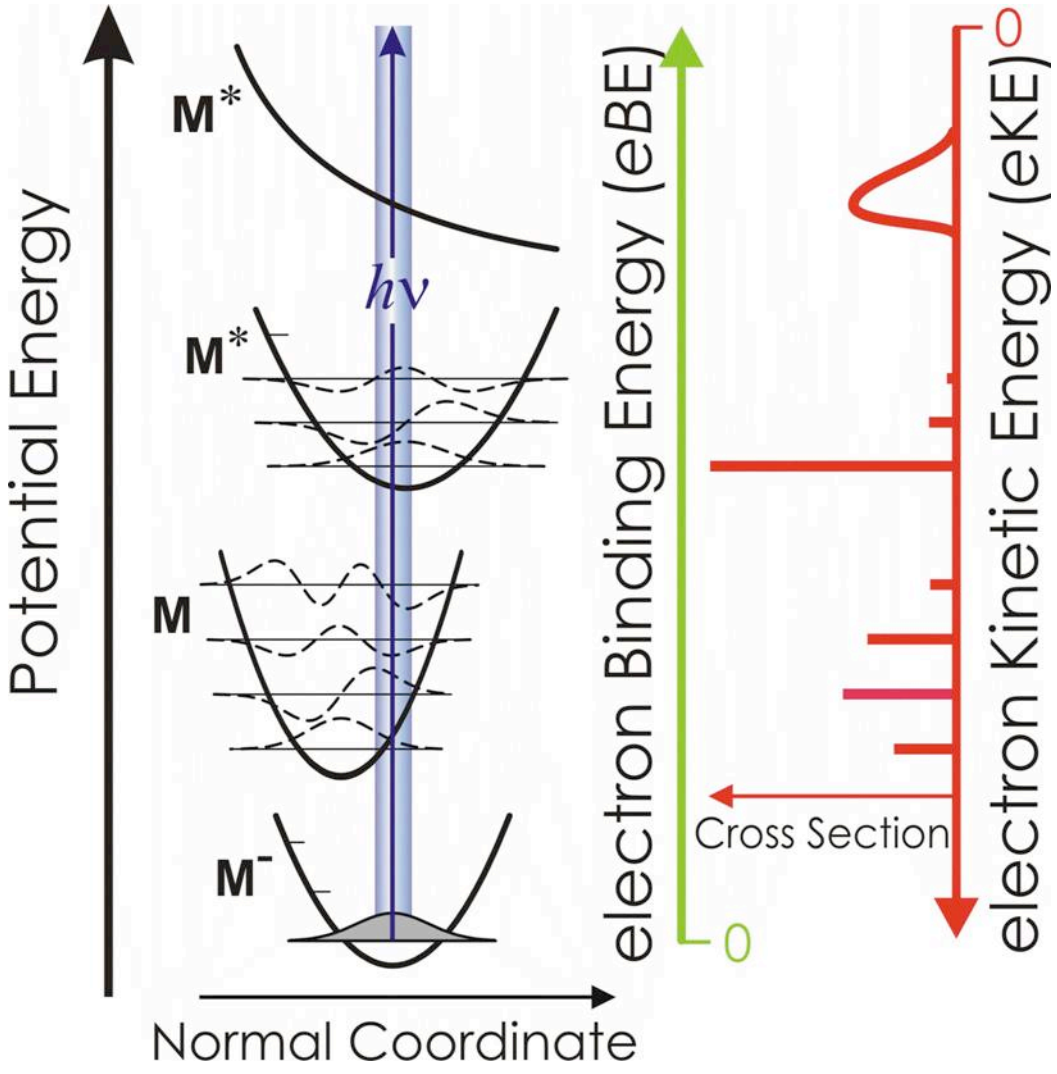

Chapter 2

Experimental section:

Liquid microjet apparatus and selected parts of the negative ion photoelectron spectrometer

LIQUID MICROJET APPARATUS

Our liquid microjet apparatus consists of a liquid jet source to produce solvated electrons, a fixed-frequency laser to both generate and detach the solvated electrons, a time-of-flight (TOF) chamber to detect the electrons and determine their electron kinetic energies, and a negative ion source to use for calibration.

A schematic diagram of the apparatus is shown in Figure 2.1. The microjet enters the chamber via a three-axis translation stage mounted on a feedthrough flange. The nozzle assembly is of the type developed by [1], consisting of a fused silica capillary clamped into polyether ether ketone (PEEK) tubing. Constant flow of a dilute salt solution through the nozzle is maintained by a syringe pump with an in-line filter to prevent clogging. The microjet intersects a pulsed nanosecond Nd:YAG laser. We use two photons from a single nanosecond pulse; the first creates a solvated electron via charge-transfer-to-solvent (CTTS) excitation of the dissolved anions, and the second ejects the electron into vacuum. Once in vacuum, the photoelectrons enter the TOF system through a skimmer. They travel through a field-free drift tube to a chevron mounted, dual microchannel plate detector. The electron flight times are collected and averaged on a digital oscilloscope and analyzed by a computer.

For calibration, we use the ion source and mass spectrometer parts of the negative ion photoelectron spectrometer that has been described in detail previously [2-5]. Briefly, the anion precursor, diluted in a noble gas carrier, is expanded into the source region through a pulsed valve. Anions are formed in the supersonic expansion by dissociative electron attachment. They are extracted into a linear reflectron mass spectrometer, guided by three sets of deflectors and focused by a cylindrical electrostatic Einzel lens. Upon intersection with a Nd:YAG photodetachment laser, electrons are detached, passed through a skimmer and collected with the TOF system used as part of the liquid jet apparatus. The current negative ion photoelectron spectrometer has been modified, however, such that we detect the detached electrons along an axis that is collinear to the direction of the propagation of the parent ions.

In this chapter, the operating principles behind each component will be discussed.

2.1 Liquid jet source

PES of liquids is complicated by the fact that photoelectron energy analyzers, regardless of design, work best under high vacuum or ultrahigh vacuum conditions, seemingly incompatible with the many liquids of interest that have substantial vapor pressures. PES of water and ions in aqueous solutions was only made possible through the development of liquid microjets by Faubel [6, 7]. This section describes this technique in detail.

After a description of the theory and construction of the liquid microjet, I will discuss how we generate and detach solvated electrons.

2.1.1 Principles

The liquid microjet is formed by forcing liquid at high pressure through an orifice with diameter d into a vacuum chamber. By having d comparable to or smaller than the mean free path λ in the equilibrium vapor, we satisfy the Knudsen condition, $\lambda > d$, for effusive flow from a molecular beam source [6]. This way, the jet acts as an effusive source of vapor molecules into a nearly collisionless environment. Larger diameter jets are surrounded by a sheath of vapor at the equilibrium vapor pressure. The mean free path in the vapor is given by [8]

$$\lambda[\mathrm{cm}] = \frac{c}{p_v[\mathrm{Torr}]} \tag{1}$$

where p_v is the equilibrium vapor pressure and c represents [8]

$$c[\mathrm{Torr}\cdot\mathrm{cm}] = \frac{kT}{\left(\frac{1}{3}+\frac{2}{3}\sqrt{2}\right)\pi\sigma^2} \tag{2}$$

with k representing Boltzmann's constant in Torr cm^3 K^{-1}, T the temperature in Kelvin, and $\pi\sigma^2$ is the collision cross-section. For water at the freezing point, c = 0.0053 Torr cm.

The jet can be approximated as a cylindrical line source divided into three separate flow regimes [6]. The first region is the liquid surface, where we assume the evaporating molecules have a Maxwellian velocity distribution. In the second region (the dense gas phase), the vapor expands radially. The mean free path in this regime is comparable to or smaller than the radius of this region. In the third region (the far flow field), the mean free path is much larger than the radius of the second region and we expect free molecular flow.

The goal is to reduce the effect of collisions in the dense gas region (the second region) as much as possible. One approach is to make the diameter d of the jet very small; another is to introduce a skimmer into this region near the liquid core. The skimmer changes the geometry of the flow field from cylindrical to spherical and the decrease in vapor density goes from a $\frac{1}{r}$ drop to a $\frac{1}{r^2}$ drop once past the skimmer.

We can estimate the overall collision frequency in the second region by calculating the effective vapor layer thickness using [6]

$$\mu = n_0 r_0 \ln\left(\frac{r}{r_0}\right) \tag{3}$$

where μ is the effective vapor layer thickness, r_0 the radius of the jet, r the distance from the center of the jet to the skimmer entrance and n_0 the local equilibrium vapor density at the jet surface. Under our typical experimental conditions for running a 30 μm water jet, with an estimate of 6.5 – 8.0 Torr for the equilibrium vapor pressure [9], we find our

effective vapor thickness to be between 0.038 and 0.055 Torr cm. Using Eqn (1), this effective vapor thickness corresponds to about 8-11 gas kinetic collisions with water molcules.

2.1.2 Fabrication

Microjets of the required diameter are fabricated using a method developed by the Saykally group [1]. A 9.5±0.5 mm length of 15 μm or 30 μm I.D. fused silica capillary purchased from a liquid chromatography vendor (Western Analytical inc.) is clamped into a piece of 0.020" I.D. by 1/16" O.D. PEEK tubing (Western Analytical Inc. PK1020-OR) that is ~ 8 mm long by a 1/16" Swagelok fitting. This assembly is connected to a 2 μm in-line filter (Western Analytical Inc.) to prevent clogging. Following construction, the whole nozzle assembly is coated in colloidal graphite (Aerodag, Acheson Colloid Co.) to reduce charge buildup on the fused silica and improve signal stability.

Constant flow through the nozzle is maintained by a syringe pump (Teledyne-Isco Model 500D). A typical flow rate of 0.25 mL/min was used for the methanol studies, which were performed using a 15 μm tip (described in Chapter 3). This results in a jet velocity of ~ 24 m/s, determined geometrically from

$$v_{jet} = \frac{\text{flow rate}}{\pi r_0^2} \tag{4}$$

where r_0 is the microjet radius. This velocity is high enough to keep the sample continuously renewed on the time scale of the experiment, minimizing charging through ionization and keeping the surface of the sample clean even under non-UHV conditions.

The flow of liquid through a microjet can be characterized by a Reynolds number (R_e) given by [1]

$$R_e = \frac{2 v_{jet} r_0 \rho}{\eta} \tag{5}$$

Where ρ and η are the density and viscosity of the liquid, respectively. For water, ρ is 1000 kg/m^3 and η is 7.97 x 10-4 kg m^{-1} s^{-1}. An R_e < 2000 indicates that the flow is

laminar. In practice, the laminar region for a water jet is observed to extend 5-10 mm from the tip before entering the turbulent flow regime and breaking up into droplets. The laminar region for a methanol jet is shorter, observed to extend to about 3 mm from the tip. It should be noted that the length of the laminar flow region remains constant under vacuum.

2.1.3 Generation of solvated electrons

The solvated electrons are generated via charge-transfer-to-solvent (CTTS) excitation [10]. This is a pathway for a solute anion, $X^-_{(aq)}$, to eject an electron without being excited into the conduction band. The CTTS state is postulated [11] to be a quasi-bound, locally excited state. To achieve the final state of a separated solvated electron and a neutral solute, the solvent has to rearrange around the new charge density. As these CTTS states do not free the electron and occur well below the vacuum level for $X + e^-$, there is no gas phase analog for this mechanism.

2.1.4 Solvated electron generation and photodetachment laser

The laser and microjet cross at 90° about 1-2 mm downstream from the tip of the jet and ~0.75-1.5 mm from the skimmer that is the entrance to the TOF chamber. The laser beam is focused to about ~100 microns in diameter at the interaction region using a focusing lens. Generally, we first align the laser through the machine and then use the three-axis translation stage to move the liquid jet to meet the laser beam such that we see a peak on the oscilloscope (from photons scattering off the jet) and/or a diffraction pattern in the exit beam.

We used a Nd:YAG photodetachment laser (Spectra-Physics Quanta-Ray Pro 290-30) that operates at a repetition rate of 30 Hz and produces ~35 ns light pulses. The laser pulse is triggered off a Stanford DG-535 digital delay/pulse generator. It has a lasing wavelength of 1064 nm that we convert to 266 nm and 213 nm using, respectively, KDP crystals for the fourth harmonic and a β-barium borate (BBO) for fifth harmonic generation. Our experiments require very low power, using typically 10-35 μJ/pulse at 266 nm and 3-20 μJ/pulse at 213 nm. The optical diagram for our laser setup is shown in Figure 2.2.

2.1.5 Inelastic mean free path (IMFP) of detached electrons

Upon detachment, the electrons show an approximately exponential attenuation in intensity as a function of depth from where they are detached or created [12]. The electron inelastic mean free path (IMFP) is defined as the average length the electron travels, with a given energy, before it experiences its first inelastic collision and loses some of its kinetic energy to the environment. The IMFP is strongly dependent on the nascent kinetic energy of the electron. For most materials, the universal IMFP curve [12] show that the IMFPs, as a function of electron kinetic energy (eKE), are characterized by a minimum of about 5-10 Å in the 50-100 eV eKE range. However, for lower eKEs (what our experiments give), there is a steep increase in IMFPs; there is also a slow increase for higher eKEs. In the range of eKEs we experience (1-2 eV), the IMFPs are not precisely known, but the IMFP is expected to be >10 nm based on recent theoretical and experimental work [12, 13].

2.2 Time-of-flight system

Once the solvated electrons are generated and detached, the next step is to detect them using our TOF system. Electrons with binding energies less than the laser photon energy are detached, detected at the end of the field-free flight tube, and their energies are determined from their time of flights. This section describes the electron detector and instrumentation for data collection.

2.2.1 Field-free flight tube

After passing through a 500 μm skimmer, the detached electrons travel through a 63 cm, field-free drift tube that is orthogonal to the laser and microjet. Photoelectrons are ejected in all directions, but we observe only those contained in the solid angle subtended by the 70 mm-diameter detector, about 0.08%.

Scattered light is reduced by lowering the power of the 266 nm and 213 nm light we use and by installing black anodized light baffles (Figure 2.2) in the laser beam path and trapping the laser beam reflection from the entrance window. We did not install any baffles to capture the reflection from the exit window as that would impede us from viewing the jet to position it inside the machine and to make sure it did not freeze during the experiment.

The photoelectrons of interest have low kinetic energies (~3-4 eV) and are strongly affected by stray electric and magnetic fields, which must be minimized within the flight tube. A cylinder of μ-metal inside the flight tube shields the region from magnetic fields, and the skimmer and microjet nozzle assembly are coated with colloidal graphite (Aerodag, Acheson Colloid Co.) to minimize patch potentials and charge buildup on the fused silica. Residual magnetization inside the flight tube can be decreased significantly by degaussing following the procedure outlined in A. Weaver's thesis [5].

2.2.2 Electron detection, collection and processing

The electron detector (Figure 2.3) is composed of a pair of 70 mm O.D. microchannel plates that is chevron mounted. Typical operating voltages are shown. A grid sits in front of the detector and is grounded with a grounding plug. The grid is used when calibrating the apparatus.

Data acquisition is initiated by each laser light pulse via a fast photodiode that triggers the oscilloscope. Data from each laser pulse are stored (Tektronix TDS 3034B) and read into a PC after every 512 pulses. Accumulated data are displayed on the computer monitor. The entire experiment is computer-controlled using a data acquisition computer program written by Harry Gomez and modified by Alexander T. Shreve. The data collection rate is largely determined by the laser repetition rate of 30 Hz: 10,000 scans require about 5-6 minutes. Our data are usually smoothed by convoluting each data point with a Gaussian peak of fwhm 10 meV.

2.3 Vacuum pumps and liquid nitrogen traps

The liquid jet source region is pumped by a 150 L/s turbomolecular pump (Leybold Turbovac 151) backed by a rotary vane dual stage mechanical vacuum pump (Edwards RV8, 2.8 L/s). Additionally, approximately 10 cm downstream of the nozzle,

the jet enters a trap consisting of a 3.8 cm diameter x 60 cm stainless steel cylinder immersed in 30 cm of liquid nitrogen; a condensation unit made of a 15 cm diameter x 20 cm stainless steel cylinder filled with liquid nitrogen sits in an adjoining chamber.

The TOF chamber is pumped by three turbomolecular pumps with a combined speed of 700 L/s (Seiko Seiki STP 400, Leybold Turbovac 151, Leybold Turbovac 150 CSV) backed by a rotary vane dual stage mechanical vacuum pump (Edwards RV12, 4 L/s). The TOF chamber and the liquid jet source region are isolated from each other by a pneumatic gate valve.

Pressures in both chambers are measured by ionization gauges. Foreline pressures on the rotary backing pumps are measured by thermocouple gauges. Normal operating pressures are 10^{-4} Torr in the liquid jet source region and 4×10^{-6} Torr in the TOF region. A liquid-nitrogen cooled trap in the source foreline was also used.

An interlock system protects the vacuum pumps and electronics in case of equipment failure or high pressure in critical regions. The system is described in detail in A. Weaver's thesis [5] and is slightly modified for the liquid jet apparatus. Because the liquid jet source region has to be vented to atmosphere after each experiment in order to clean the trap and the skimmer, the maximum source and source foreline pressures are set at atmosphere on the ionization and thermocouple gauge controller (Granville-Phillips model 307). We also incorporated the pneumatic gate valve between the liquid jet source and TOF detection regions into the interlock system such that when the interlock relay trips, the gate valve closes.

2.4 Calibration

To calibrate our liquid jet apparatus, we use the negative ion photoelectron spectrometer that has been described in detail previously [2, 4, 5]; the source and first differential regions of the negative ion photoelectron spectrometer are separated from the liquid jet source region by a pneumatic gate valve that remained part of the interlock system described in A. Weaver's thesis [5]. A few modifications have been made to the apparatus hardware of the negative ion photoelectron spectrometer as a result of building the liquid jet apparatus and having an electron detection scheme where the detection axis is collinear to the axis of propagation of the parent ions. The detector at the end of the TOF flight tube is the same as the electron detector in our liquid jet apparatus and detects photoelectrons, ions, and neutral molecules. Neutral molecules are detected when the grid at the front of the detector setup is held at a small positive voltage; the ions are deflected, letting the neutral molecules through to the detector. This allows us to maximize the overlap between the laser and the ions.

A second Einzel lens and a third set of deflectors have been installed in the liquid jet source chamber to further help steer the ions through the 500 μm skimmer that is the entrance to the TOF detection region. The ions pass through the Einzel lens before they are guided by the deflectors. In early experiments, we could not see any electron signal due to the multitude of ions heading to the detector. To prevent background signal from all these ions, a pulsing scheme is typically applied to the second Einzel lens to act as a mass gate. The second Einzel lens is held at a voltage large enough to deflect the ions (typically ~ -3400 V) until ~ 17-20 μs after the target ion is extracted, at which point the voltage on the lens returns to that needed to optimally focus the target ion packet (typically ~ -1000 to -1200 V). The pulse duration is adjusted for each target ion to give optimal ion levels at the ion detector. This way, only the target ion and those ions that arrive later in time than the target ion make it to the detector and we are able to obtain electron signal.

As aforementioned in Section 2.2.3, conversion of electron TOF data to electron kinetic energy requires two parameters: l, the effective flight tube length, and t_0, the timing offset between the time at which the solvated electron is detached and the time at which the photodiode triggers the oscilloscope such that we see signal. An electron with mass m_{e^-} that arrives at the detector at time t has energy

$$E = \tfrac{1}{2} m_{e^-} v_{lab}^2 \tag{6}$$

Where v_{lab} is the velocity of the electron in the lab frame and is given by

$$v_{lab} = \frac{l}{t - t_0} \tag{7}$$

with l the effective flight tube length (to be determined), t the flight time, and t_0 the timing offset (to be determined). Thus

$$E = \tfrac{1}{2} m_{e^-} \frac{l^2}{(t - t_0)^2} \tag{8}$$

In addition, since the electron is born and traveling in the same direction as the propagating ion beam

$$v_{lab} = v_{COM} + v_{e^-,\,COM} \tag{9}$$

with v_{COM} the velocity of the center-of-mass and $v_{e^-,COM}$ the velocity of the electron in the center-of-mass frame.

The velocity of the center-of-mass in this case is equivalent to the velocity of the ion packet.

$$v_{COM} = v_{ion} \tag{10}$$

The ion beam energy is

$$\tfrac{1}{2} m_{ion} v_{ion}^2 = \tfrac{1}{2} \mathrm{V}_{ext} \tag{11}$$

where m_{ion} is the mass of the ion and V_{ext} is the total voltage of the extraction plates. So

$$v_{ion} = \sqrt{\frac{\mathrm{V}_{ext}}{m_{ion}}} \tag{12}$$

The velocity of the electron in the center-of-mass frame is calculated from the binding energy of the electron, which is known.

$$v_{e^-,\,COM} = \sqrt{\frac{2(h\nu - eBE)q_{e^-}}{m_{e^-}}} \tag{13}$$

where $h\nu$ is the photon energy (4.662 eV for a 266 nm photon, 5.822 eV for a 213 nm photon), eBE is the electron binding energy (a known parameter), and q_{e^-} is the charge of the electron.

Putting everything together gives

$$t = l \frac{1}{\sqrt{\frac{2(h\nu - eBE)q_{e^-}}{m_{e^-}}} + \sqrt{\frac{V_{ext}}{m_{ion}}}} + t_0 \tag{14}$$

We can plot t vs. $\frac{1}{\sqrt{\frac{2(h\nu - eBE)q_{e^-}}{m_{e^-}}} + \sqrt{\frac{V_{ext}}{m_{ion}}}}$ to obtain a straight line whose slope and intercept will give us the calibration parameters l and t_0.

We perform a least-squares regression using gas-phase spectra of I^- and Br^- to calibrate at both 266 nm and 213 nm since the neutral electron affinities and spin-orbit splittings are well known [2, 14]. Sample sets of spectra and calibration parameters at 266 nm and 213 nm are shown in Figures 2.3 and 2.4, respectively. The spectra shown are background-subtracted electron TOF spectra, usually averaged for 40,000 - 80,000 laser pulses and taken with a laser polarization that is perpendicular to the plane of the detector. Two kinds of background spectra are collected. Both are collected under the same conditions as the photoelectron spectrum, except in one, no ions are present, and in the other, the laser is blocked after the photodiode and before it enters the machine. Typical background scans are shown in Figure 2.5 and the photoelectron spectrum with and without background subtraction are shown in Figure 2.6.

The instrumental electron energy resolution is affected by many factors. From Eq. (8), any uncertainty in timing, Δt, or in length, Δl, are propagated as energy uncertainty [15]

$$\frac{\Delta E}{E} = \sqrt{\left(\frac{2\Delta t}{t}\right)^2 + \left(\frac{2\Delta l}{l}\right)^2} \tag{15}$$

Since we measure t and not l, Δl (due to the difference in path length between the various trajectories the electron can take inside the machine) will be effectively manifested as a further timing error, Δt'. If we assume $\Delta l = 0$, then for a 3 eV electron with flight path of 63 cm and timing uncertainty (fwhm of peak) at best of ~20 ns, the resolution $\Delta E = \sim 50$ meV. The resolution degrades as $E^{3/2}$ at higher energy.

ION SOURCE AND MASS SPECTROMETER PARTS OF THE NEGATIVE ION PHOTOELECTRON SPECTROMETER

The apparatus used for the gas-phase experiments presented in this thesis is the negative ion photoelectron spectrometer that was constructed prior to the assembly of the liquid jet apparatus and discussed in detail in previous theses. Two electron detector schemes are used: TOF, which is described extensively in the thesis of A. Weaver [5] and velocity-map imaging (VMI), which is described extensively in the thesis of S.M. Sheehan [4].

References

1. Wilson, K.R., et al., *Investigation of volatile liquid surfaces by synchrotron x-ray spectroscopy of liquid microjets.* Review of Scientific Instruments, 2004. **75**(3): p. 725-736.
2. Bradforth, S.E. 1992.
3. Metz, R.B., et al., *PROBING THE TRANSITION-STATE WITH NEGATIVE-ION PHOTODETACHMENT - THE CL + HCL AND BR + HBR REACTIONS.* Journal of Physical Chemistry, 1990. **94**(4): p. 1377-1388.
4. Sheehan, S.M. 2007.
5. Weaver, A. 1991.
6. Faubel, M., S. Schlemmer, and J.P. Toennies, Z. Phys. D, 1988. **10**.
7. Faubel, M. and B. Steiner, *STRONG BIPOLAR ELECTROKINETIC CHARGING OF THIN LIQUID JETS EMERGING FROM 10 MU-M PTIR NOZZLES.* Berichte Der Bunsen-Gesellschaft-Physical Chemistry Chemical Physics, 1992. **96**(9): p. 1167-1172.
8. Hirschfelder, J.O., C.F. Curtiss, and R.B. Bird, *Molecular theory of gases and liquids*. 1954, New York: Wiley.
9. Wagner, W. and A. Pruss, *The IAPWS formulation 1995 for the thermodynamic properties of ordinary water substance for general and scientific use.* Journal of Physical and Chemical Reference Data, 2002. **31**(2): p. 387-535.
10. Chen, X.Y. and S.E. Bradforth, *The ultrafast dynamics of photodetachment.* Annual Review of Physical Chemistry, 2008. **59**: p. 203-231.
11. Kloepfer, J.A., et al., *The ejection distribution of solvated electrons generated by the one-photon photodetachment of aqueous I- and two-photon ionization of the solvent.* Journal of Chemical Physics, 2000. **113**(15): p. 6288-6307.
12. Ottosson, N., et al., *Photoelectron spectroscopy of liquid water and aqueous solution: Electron effective attenuation lengths and emission-angle anisotropy.* Journal of Electron Spectroscopy and Related Phenomena. **177**(2-3): p. 60-70.
13. Emfietzoglou, D. and H. Nikjoo, *The effect of model approximations on single-collision distributions of low-energy electrons in liquid water.* Radiation Research, 2005. **163**(1): p. 98-111.
14. Hotop, H. and W.C. Lineberger, *BINDING-ENERGIES IN ATOMIC NEGATIVE-IONS .2.* Journal of Physical and Chemical Reference Data, 1985. **14**(3): p. 731-750.
15. Wilden, D.G., P.J. Hicks, and J. Comer, *AUTOIONIZATION OF N2 STUDIED USING AN ELECTRON TIME-OF-FLIGHT COINCIDENCE SPECTROMETER.* Journal of Physics B-Atomic Molecular and Optical Physics, 1976. **9**(11): p. 1959-1974.

Figure 2.1 Schematic of liquid microjet apparatus

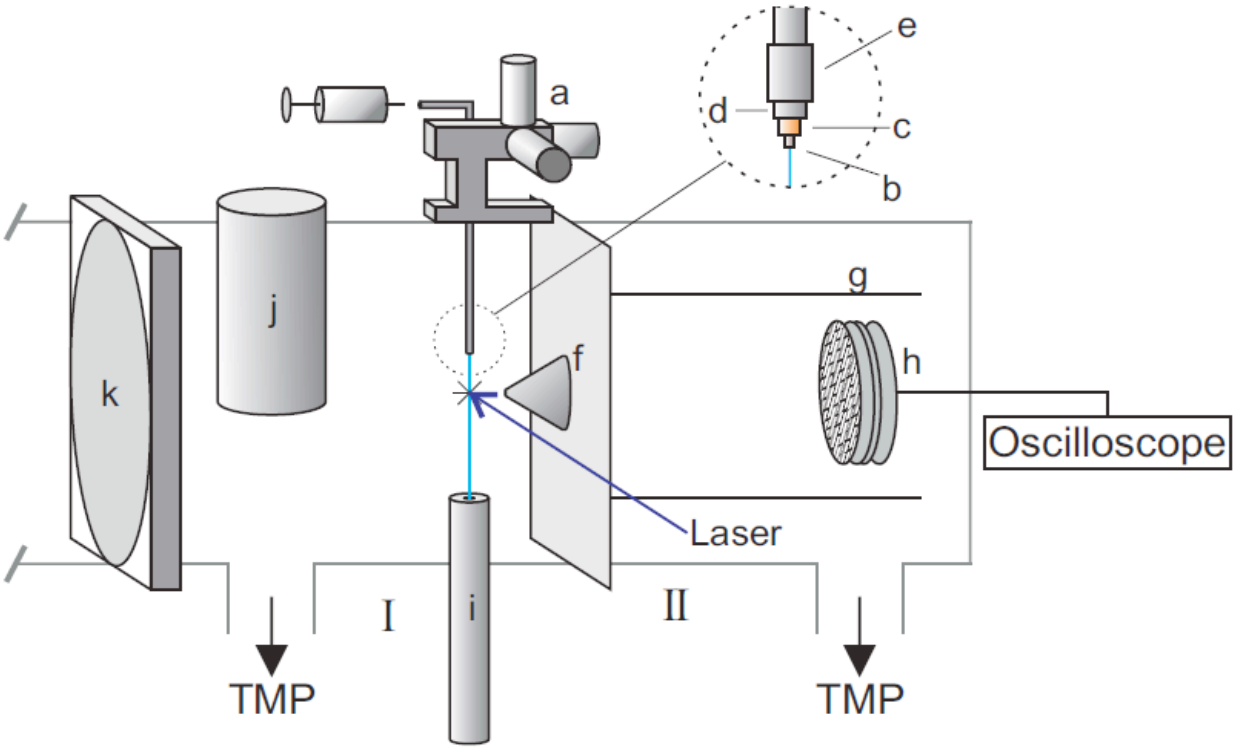

Figure 2.2 Laser optics

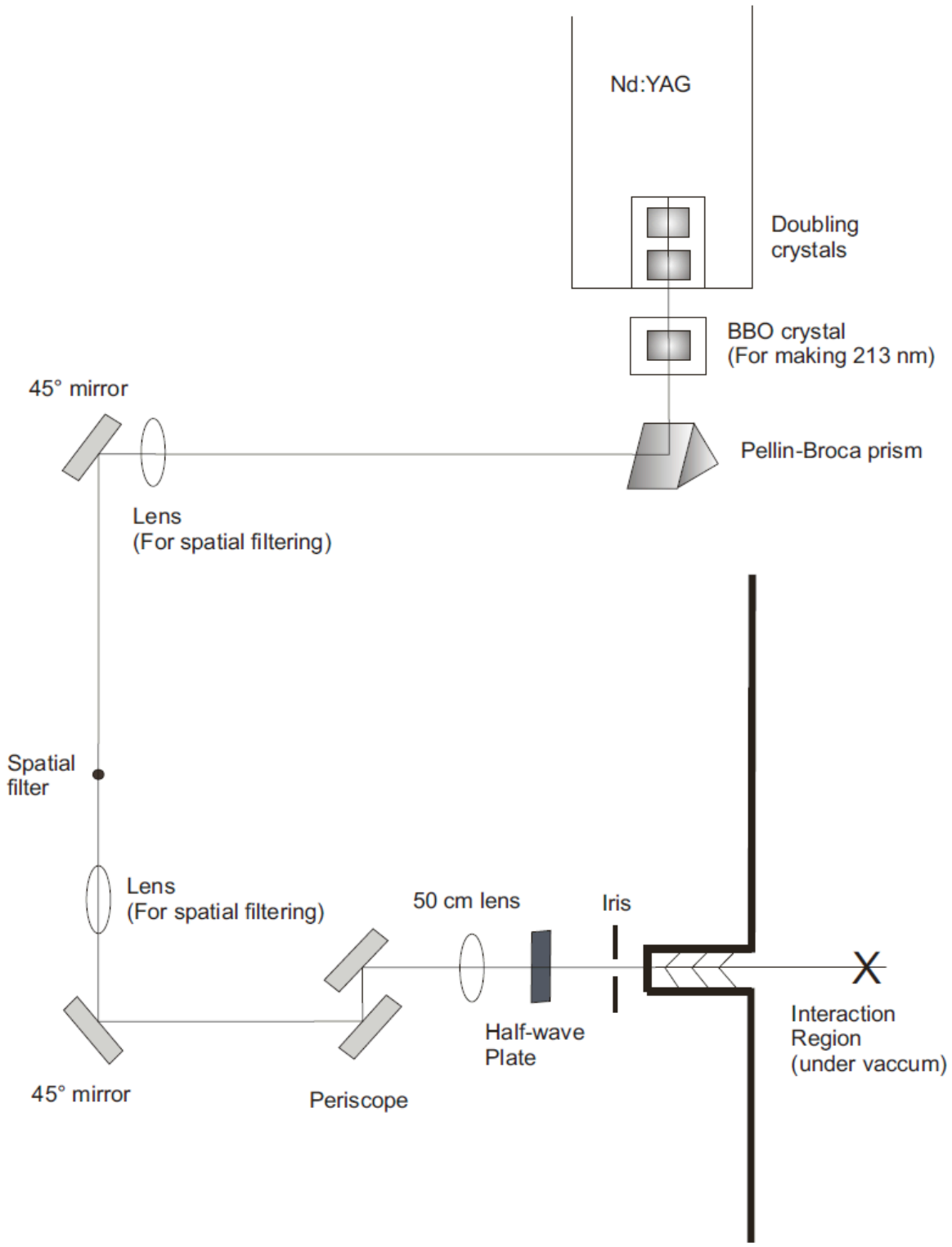

Figure 2.3 Electron detector circuit diagram (NOT TO SCALE)

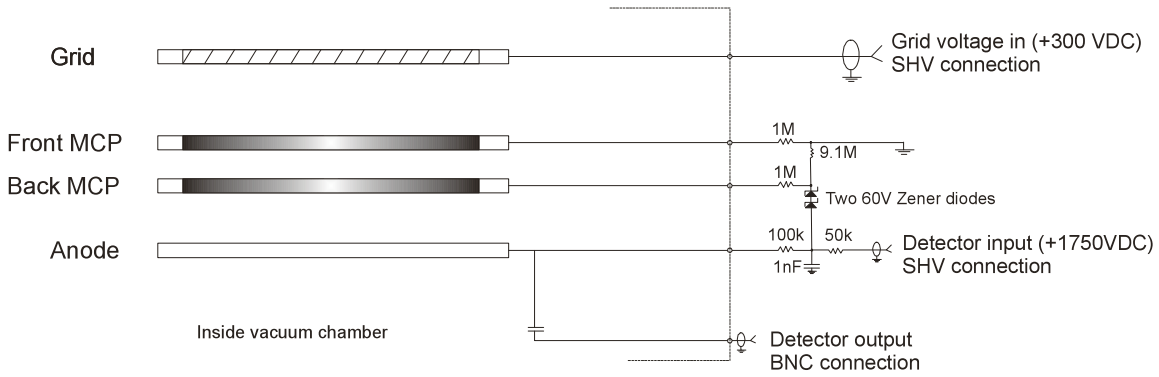

Figure 2.4 Sample calibration spectra and parameters at 266 nm

Photoelectron spectra of I^- at 266 nm

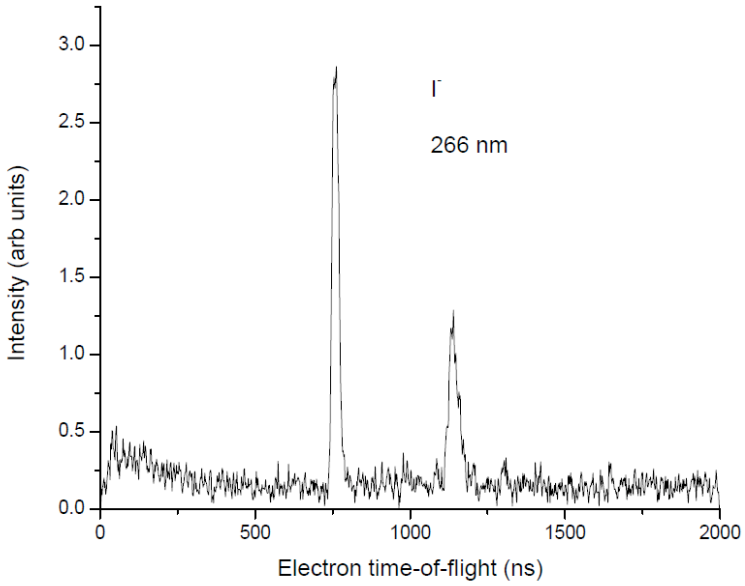

Calibration parameters

Ion and transition	*t* (ns)
$I\ ^2P_{3/2} \leftarrow I^-$	759.37
$I\ ^2P_{1/2} \leftarrow I^-$	1140.3

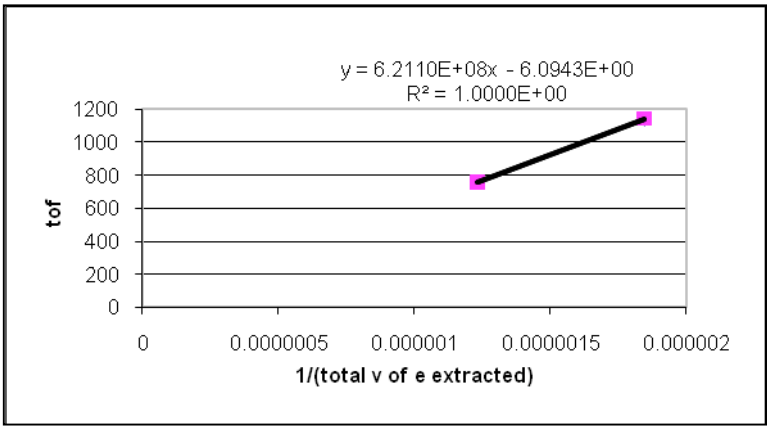

length = 62.11 cm
t_0 = -6.09 ns

Figure 2.5 Sample calibration spectra and parameters at 213 nm

Photoelectron spectra of I^- and Br^- at 213 nm

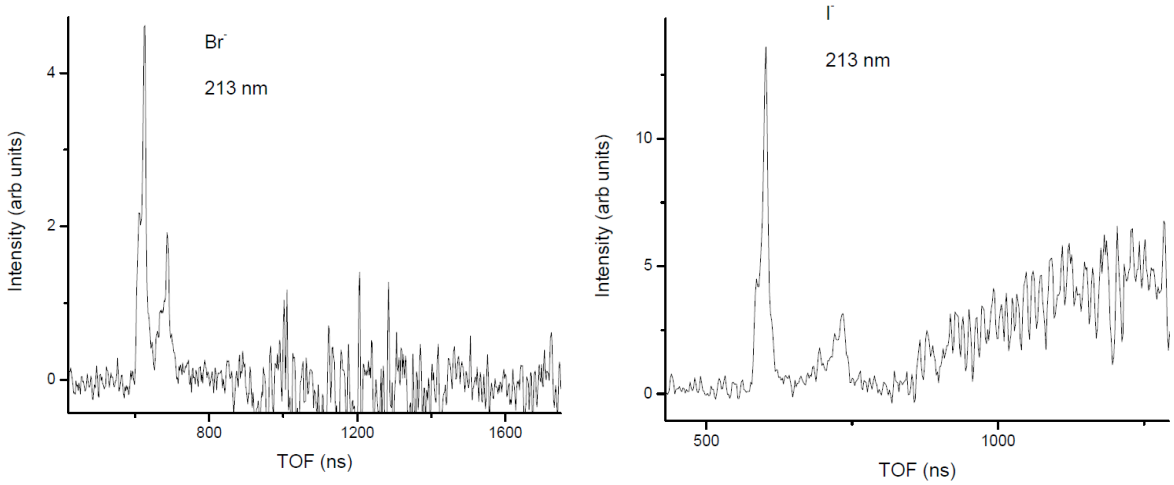

Calibration parameters

Ion and transition	*t* (ns)
$I\ ^2P_{3/2} \leftarrow I^-$	600.78
$I\ ^2P_{1/2} \leftarrow I^-$	728.23
$Br\ ^2P_{3/2} \leftarrow Br^-$	622.42
$Br\ ^2P_{1/2} \leftarrow Br^-$	682.17

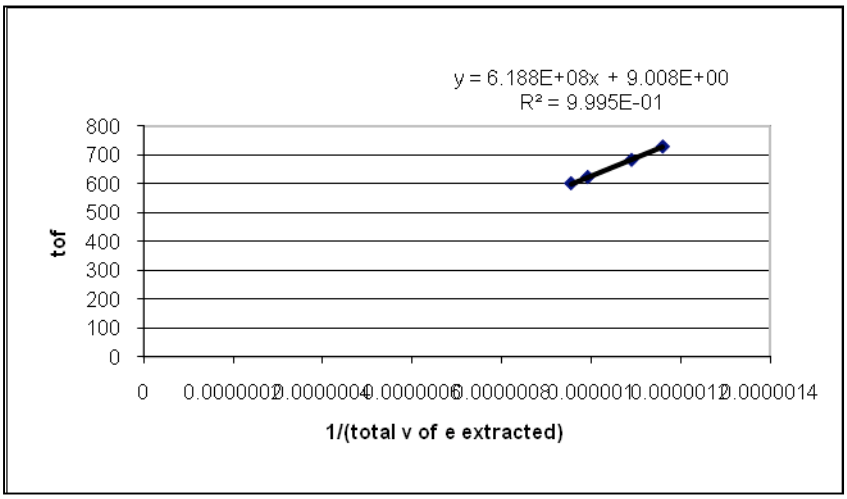

length = 61.88 cm
t_0 = +9.008 ns

Figure 2.6

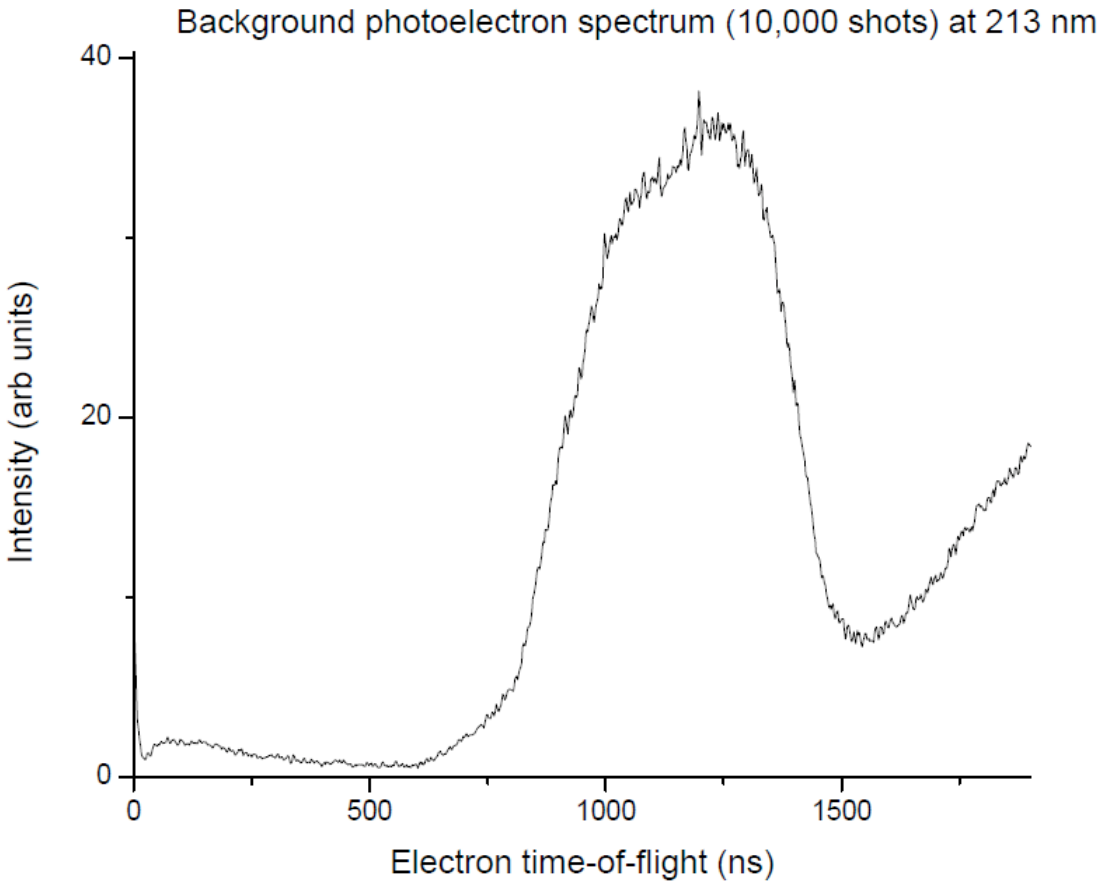
Background photoelectron spectrum (10,000 shots) at 213 nm
Intensity (arb units)
40
20
0
0
500
1000
1500
Electron time-of-flight (ns)

Figure 2.7 Background subtraction of calibration photoelectron spectra at 213 nm

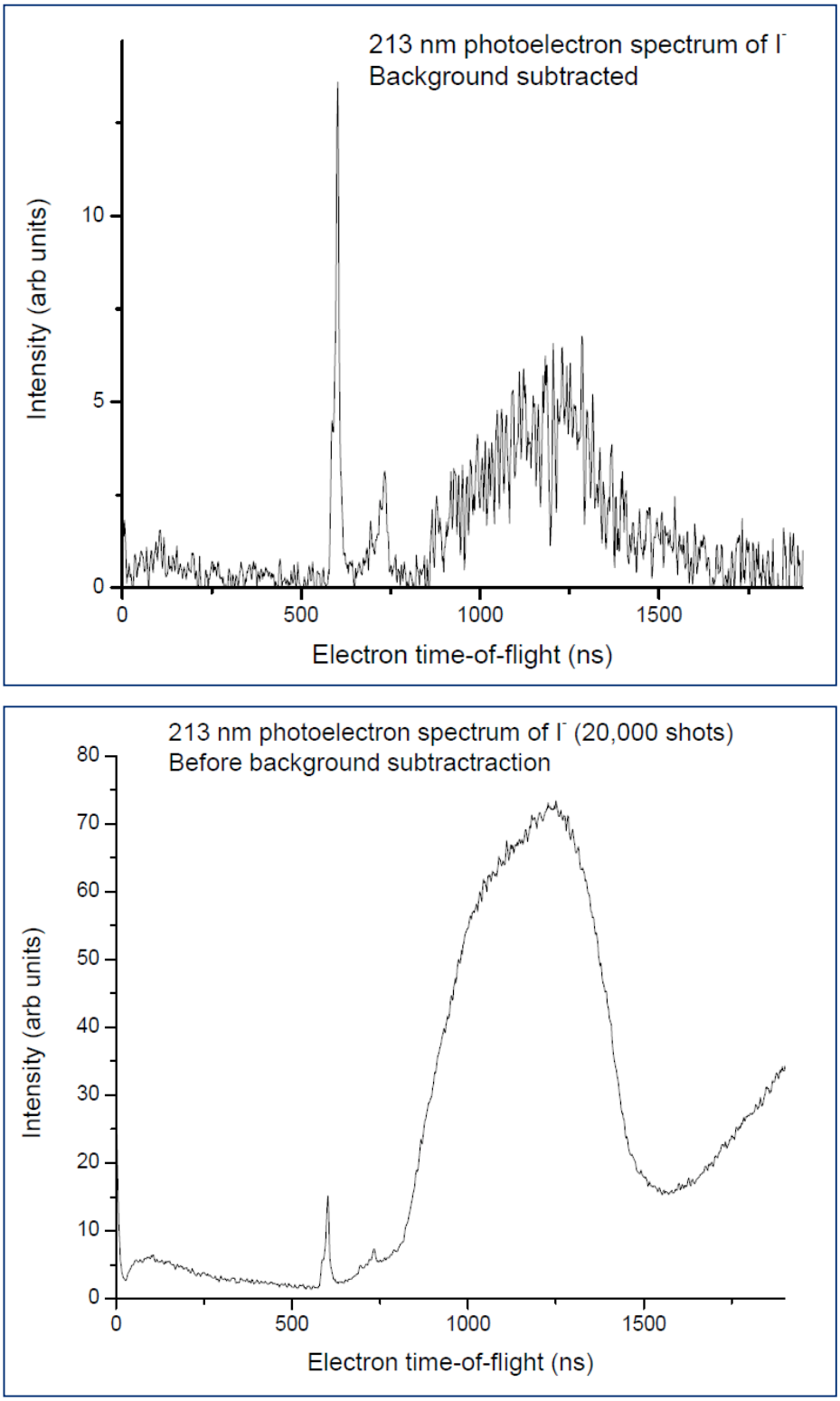

Chapter 3

Anion photoelectron spectroscopy of solvated electrons in methanol

The following chapter reports our preliminary measurement of the vertical binding energy of the solvated electron in methanol. Two photons from a single nanosecond laser pulse at 213 nm were used to first create the solvated electrons by charge transfer to solvent excitation using I^- anions in methanol and to then detach them from the microjet. Initial experiments using a solution of 100 mM potassium iodide indicate a vertical binding energy of 3.6 eV.

3.1 Introduction

The solvated electron plays an important role in fundamental chemical and biological processes. First discovered in solutions of alkali metals and alkaline earth metals in ammonia to give the solutions their bright blue to copper colors, the solvated electron represents the simplest quantum mechanical solute [1, 2]. Numerous experimental and theoretical studies have been performed on electrons solvated in water [1, 3-8] (also known as the hydrated electron), and to a lesser extent, on electrons solvated in ammonia [9], acetonitrile [10], and simple alcohols [11]. These studies have provided valuable insights into the nature of the solvated electron, shedding light on its spectroscopy, reactivity and relaxation dynamics subsequent to electronic excitation.

Complementing the condensed phase work are parallel efforts focused on gas phase cluster anions in which an excess electron is bound to a known number of solvent molecules [4]. However, extrapolation of properties such as the vertical binding energy (VBE) and relaxation timescales from clusters to the bulk size regime is controversial, due to the presence of multiple cluster anion isomers. For example, three types of isomers have been found for negatively charged water clusters [3, 5, 12-16] and two for negatively charged methanol clusters [17]. The isomers vary in the magnitudes of their VBE's and their yields depend on molecular beam conditions. The elucidation of electron binding motifs in these isomers has consequently attracted much interest.

Until recently, there has been no direct measurement of the VBE of the solvated electron; the VBE has been estimated by extrapolating to the infinite size limit the VBE's of the variously sized negatively charged clusters [4]. With the development of liquid microjets by Faubel [18], the first measurement of the VBE of the hydrated electron[6-8] was achieved. Tang, et al. and Siefermann et al. used time-resolved photoelectron spectroscopy (TR-PES) while we used a time-independent approach. Our study gave a slightly higher value for the VBE of the hydrated electron; we measured 3.6±0.1 eV while Tang, et al. and Siefermann, et al. measured 3.3 eV.

Methanol, the simplest alcohol and considered as "methylated water", is thus logically, the next solvent to study in order to gain a clearer understanding of not only the solvated electron in alcohols, but also the hydrated electron. The present chapter discusses our work on the VBE of the solvated electron in methanol. Electron spin resonance spectra have suggested that the first solvation shell of a solvated electron consists of four methanol molecules, compared to the six water molecules that make up the first solvation shell of the hydrated electron [19]. Additionally, several experiments have been performed on elucidating the relaxation dynamics of the solvated electron bulk methanol [20, 21]. Moreover, using photoelectron imaging, Kammrath, et al. [17] observed two isomers for negatively charged methanol clusters $(MeOH)_n^-$ in the size range of $n \sim 70 - 460$. For the isomer termed methanol I, they measured VBE's ranging from 2 – 2.5 eV and proposed that the excess electron is internally solvated. For the other isomer, methanol II, they measured much lower VBE's, between 0.2 and 0.5 eV, and proposed that the excess electron resides in a dipole-bound surface state. These

considerations have motivated us to investigate the spectroscopy of the solvated electron in methanol.

3.2 Experimental setup

The set up used in this experiment has been described in detail previously [6]. In the present study, we generate solvated electrons in methanol by charge transfer to solvent (CTTS) excitation of I^-. The CTTS absorption spectra of I^- in alcohols are similar to that in water, with a peak at around 220 nm [8]. A microjet flowing 100 mM KI solution in methanol (methanol: Fischer Scientific Optima grade, 0.2 micron filtered ; potassium iodide: Fisher, USP/FCC) is controlled via a three-axis translation stage. The microjet consists of a nozzle of the type developed by Saykally [ref]. A short length of 15 μm I.D. fused silica capillary is clamped into ~8 mm polyether ether ketone (PEEK) tubing by a Swagelok fitting. Constant flow is maintained through the nozzle by a syringe pump (Teledyne-Isco model 500D) with a 2 μm in-line filter to prevent clogging. We noticed that the piston and wiper seals in the syringe pump have to be regularly checked to ensure constant flow through the 15 μm fused silica tip. Following construction, the nozzle assembly is coated with colloidal graphite (Aerodag, Acheson Colloid Co.) to reduce charge buildup on the fused silica and improve signal stability. The liquid flow rate was 0.25 mL/min, resulting in a jet velocity of 24 m/s. The methanol microjet typically exhibits laminar flow for ~3 – 5 mm from the tip before entering the turbulent flow regime and breaking into droplets.

A pulsed laser beam (30 Hz) intersects the methanol jet 1 – 2 mm downstream from the tip and is focused on the liquid jet by a 40 – 50 cm lens. We use the 5^{th} (213 nm, 5.826 eV) harmonic of an Nd:YAG laser (Spectra Physics Quanta-Ray Pro 290-30). The typical laser power we use is 3 – 20 μJ/pulse and the laser polarization is parallel to the axis of the electron detector. The energy resolution of our experiment is determined to be ~50 meV from the line width of the photoelectron spectrum of gaseous I^-.

With this experimental configuration, two photons from a single ~40 ns laser pulse are used. The first generates the solvated electrons by CTTS excitation of the aqueous I^- anions; the second ejects the electron into vacuum. These photoelectrons are sampled by a 500 μm diameter skimmer, located 0.75 – 1.5 mm from the microjet, and detected at the end of a ~63 cm long field-free flight tube by a pair of chevron-mounted microchannel plates (70 mm O.D., 9.7 msr acceptance angle). The time-of-flights (TOF) of the electrons are recorded and averaged on an oscilloscope, passed to a computer, and summed typically for 10,000 shots. A strong photoelectron signal is seen on the oscilloscope when the laser beam overlaps with the methanol jet.

The pressure in the source chamber reaches 1.5 – 2 x 10^{-4} Torr and is maintained by a 150 L/s turbomolecular pump (Leybold Turbovac 151), a condensation unit filled

with liquid nitrogen, and a collection trap for the jet approximately 10 cm downstream of the nozzle that is also immersed in liquid nitrogen. The detection chamber reaches 4 x 10^{-6} Torr and is pumped by three turbomolecular pumps with a combined speed of 700 L/s.

The liquid microjet apparatus is calibrated using the known photoelectron spectra of gaseous I^- and Br^- at 213 nm. The I^- and Br^- anions are introduced into the spectrometer using an ion source and mass spectrometer that has been described in detail previously [22]. Briefly, anions are formed by supersonically expanding through a piezoelectric valve [23] a gas mixture consisting of 20 psig Ar carrier gas and either bromomethane (Br^-) or trifluoromethyl iodide (I^-) and passing through a pulsed discharge (-700 – 1000 V) stabilized by a 1 keV electron beam. Anions are mass-selected using a linear reflectron mass spectrometer with a mass resolution of $\Delta m/m = 2000$. Various ion optics steer the anions to the interaction region right in front of the 500 μm skimmer, where they intersect the photodetachment laser. A small fraction of the ejected photoelectrons are sampled by the skimmer and enter the TOF electron detection system of our liquid microjet apparatus, where they are detected at the end of a field-free flight tube by a pair of microchannel plates.

3.3 Preliminary results

Photoelectron spectra were recorded at 213 nm (5.826 eV). Figure 3.1 shows the raw time-of-flight spectrum for 100 mM KI in methanol. The signal below 500 ns is from light scattered off the jet and into the flight tube. The broad feature peaking around 670 ns in the spectrum from the methanol-salt solution is from ejected photoelectrons.

The time-of-flight spectra we collect are converted into energy spectra, plotted as relative intensity versus electron kinetic energy (eKE), using the appropriate Jacobian transformation. A typical background subtracted photoelectron spectrum of 100 mM KI in methanol is shown in Figure 3.2, plotted in terms of electron binding energy (eBE), which is given by eBE = $h\nu$ – eKE, where $h\nu$ is the photon energy (in this case, 5.826 eV). From the peak eBE of the photoelectron distribution, we find the quantity of interest, the VBE of the solvated electron in methanol, to be 3.6 eV. The peak width is 1.3 eV full width at half maximum (fwhm). This value is comparable to the VBE of the hydrated electron (3.6 ± 0.1 eV) determined in our previous study [6], and significantly higher than the value of 3.1 ± 0.1 eV reported by Shen et al. [24]. Since our preliminary finding is much larger than previous work, current experiments are underway to determine the effects of the streaming potential of our microjet. As demonstrated in previous works [24, 25], the liquid beam from the microjet is electrically charged by the dynamic separation of electrical double layers formed around the inner wall of the jet nozzle. Significant streaming currents can be generated as a result of this, creating radial

surface potentials up to tens of volts. The electric potential can accelerate or decelerate photoelectrons ejected from the microjet.

3.4 Conclusions

We have tentatively measured the vertical binding energy of the solvated electron in methanol at 213 nm. Two photons from a single ns laser pulse were used to excite the iodide anion (from potassium iodide) in methanol to its charge-transfer-to-solvent state to generate and then detach the solvated electron from the liquid microjet into vacuum. The low photon energy used here ensures that we are probing electrons borne in the bulk methanol. Our preliminary findings indicate that the VBE of the solvated electron in methanol is 3.6 eV.

Acknowledgments

This work is supported by the U.S. Department of Energy (Contract # DE-AC02-05CH11231) and the American Chemical Society Petroleum Research Fund (Grant # 47852-AC6).

References

1. Rossky, P.J. and J. Schnitker, *THE HYDRATED ELECTRON - QUANTUM SIMULATION OF STRUCTURE, SPECTROSCOPY, AND DYNAMICS.* Journal of Physical Chemistry, 1988. **92**(15): p. 4277-4285.
2. Madarasz, A., P.J. Rossky, and L. Turi, *Response of Observables for Cold Anionic Water Clusters to Cluster Thermal History.* Journal of Physical Chemistry A. **114**(6): p. 2331-2337.
3. Bragg, A.E., et al., *Hydrated electron dynamics: From clusters to bulk.* Science, 2004. **306**(5696): p. 669-671.
4. Coe, J.V., et al., *PHOTOELECTRON-SPECTROSCOPY OF HYDRATED ELECTRON CLUSTER ANIONS, (H2O)N-=2-69.* Journal of Chemical Physics, 1990. **92**(6): p. 3980-3982.
5. Paik, D.H., et al., *Electrons in finite-sized water cavities: Hydration dynamics observed in real time.* Science, 2004. **306**(5696): p. 672-675.
6. Shreve, A.T., T.A. Yen, and D.M. Neumark, *Photoelectron spectroscopy of hydrated electrons.* Chemical Physics Letters. **493**(4-6): p. 216-219.
7. Siefermann, K.R., et al., *Binding energies, lifetimes and implications of bulk and interface solvated electrons in water.* Nature Chemistry. **2**(4): p. 274-279.
8. Tang, Y., et al., *Direct measurement of vertical binding energy of a hydrated electron.* Physical Chemistry Chemical Physics. **12**(15): p. 3653-3655.
9. Symons, M.C.R., *SOLUTIONS OF METALS - SOLVATED ELECTRONS.* Chemical Society Reviews, 1976. **5**(4): p. 337-358.
10. Shkrob, I.A. and M.C. Sauer, *Electron localization in liquid acetonitrile.* Journal of Physical Chemistry A, 2002. **106**(39): p. 9120-9131.
11. Baxendal, J. and P. Wardman, *ELECTRONS IN LIQUID ALCOHOLS AT LOW-TEMPERATURES.* Journal of the Chemical Society-Faraday Transactions I, 1973. **69**(3): p. 584-594.
12. Coe, J.V., S.M. Williams, and K.H. Bowen, *Photoelectron spectra of hydrated electron clusters vs. cluster size: connecting to bulk.* International Reviews in Physical Chemistry, 2008. **27**(1): p. 27-51.
13. Hammer, N.I., et al., *How do small water clusters bind an excess electron?* Science, 2004. **306**(5696): p. 675-679.
14. Neumark, D.M., *Spectroscopy and dynamics of excess electrons in clusters.* Molecular Physics, 2008. **106**(16-18): p. 2183-2197.
15. Turi, L., W.S. Sheu, and P.J. Rossky, *Characterization of excess electrons in water-cluster anions by quantum simulations.* Science, 2005. **309**(5736): p. 914-917.
16. Verlet, J.R.R., et al., *Observation of large water-cluster anions with surface-bound excess electrons.* Science, 2005. **307**(5706): p. 93-96.
17. Kammrath, A., et al., *Photoelectron imaging of large anionic methanol clusters: (MeOH)(n)(-) (n similar to 70-460).* Journal of Chemical Physics, 2006. **125**(17): p. 4.
18. Winter, B. and M. Faubel, *Photoemission from liquid aqueous solutions.* Chemical Reviews, 2006. **106**(4): p. 1176-1211.

19. Kevan, L., *FORBIDDEN MATRIX PROTON SPIN-FLIP SATELLITES IN 70-GHZ ESR-SPECTRA OF SOLVATED ELECTRONS - GEOMETRICAL MODEL FOR THE SOLVATED ELECTRON IN METHANOL GLASS.* Chemical Physics Letters, 1979. **66**(3): p. 578-580.
20. Silva, C., et al., *Detailed investigations of the pump-probe spectroscopy of the equilibrated solvated electron in alcohols.* Journal of Physical Chemistry A, 1998. **102**(28): p. 5701-5707.
21. Thaller, A., R. Laenen, and A. Laubereau, *The precursors of the solvated electron in methanol studied by femtosecond pump-repump-probe spectroscopy.* Journal of Chemical Physics, 2006. **124**(2): p. 9.
22. Metz, R.B., et al., *PROBING THE TRANSITION-STATE WITH NEGATIVE-ION PHOTODETACHMENT - THE CL + HCL AND BR + HBR REACTIONS.* Journal of Physical Chemistry, 1990. **94**(4): p. 1377-1388.
23. Proch, D. and T. Trickl, *A HIGH-INTENSITY MULTI-PURPOSE PIEZOELECTRIC PULSED MOLECULAR-BEAM SOURCE.* Review of Scientific Instruments, 1989. **60**(4): p. 713-716.
24. Shen, H., et al., *Direct Measurement of Vertical Electron Binding Energies of Solvated Electrons in Methanol and Ethanol.* Chemistry Letters, 2010. **39**: p. 668-770.
25. Faubel, M., B. Steiner, and J.P. Toennies, *Photoelectron spectroscopy of liquid water, some alcohols, and pure nonane in free micro jets.* Journal of Chemical Physics, 1997. **106**(22): p. 9013-9031.

Figure 3.1 Time-of-flight spectrum for 100 mM KI in methanol solution

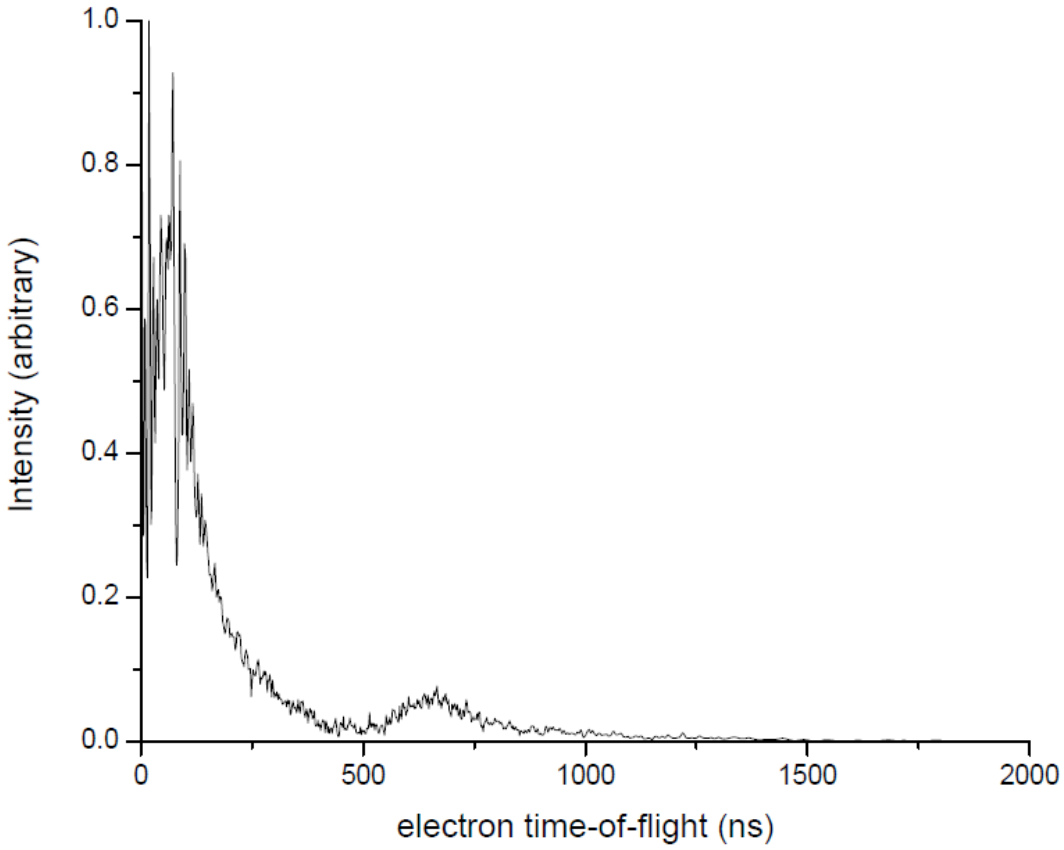

Figure 3.2 Photoelectron spectrum of 100 mM KI in methanol solution

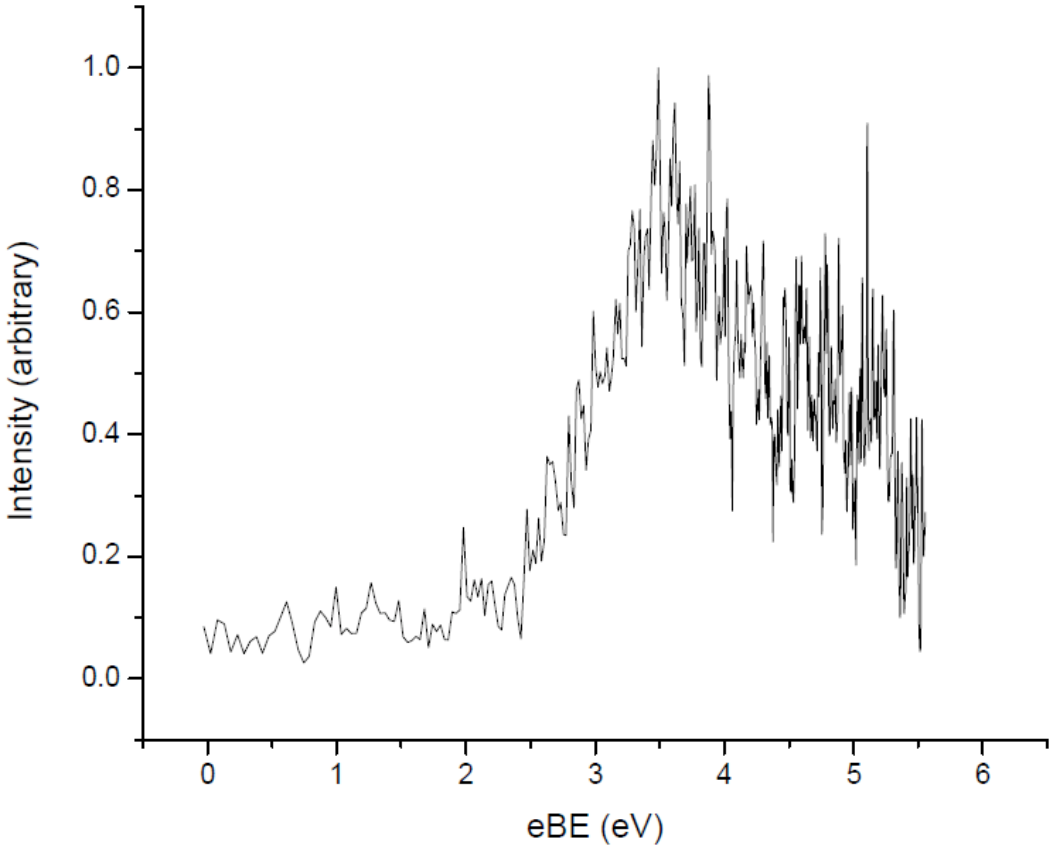

Chapter 4

Anion photoelectron spectroscopy of deprotonated cytosine and thymine at 5.826 eV

UV radiation from sunlight is one of the most ubiquitous and lethal forms of environmental carcinogens. Luckily, perhaps as a result of selective pressure by molecular evolution, DNA is remarkably stable to photochemical decay. The solar UV photons are absorbed primarily by the building blocks of DNA, the nucleobases, which undergo ultrafast nonradiative relaxation processes back to the ground state by internal conversion. It has been suggested that the nucleobases' excited singlet states of $\pi\sigma^*$ character, which are dissociative along the NH stretch coordinate, play a key role in the relaxation pathways. Studying the dynamics of the excited states of deprotonated nucleobases is therefore of great importance in understanding the photostability of DNA.

Excited state dynamics of the deprotonated nucleobases cytosine and thymine has been investigated using anion photoelectron spectroscopy at 5.826 eV. In the experiments, a laser is used to detach an electron from a mass selected deprotonated nucleobase anion and the electron kinetic energy (eKE) is measured using velocity-map imaging (VMI). Through VMI, information is obtained on the nature of the excited states involved in the non-radiative processes of DNA.

4.1 Introduction

Deoxyribonucleic acid (DNA), the information carrier in most biological systems, is made up of four nucleobases: adenine (A), guanine (G), thymine (T) and cytosine (C). These nucleobases absorb strongly in the 200 – 300 nm range, yet are remarkably stable to photochemical decay [1]. It seems that their photostability results from undergoing ultrafast nonradiative decay processes back to their electronic ground states upon absorption of UV photons. These nonradiative relaxation pathways allow the photon energy to quickly dissipate before more profound and/or mutagenic chemical rearrangements can take place, such as single strand breaks (SSB) and/or double strand breaks (DSB) that occur through cleavage of either the sugar-phosphate bond or the sugar-nucleobase bond [2]. Therefore, understanding the conversion mechanisms behind DNA's photostability is of great importance.

Recent experimental and computational work on the isolated nucleobases has led to significant progress in understanding their mechanisms of radiationless decay. Resonance-enhanced multiphoton ionization (REMPI) as well as laser-induced fluorescence (LIF) spectra of the pyrimidine bases uracil (a RNA nucleobase) and thymine have been found to be broad and structureless, suggesting extensive mixing among the excited states and short excited-state lifetimes [3]. REMPI and LIF spectra of cytosine and the purine bases adenine and guanine have a short progression of sharp vibronic lines, followed by an unstructured absorption band at higher energies [4-6]. Time-resolved experiments of both isolated DNA bases and of those in solution have confirmed the subpicosecond excited-state lifetimes. These results indicate that the excited-state relaxation processes must be intramolecular in nature and likely related to conical intersections because of the very short timescales involved.

There are unfortunately relatively few calculations of the excited states of the DNA bases performed with *ab initio* methods. The presence of several heteroatoms with lone pairs results in the existence of a large number of low-lying $^1n\pi^*$ and $^1\pi\sigma^*$ states on top of the $^1\pi\pi^*$ states that complicate the electronic spectrum and increase the tedium and time of the calculations. Futhermore, the DNA bases each have several tautomers whose electronic ground states lie close in energy. These tautomers arise from the movement of the hydrogen atoms.

Vertical excitation energies have been obtained by various methods for the DNA bases [7-18]. Additional computational studies have revealed the existence of low-lying conical intersections and indicated that the conical intersections related to certain out-of-plane deformations of the six-membered heteroatomatic rings may play a dominant role in the ultrafast internal conversion dynamics of the lowest excited states of adenine [19-24], uracil [25-27], and cytosine [28, 29].

In spite of the experimental and theoretical investigations, the photophysics of DNA bases is poorly understood. Several relaxation pathways have been discussed; the three main mechanisms are presented. Soblewski and coworkers [30] theorized that the

excited electronic states of $^1\pi\sigma^*$ character play a pivotal role in the fast internal conversion of the electronically excited singlet states of 9H-adenine. These $^1\pi\sigma^*$ states are dark in absorption and their potential energy surfaces are dissociative along the OH/NH stretch coordinates. Their existence has been confirmed experimentally [31]. More importantly, they exhibit conical intersections with the electronic ground state and the $^1\pi\pi^*$ states that lie relatively high in energy. These intersections provide a pathway for ultrafast internal conversion to the ground state. The ground state dissociates along the NH coordinate towards an excited $^2\sigma$ radical, while the lowest $^1\pi\sigma^*$ state dissociates towards the $^2\pi$ ground state of the deprotonated radical. In contrast, other researchers [10, 11, 21, 31, 32] theorized that an $n\pi^*$ state couples the $\pi\pi^*$ state to the S_0 ground state of adenine and that this coupling is responsible for the fast radiationless quenching of photochemical reactions in DNA. Experimental support for the existence of the np* state lying close to the pp* state and the involvement of the np* state in the relaxation process has been reported in several studies [4, 10, 33-36]. Finally, Perun and coworkers [1] and Merchan and coworkers [29] identified a third photochemical reaction path that involves a conical intersection between the $^1\pi\pi^*$ state and the S_0 ground state that is characterized by strongly out-of-plane deformations of the six-membered aromatic ring. Perun located, for thymine, three S_1-S_0 conical intersections. The lowest-energy intersection arises from a crossing of the lowest $^1\pi\pi^*$ state with the electronic ground state and is speculated to provide the most direct and fastest relaxation pathway. The other two conical intersections involve the crossing of the lowest $^1n\pi^*$ excited state with the electronic ground state and are significantly higher in energy.

In this chapter, we attempt to better elucidate the radiationless decay mechanism behind the photostability of DNA by investigating the deprotonated nucleobases (thymine and cytosine in particular) at high photon energy (213 nm, 5.826 eV). We focus on more comprehensively examining the conical intersection of the $^1\pi\sigma^*$ state surface with the electronic ground state that Soblewski and coworkers [30] found by measuring the energy splitting between the $^2\sigma$ ground state and the first $^2\pi$ excited state of the deprotonated radical species.

4.2 Experimental setup

Details of our anion photoelectron spectrometer have been discussed previously [37]. Briefly, anions are formed by first supersonically expanding 15 psi Ar carrier gas into the source region. The Ar gas passes through a heated reservoir containing the nucleobase (thymine or cytosine), which is heated to ~50-60°C, a range that is below the decomposition temperature of the nucleobase. The resulting Ar/nucleobase gas mixture then passes through a pulsed discharge and crosses with a 1 keV electron beam. The anions generated are collimated by a skimmer, extracted by pulsed electric fields, and are mass-selected using a linear reflectron time-of-flight (TOF) mass spectrometer with a

mass resolution ($m/\Delta m$) of 2000. Various ion optics steer the anions to the interaction region of either our velocity-map imaging (VMI) detection system [38, 39] or our field-free time-of-flight (TOF) detection system, where they are photodetached by a laser.

We modified our VMI setup to reduce the background electrons from photons striking the repeller plate (A in Figure 4.1A and B in Figure 4.1B). As shown in Figure 4.1B, a center grid is added to the repeller, which allows ~70% of the scattered photons to pass through and maintains a uniform electric field. An additional plate (A in Figure 4.1B) is installed below the repeller and held at a positive bias during the experiment. This plate serves as an electron "collector" to remove background electrons ejected from the grid. Typical operating voltages are 3.0 kV for A (the "collector"), -1.7 kV for B (the repeller), -1.1 kV for C (the extractor), and 0 V for D (the ground plate).

The 5th (213 nm, 5.826 eV) harmonic of an Nd:YAG laser is used. The laser is focused ~1.5 cm before the interaction region between the repeller and extractor plates of our modified VMI setup using a 50 cm fused silica lens. The electrons are detached perpendicularly to the laser and ion beams and are accelerated towards a 2-D position sensitive detector, comprising of two microchannel plates coupled to a phosphor screen. An externally triggered charge coupled device (CCD) records the output of the phosphor screen. Photoelectron images are typically acquired for 50,000 shots.

The original 3-D distribution is reconstructed from the 2-D image by the basis set expansion (BASEX) Abel transform method [40]. The central 2-D slice of the reconstructed 3-D image is angularly integrated to obtain a photoelectron (PE) spectrum. The photoelectron spectra of deprotonated thymine and cytosine are calibrated using the known 213 nm PE spectrum of I^- and Br^-. The best energy resolution for these experiments is about 2 pixels, which corresponds to a $\Delta E/E$ of ~2.0%. Anion photoelectron spectroscopy using VMI is becoming an increasingly attractive technique because it offers high collection efficiency (100%), simultaneous measurement of photoelectron kinetic energy and angular distributions, and sensitivity to low energy photoelectrons.

Figure 4.2A shows the raw (left) and reconstructed (right) images of I^- photodetached at 213 nm using the traditional VMI setup. The bright spot in the center of the raw image is from background electrons ejected by photons hitting the repeller plate. The photoelectron spectrum obtained from the image in Figure 4.2A is shown in Figure 4.2C. The background electrons give a large peak at low eKE.

Figure 4.2B shows the raw (left) and reconstructed (right) images of I^- photodetached at 213 nm using the modified VMI setup. The bright center spot is now gone and signal from background electrons is seen primarily as a spot to the left of the image. This is presumably from stray photons striking the solid outer ring of the repeller. The photoelectron spectrum obtained from the image in Figure 4.2B is shown in Figure 4.2D. The background peak is significantly reduced in intensity and appears at high eKE, which is desirable because the low eKE range is typically of great interest at high photon energies. Electrons scattered from the grid are not velocity mapped onto the detector; since the detachment laser is focused before the interaction region, most of the scattered

electrons appear after the interaction region and map to the left side of the image in Figure 4.2B.

In the field-free TOF detection scheme, photoelectrons are detected by a pair of microchannel plates mounted in a chevron configuration at the end of a field-free flight tube ~1m long that is oriented perpendicular to both the ion and laser beam axes. The energy resolution is 8-10 meV at 0.65 eV electron kinetic energy (eKE) and degrades as $eKE^{3/2}$ for higher eKE.

The angular distribution of the photoelectrons is given by [41]

$$I(\theta) = \frac{1}{4\pi}[1 + \frac{\beta}{2}(3\cos^2\theta - 1)] \quad (1)$$

where I(θ) is the photoelectron angular distribution, θ is the angle between the laser electric field and the TOF axis of the electron, and β is the anisotropy parameter, which varies from -1 to 2. A β of 0 represents an isotropic photoelectron distribution while a β of -1 and 2 give $\sin^2\theta$ and $\cos^2\theta$ distributions, respectively. β can be obtained directly by fitting the data to Eqn (1).

4.3 Results on T_{-H}^- and C_{-H}^-

Figures 4.3 and 4.4 show the velocity-mapped photoelectron image (left) and reconstructed image (right) of deprotonated thymine (T_{-H}^-) and deprotonated cytosine (C_{-H}^-) taken at a detachment energy of 5.826 eV. Figures 4.5 and 4.6 show the anion PE spectra of T_{-H}^- and C_{-H}^-, respectively, derived from the photoelectron images in Figures 4.3 and 4.4. The PE spectra are plotted in electron binding energy (eBE), defined as eBE = $h\nu$ – eKE, where $h\nu$ is the photon energy and eKE is the electron kinetic energy derived from the image.

The T_{-H}^- PE spectrum shows two broad bands, X_0 and X_1, centered around 3.53 eV and 4.82 eV, respectively. The peak X_0 corresponds to a feature we saw with better resolution in the PE spectrum of T_{-H}^- at 355 nm (3.496 eV) [37], namely a transition arising from detachment from the anion ground state to the ground state of the neutral radical isomer resulting from deprotonation from the N1 nitrogen site. Band X_1 is a new feature that is revealed from detaching at 213 nm (5.826 eV), which may correspond to transitions to the excited states of T_{-H}^-.

The C_{-H}^- PE spectrum is similar to that of T_{-H}^-. It shows two bands, X_0 and X_1, with peak maxima at around 3.28 eV and 4.36 eV, respectively. The peak X_0 corresponds to a feature we saw in the PE spectrum of C_{-H}^- at 355 nm (3.496 eV) [37], namely a transition arising from detachment from the anion ground state to the ground state of the neutral radical isomer resulting from deprotonation from the N1 nitrogen site. Band X_1 is a new feature that is revealed from detaching at 213 nm (5.826 eV), which may correspond to transitions to the excited states of C_{-H}^-.

To confirm the existence of this new feature at higher eBE for both deprotonated nucleobases, we obtained photoelectron spectra of T_{-H}^- and C_{-H}^- at 5.826 eV using the field-free TOF electron detection technique. Unfortunately, the TOF spectra have not been very conclusive, due to low signal.

4.4 Preliminary analysis and discussion

The chemical structures of thymine and cytosine are shown in Figure 4.7A. The isomers of deprotonated thymine and deprotonated cytosine from deprotonation at the nitrogen sites are shown in Figure 4.7B and Figure 4.7C, respectively. In contrast to the radicals corresponding to deprotonation at a carbon site, the radicals that result from deprotonation at the nitrogen sites have electron affinities in the energetic range of the photoelectron spectra. From calculations and simulations performed for the T_{-H}^- and C_{-H}^- photoelectron spectra collected at 355 nm (3.496 eV) [37], the isomers we are most likely photodetaching are the N1 T_{-H}^- and C_{-H}^- isomers.

Analysis of the photoelectron spectra collected at 213 nm (5.826 eV) thus requires electronic structure calculations of the excited states of the N1 T_{-H}^- isomer and of the N1 C_{-H}^- isomer and Franck-Condon (FC) simulations, the results of which are pending.

4.5 Conclusions

We present the photoelectron spectra of deprotonated thymine and deprotonated cytosine at 5.826 eV obtained using velocity-map imaging. We have modified our velocity-map imaging optics setup, which has led to a significant reduction of background photoelectrons and has opened the possibility for future studies at high photon energies. The photoelectron spectra of both deprotonated nucleobases exhibit two bands. In both spectra, the band at lower electron binding energy corresponds to a transition seen in the photoelectron spectra obtained using velocity-map imaging at 3.496

eV. This transition arises from detachment from the anion ground state to the neutral radical ground state of the N1 isomer of deprotonated thymine or cytosine. The band at higher electron binding energy in both spectra is a new feature revealed at 5.826 eV that may be due to transitions to the excited states of the neutral radical of deprotonated thymine or deprotonated cytosine. To confirm this new feature, photoelectron spectra of deprotonated thymine and deprotonated cytosine at 5.826 eV were obtained using the field-free time-of-flight technique, but have proved inconclusive due to low signal.

Acknowledgments

This work is supported by the National Science Foundation under grant number DMR-0139064.

References

1. Perun, S., A.L. Sobolewski, and W. Domcke, *Conical intersections in thymine.* Journal of Physical Chemistry A, 2006. **110**(49): p. 13238-13244.
2. Simons, J., *How do low-energy (0.1-2 eV) electrons cause DNA-strand breaks?* Accounts of Chemical Research, 2006. **39**(10): p. 772-779.
3. Brady, B.B., L.A. Peteanu, and D.H. Levy, *THE ELECTRONIC-SPECTRA OF THE PYRIMIDINE-BASES URACIL AND THYMINE IN A SUPERSONIC MOLECULAR-BEAM.* Chemical Physics Letters, 1988. **147**(6): p. 538-543.
4. Kim, N.J., et al., *Resonant two-photon ionization and laser induced fluorescence spectroscopy of jet-cooled adenine.* Journal of Chemical Physics, 2000. **113**(22): p. 10051-10055.
5. Nir, E., et al., *On the photochemistry of purine nucleobases.* Journal of Physical Chemistry A, 2001. **105**(21): p. 5106-5110.
6. Piuzzi, F., et al., *Ultraviolet spectroscopy and tautomerism of the DNA base guanine and its hydrate formed in a supersonic jet.* Chemical Physics, 2001. **270**(1): p. 205-214.
7. Lorentzon, J., M.P. Fulscher, and B.O. Roos, *THEORETICAL-STUDY OF THE ELECTRONIC-SPECTRA OF URACIL AND THYMINE.* Journal of the American Chemical Society, 1995. **117**(36): p. 9265-9273.
8. Shukla, M.K. and J. Leszczynski, *TDDFT investigation on nucleic acid bases: Comparison with experiments and standard approach.* Journal of Computational Chemistry, 2004. **25**(5): p. 768-778.
9. Shukla, M.K. and P.C. Mishra, *A gas phase ab initio excited state geometry optimization study of thymine, cytosine and uracil.* Chemical Physics, 1999. **240**(3): p. 319-329.
10. Broo, A., *A theoretical investigation of the physical reason for the very different luminescence properties of the two isomers adenine and 2-aminopurine.* Journal of Physical Chemistry A, 1998. **102**(3): p. 526-531.
11. Broo, A. and A. Holmen, *Calculations and characterization of the electronic spectra of DNA bases based on ab initio MP2 geometries of different tautomeric forms.* Journal of Physical Chemistry A, 1997. **101**(19): p. 3589-3600.
12. Fulscher, M.P., L. SerranoAndres, and B.O. Roos, *A theoretical study of the electronic spectra of adenine and guanine.* Journal of the American Chemical Society, 1997. **119**(26): p. 6168-6176.
13. Jensen, H.J.A., et al., *DIRECT ITERATIVE RPA CALCULATIONS - APPLICATIONS TO ETHYLENE, BENZENE AND CYTOSINE.* Chemical Physics, 1988. **119**(2-3): p. 297-306.
14. Matos, J.M.O. and B.O. Roos, *ABINITIO QUANTUM CHEMICAL STUDY OF THE PI-ELECTRON SPECTRUM OF THE CYTOSINE MOLECULE.* Journal of the American Chemical Society, 1988. **110**(23): p. 7664-7671.
15. Mennucci, B., A. Toniolo, and J. Tomasi, *Theoretical study of guanine from gas phase to aqueous solution: Role of tautomerism and its implications in absorption and emission spectra.* Journal of Physical Chemistry A, 2001. **105**(29): p. 7126-7134.

16. Mennucci, B., A. Toniolo, and J. Tomasi, *Theoretical study of the photophysics of adenine in solution: Tautomerism, deactivation mechanisms, and comparison with the 2-aminopurine fluorescent isomer.* Journal of Physical Chemistry A, 2001. **105**(19): p. 4749-4757.
17. Petke, J.D., G.M. Maggiora, and R.E. Christoffersen, *ABINITIO CONFIGURATION-INTERACTION AND RANDOM PHASE APPROXIMATION CALCULATIONS OF THE EXCITED SINGLET AND TRIPLET-STATES OF ADENINE AND GUANINE.* Journal of the American Chemical Society, 1990. **112**(14): p. 5452-5460.
18. Rachofsky, E.L., et al., *CASSCF investigation of electronic excited states of 2-aminopurine.* Journal of Physical Chemistry A, 2001. **105**(1): p. 190-197.
19. Blancafort, L., *Excited-state potential energy surface for the photophysics of adenine.* Journal of the American Chemical Society, 2006. **128**(1): p. 210-219.
20. Chen, H. and S.H. Li, *Theoretical study toward understanding ultrafast internal conversion of excited 9H-adenine.* Journal of Physical Chemistry A, 2005. **109**(38): p. 8443-8446.
21. Marian, C.M., *A new pathway for the rapid decay of electronically excited adenine.* Journal of Chemical Physics, 2005. **122**(10): p. 13.
22. Nielsen, S.B. and T.I. Solling, *Are conical intersections responsible for the ultrafast processes of adenine, protonated adenine, and the corresponding nucleosides?* Chemphyschem, 2005. **6**(7): p. 1276-1281.
23. Perun, S., A.L. Sobolewski, and W. Domcke, *Ab initio studies on the radiationless decay mechanisms of the lowest excited singlet states of 9H-adenine.* Journal of the American Chemical Society, 2005. **127**(17): p. 6257-6265.
24. Perun, S., A.L. Sobolewski, and W. Domcke, *Photostability of 9H-adenine: mechanisms of the radiationless deactivation of the lowest excited singlet states.* Chemical Physics, 2005. **313**(1-3): p. 107-112.
25. Gustavsson, T., et al., *Singlet excited-state behavior of uracil and thymine in aqueous solution: A combined experimental and computational study of 11 uracil derivatives.* Journal of the American Chemical Society, 2006. **128**(2): p. 607-619.
26. Matsika, S., *Radiationless decay of excited states of uracil through conical intersections.* Journal of Physical Chemistry A, 2004. **108**(37): p. 7584-7590.
27. Zgierski, M.Z., et al., *On the origin of the ultrafast internal conversion of electronically excited pyrimidine bases.* Journal of Physical Chemistry A, 2005. **109**(42): p. 9384-9387.
28. Ismail, N., et al., *Ultrafast decay of electronically excited singlet cytosine via pi,pi* to n(o)pi* state switch.* Journal of the American Chemical Society, 2002. **124**(24): p. 6818-6819.
29. Merchan, M. and L. Serrano-Andres, *Ultrafast internal conversion of excited cytosine via the lowest pi pi* electronic singlet state.* Journal of the American Chemical Society, 2003. **125**(27): p. 8108-8109.
30. Sobolewski, A.L., et al., *Excited-state hydrogen detachment and hydrogen transfer driven by repulsive (1)pi sigma* states: A new paradigm for nonradiative decay in aromatic biomolecules.* Physical Chemistry Chemical Physics, 2002. **4**(7): p. 1093-1100.

31. Hunig, I., et al., *Photostability of isolated and paired nucleobases: N-H dissociation of adenine and hydrogen transfer in its base pairs examined by laser spectroscopy.* Chemphyschem, 2004. **5**(9): p. 1427-1431.
32. Canuel, C., et al., *Time-resolved photoelectron and photoion fragmentation spectroscopy study of 9-methyladenine and its hydrates: a contribution to the understanding of the ultrafast radiationless decay of excited DNA bases.* Physical Chemistry Chemical Physics, 2006. **8**(34): p. 3978-3987.
33. Kang, H., B. Jung, and S.K. Kim, *Mechanism for ultrafast internal conversion of adenine.* Journal of Chemical Physics, 2003. **118**(15): p. 6717-6719.
34. Kang, H., et al., *Intrinsic lifetimes of the excited state of DNA and RNA bases.* Journal of the American Chemical Society, 2002. **124**(44): p. 12958-12959.
35. Ullrich, S., et al., *Direct observation of electronic relaxation dynamics in adenine via time-resolved photoelectron spectroscopy.* Journal of the American Chemical Society, 2004. **126**(8): p. 2262-2263.
36. Plutzer, C. and K. Kleinermanns, *Tautomers and electronic states of jet-cooled adenine investigated by double resonance spectroscopy.* Physical Chemistry Chemical Physics, 2002. **4**(20): p. 4877-4882.
37. Parsons, B.F., et al., *Anion photoelectron imaging of deprotonated thymine and cytosine.* Physical Chemistry Chemical Physics, 2007. **9**(25): p. 3291-3297.
38. Chandler, D.W. and P.L. Houston, *TWO-DIMENSIONAL IMAGING OF STATE-SELECTED PHOTODISSOCIATION PRODUCTS DETECTED BY MULTIPHOTON IONIZATION.* Journal of Chemical Physics, 1987. **87**(2): p. 1445-1447.
39. Eppink, A. and D.H. Parker, *Velocity map imaging of ions and electrons using electrostatic lenses: Application in photoelectron and photofragment ion imaging of molecular oxygen.* Review of Scientific Instruments, 1997. **68**(9): p. 3477-3484.
40. Dribinski, V., et al., *Reconstruction of abel-transformable images: The Gaussian basis-set expansion abel transform method.* Review of Scientific Instruments, 2002. **73**(7): p. 2634-2642.
41. Cooper, J. and R.N. Zare, *ANGULAR DISTRIBUTION OF PHOTOELECTRONS.* Journal of Chemical Physics, 1968. **48**(2): p. 942

Figure 4.1 Traditional versus modified velocity-map imaging optics setup

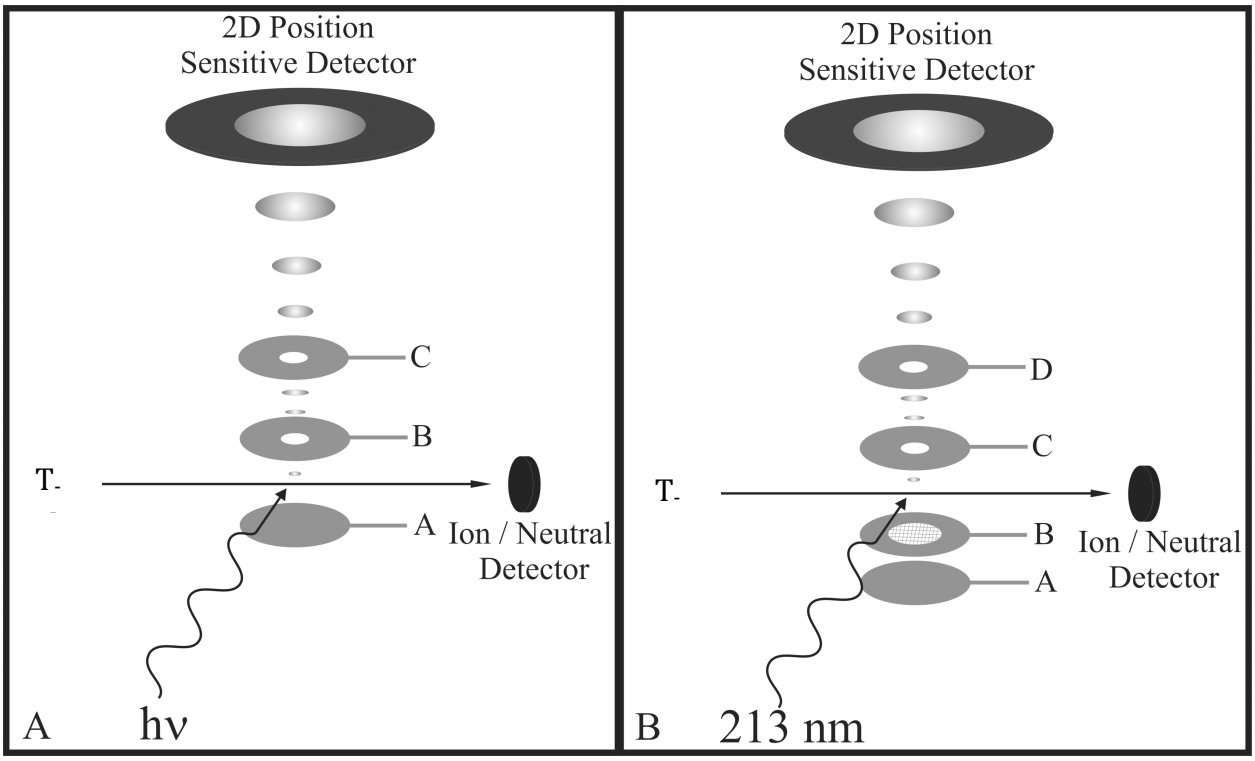

Figure 4.2 Photoelectron images and spectra collected using the traditional versus modified velocity-map imaging optics setups

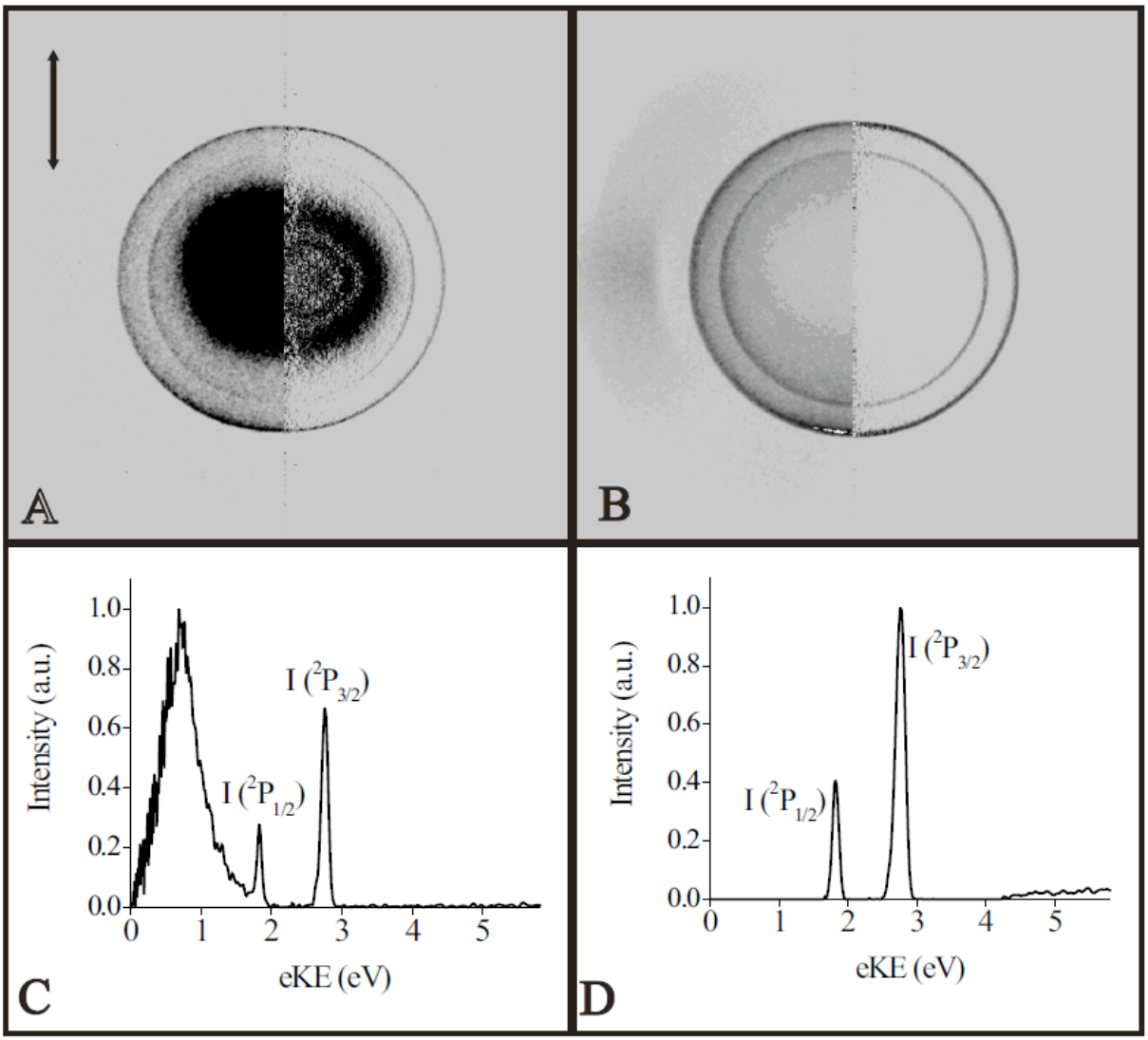

Figure 4.3 Photoelectron image of T_{-H}^{-} at 5.826 eV

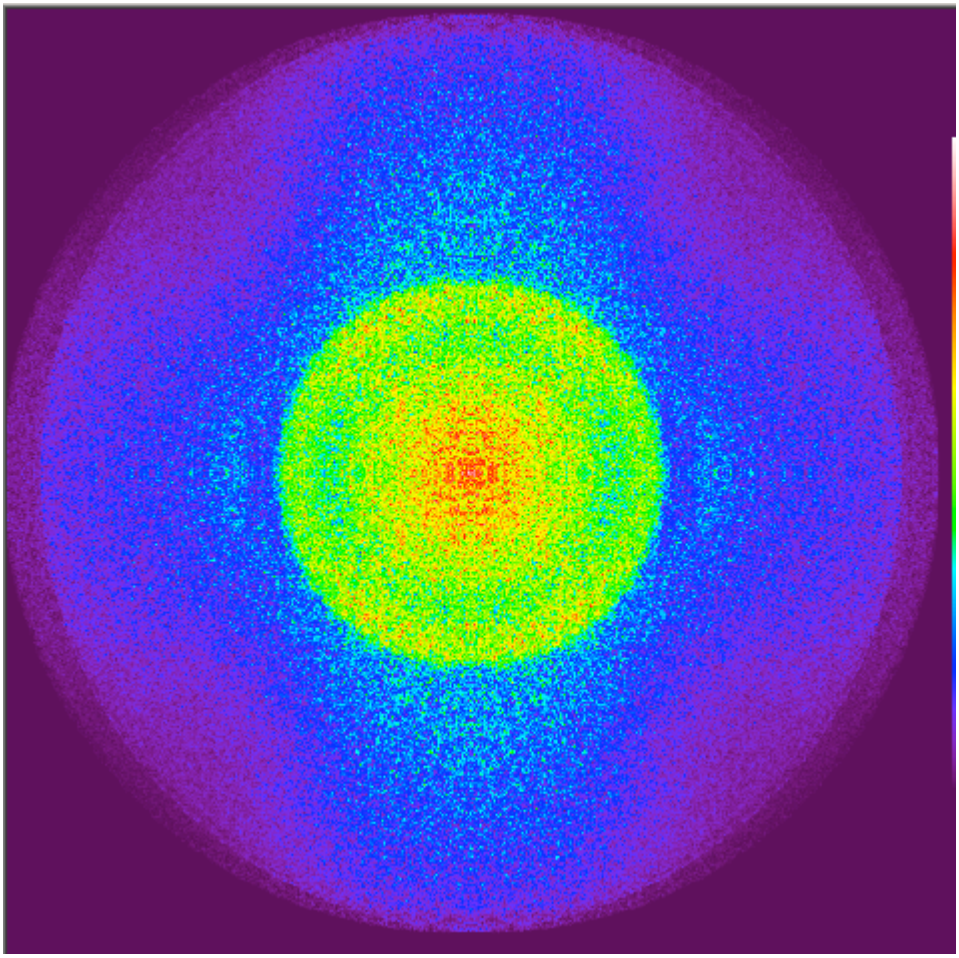

Figure 4.4 Photoelectron image of C_{-H}^- at 5.826 eV

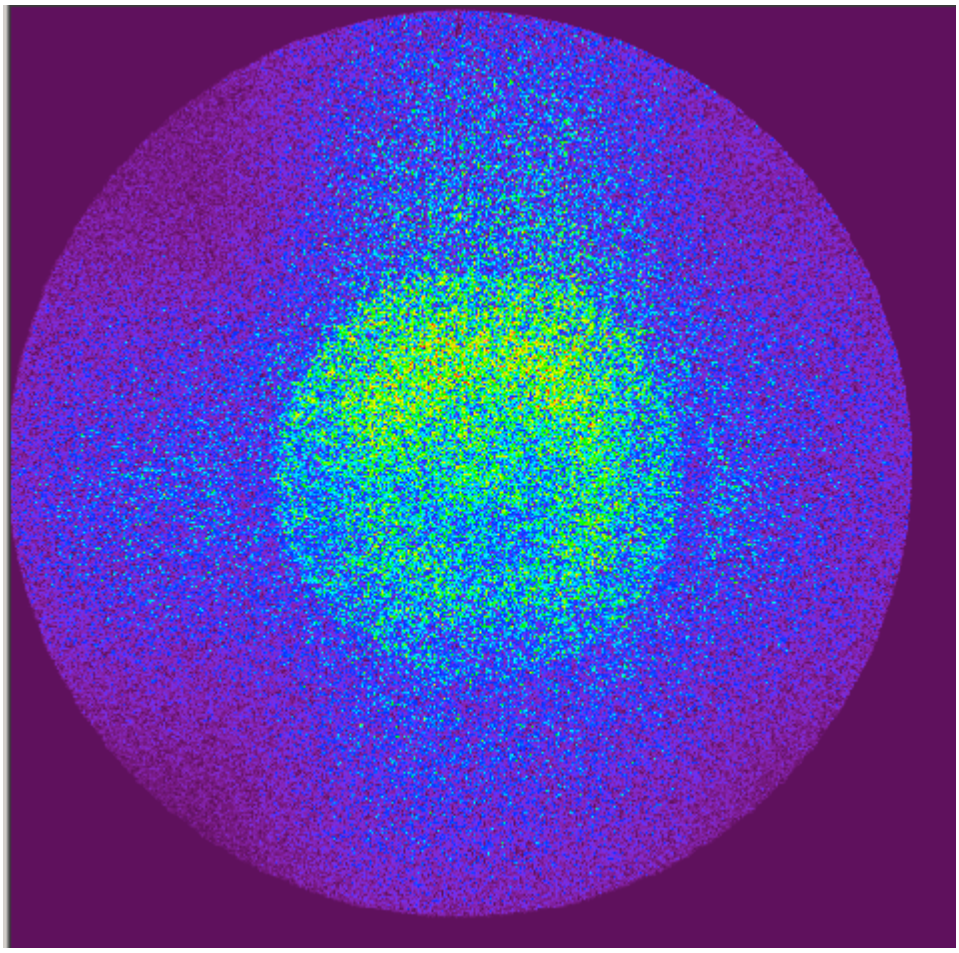

Figure 4.5 Photoelectron spectrum of T_{-H}^{-} at 5.826 eV

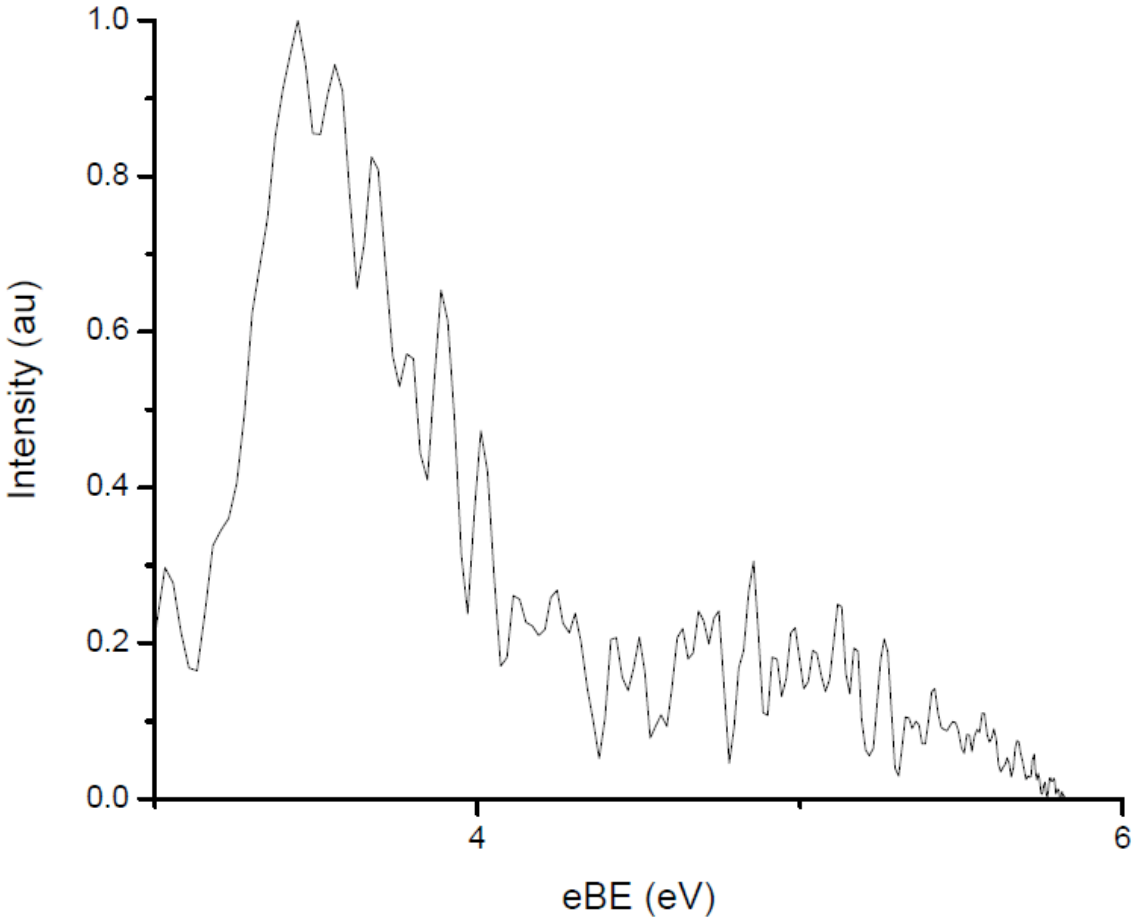

Figure 4.6 Photoelectron spectrum of C_{-H}^- at 5.826 eV

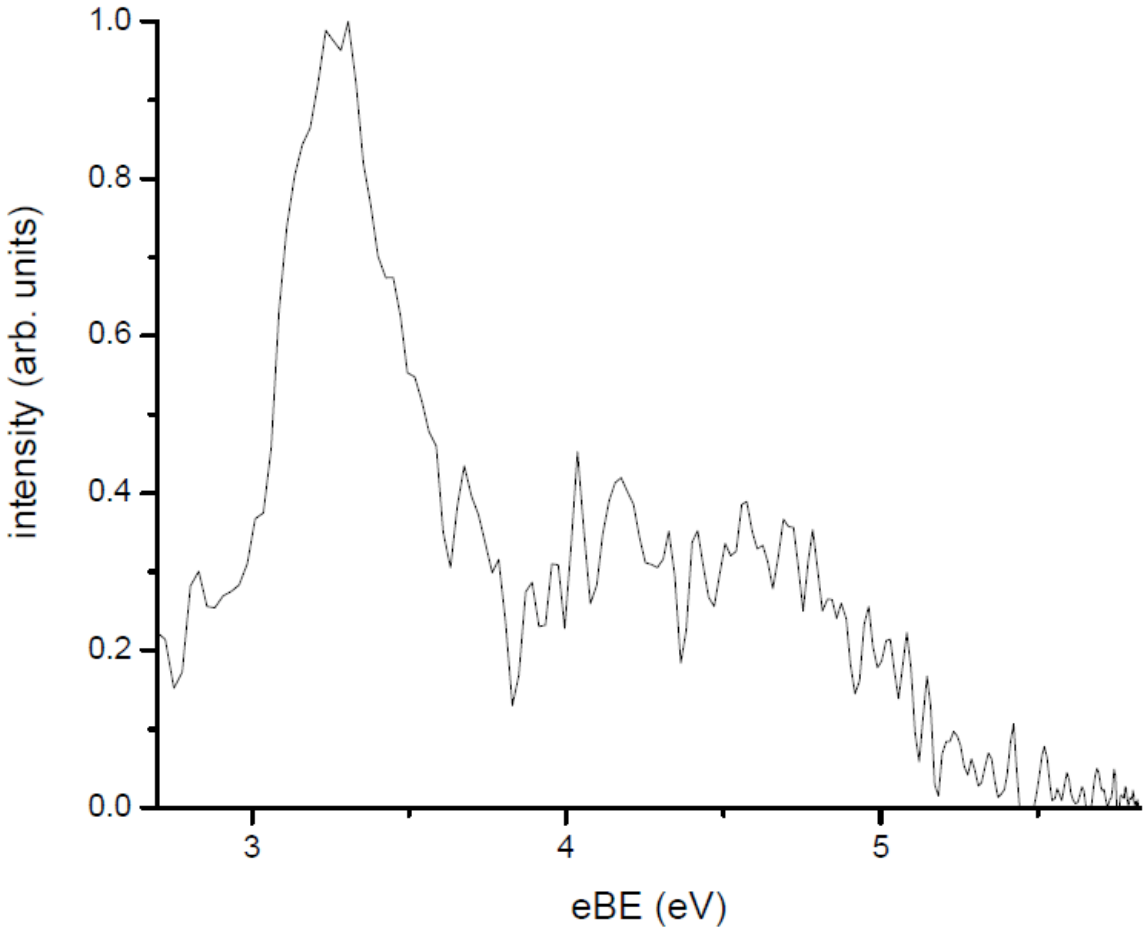

Figure 4.7 Structures of thymine and cytosine; Isomers and relative energetics of isomers of deprotonated thymine and deprotonated cytosine

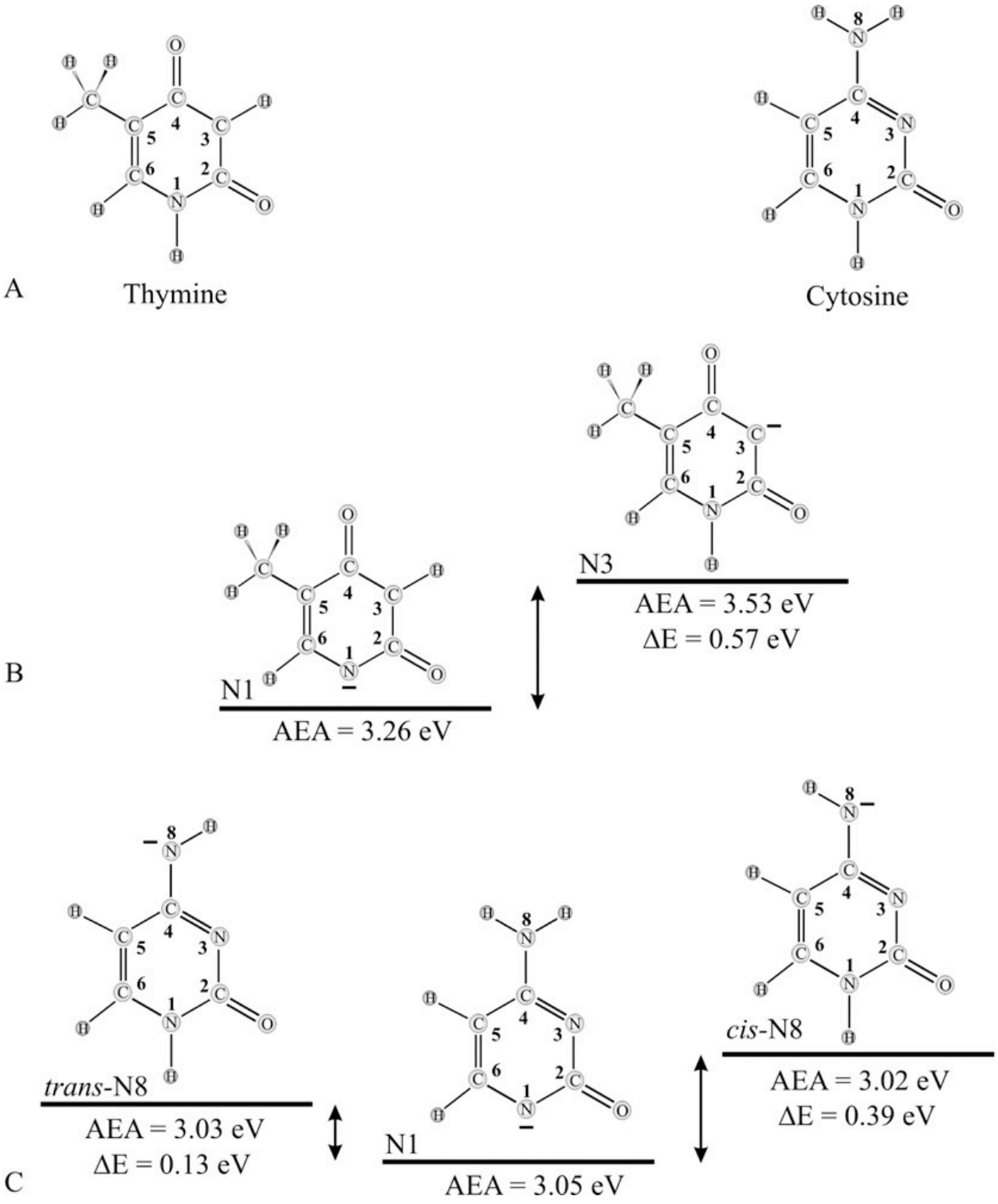

Chapter 5

Anion photoelectron spectroscopy at 118.2 nm (10.5 eV)

5.1 Introduction

Atomic and molecular clusters have attracted much interest because of the role they play as a conceptual bridge between isolated atoms and bulk matter. Semiconductor clusters, in particular indium phosphide (InP) clusters, are fascinating because of their size-dependent electrical and optical properties [1-3]. InP based materials have applications in various electronic and photonic devices used today, such as in high-quality fiber optics communication systems [4].

One of the main challenges in semiconductor cluster science is to understand how the electronic properties of clusters evolve over various size regimes. The electronic states of small clusters can be explained using standard molecular orbital pictures and quantum mechanical calculations. The electronic structure of nanocrystals and quantum dots, composed of hundreds or more atoms, is now well characterized both experimentally [3, 5] and theoretically [6, 7] thanks to recent successes in the synthesis of colloidal quantum dots. These nanocrystalline systems are understood to behave like perturbed bulk like species [8]. The behavior of clusters composed of 10-200 atoms, however, is more complicated, with little experimental information available. Understanding clusters in this size range can bridge the gap between the molecular and nanocrystalline size regimes and help answer the central question: how large does a cluster have to be before its electronic structure is better described using band structures rather than discrete molecular orbitals?

Photoelectron spectroscopy (PES) is a useful tool to study semiconductor clusters. Much of our knowledge of valence and core band structure in semiconductors comes from UV and X-ray PES studies [9, 10]. PES has also been instrumental in determining the properties and energetics of low-lying electronic states of the neutral clusters. Previous work on various semiconductor clusters using anion PES have been performed in this group and reported in various papers and theses [11-16]. Only a brief summary of the results on InP clusters will be presented here.

Rinnen, et al. [17] used photodissociation spectroscopy to collect absorption spectra on neutral In_xP_y clusters with $x + y = 5 - 14$ atoms. Xu, et al. [16] obtained photoelectron spectra for small $In_xP_y^-$ cluster anions (x, y = 1-4). For the neutral stoichiometric In_xP_x clusters, they observed HOMO-LUMO gaps that they speculated may be related to the bulk band gap, suggesting that the excess electron resided in the cluster analog of the conduction band. Asmis et al. [11] extended the study to InP cluster anions containing up to 27 atoms ($In_xP_x^-$, $In_{x+1}P_x^-$; x = 1-13) and found that the HOMO-LUMO gap of the neutral stoichiometric clusters were typically much smaller than the bulk band gap. They attributed this to the geometry of the gas-phase clusters they studied. A large fraction of the atoms comprising the neutral clusters examined were located on or close to the cluster 'surface', resulting in a large number of unoccupied low-lying surface states in which the excess electron could reside. These atoms tended to rearrange so as to minimize the number of dangling bonds, giving a non-crystalline

structure. Because of this, they concluded that the HOMO-LUMO gap in the clusters they studied was unlikely to correlate with the valence-conduction band gap of the bulk or nanocrystals. The extra electron in these bare InP clusters were more likely to reside in one of the localized surface states lying below the cluster analog of the conduction band.

In light of this, Meloni, et al. [12] undertook a different approach. They photodetached InP cluster anions containing up to 26 atoms further into the vacuum ultraviolet (157 nm, or 7.9 eV) and focused on comparing the more strongly bound molecular orbitals of the gas-phase clusters with the valence band structure of the bulk, which had been gleaned from bulk photoemission studies [10]. They observed a reasonable correlation in electronic structure between the photoelectron spectra they collected and the bulk photoemission spectrum of InP. However, at 157 nm, the photoelectron spectra only had two features that correlated with the first two bands of the bulk spectrum; to explore more structure, higher photon energies are required. The third band of the bulk spectrum is around 10 eV and electronic structure calculations indicate that the cluster equivalent lies around there as well. This state can be easily accessed with photons in the vacuum ultraviolet (VUV) spectral region, at 118.2 nm (10.5 eV). The following section describes how we make 118.2 nm.

5.2 VUV generation

5.2.1 Experimental setup

Details of the anion photoelectron spectrometer we use have been discussed previously [13-15]. As described, two electron detection schemes are possible – field-free time-of-flight (TOF) and a photoelectron imaging system utilizing the velocity-map imaging (VMI) technique. A schematic of the spectrometer is shown in Figure 1.

The imaging technique we use here to monitor the generation of 118.2 nm by detecting cations (initially) and electrons is based on that of Chandler and Houston [18] with the VMI modification of Eppink and Parker [19]. The imaging setup is very similar to that of Sanov [20] and Lineberger [21]. The electrons or cations are extracted by the imaging fields perpendicularly to the laser. The imaging stack is oriented vertically and consists of three 4.5” diameter stainless steel plates evenly spaced by 2 cm. Figure 2 shows a schematic diagram of the imaging setup.

To make 118.2 nm, we use a tripling cell and an optical arrangement that is shown in Figure 3. The VUV coherent radiation is generated by a nonresonant four-wave mixing (NFWM) process in a phase-matched condition in a Xe/Ar cell. In this cell, the 355 nm output of a Nd:YAG laser (Spectra-Physics Quanta-Ray Pro 290-30) is tripled. The 355 nm is focused by a fused silica lens (f = 30 cm at 355 nm) into the angled tripling cell (40 cm in length). A MgF_2 lens (f = 16 cm at 118 nm; f = 26.6 cm at 355 nm) and a gate valve separates the tripling cell from the high vacuum VMI detection chamber. The MgF_2 lens focuses the 118.2 nm output into the interaction zone between the extraction and repeller plates of the imaging setup. Since the focal length of the MgF_2 lens is longer at 355 nm, the 355 nm beam does not focus at the interaction zone. The tripling cell is angled to minimize back reflections of the 355 nm onto the fused silica lens. The cell is pumped by a 150 L/s turbomolecular pump (Leybold Turbovac 150); the pressure in the cell is measured by a Terranova Model 809 diaphragm gauge (Duniway Stockroom Corp.).

A mixing cylinder shown in Figure 4 was incorporated to improve the mixing of Xe and Ar in the tripling cell. It consists of a 1.5" O.D. nipple (MDC Vacuum Products, LLC) with two 2.75" O.D. conflat flanges and a MagiDrive rotary motion feed-through (Kurt J. Lesker Company Part #RMD20XD) coupled to and driven by an AC motor (WW Grainger Industrial Supply Part #3M577). A small fan is attached 1-2 cm into the nipple along the shaft of the rotary motion feed-through. Two gas lines are attached to the mixing cell – an inlet from the Xe and Ar gas cylinders and an outlet to the tripling cell.

Initially, we imaged NO^+ ions from ionizing nitric oxide (NO); the ionization energy of NO (from the NIST Chemistry WebBook) is 9.26420 ± 0.00002 eV. About 1 x 10^{-7} – 2 x 10^{-7} torr is released into the VMI detection chamber through a leak valve that is installed on a side flange.

When we found the experimental conditions that allowed us to achieve optimal conversion efficiency, we attempted to obtain a photoelectron spectrum of CN^- using VMI. CN^- anions are generated by entraining BrCN vapor from BrCN crystals in Ar and supersonically expanding the mixture through a pulsed piezoelectric nozzle followed by a high voltage discharge stabilized by a 1 keV electron beam. After collimation by a skimmer, the CN^- anions are extracted into a linear reflectron TOF mass spectrometer with a mass resolution ($m/\Delta m$) of 2000. Various ion optics steer the ion packet towards the interaction region between the center of the bottom plate (repeller) and the middle plate (extractor).

For detecting the NO^+ cations, voltages of +2000 V and +1400 – 1500 V are applied to the repeller and extractor, respectively, while the upper plate is held at ground. This way, the NO^+ ions we make accelerate toward the detector. The aperture of the middle and upper plates is 2.0 cm in diameter. The NO^+ ions are detected at the end of a 30 cm double μ-metal shielded flight tube by a 75 mm chevron MCP stack coupled to a phosphor screen (Burle Electro-Optics, Inc.). An externally triggered CCD camera (Dalsa) records one image per laser shot at 30 Hz. Typically our NO^+ images are summed for 200 shots (or frames).

For detecting electrons, negative voltages are applied to the repeller and extractor; the upper plate remains held at ground. This way, the photodetached electrons accelerate toward the detector and images are collected as aforementioned.

A pulsing scheme is applied to both the repeller voltage and to the MCPs to decrease background/noise signal. The back MCP is kept at a constant voltage of +1650 V. For NO^+ detection, the front MCP is pulsed from +400 V down to ground and the repeller voltage is pulsed from the extractor voltage up to its final voltage 500 ns before the population inversion builds up for each laser pulse. The front MCP is held at ground for 10 – 100 microseconds. For electron detection, the direction of the pulse is switched; the front MCP is pulsed from ground up to +400 V and the repeller voltage is pulsed from the extractor voltage down to its final voltage 40 ns before the arrival of CN^- ions.

The images we collect of the NO^+ ions and/or the detached electrons represent 2-D projections of the 3-D shells of ions and/or electrons. Normally, to convert the 2-D projection back into the 3-D distribution, we use the basis set expansion (BASEX) Abel transform method developed by Dribinski et al. [22]. We then angularly integrate over a slice of the reconstructed 3-D image along the plane of the detector to generate the photoelectron spectrum. For the NO^+ images we collect, we summed the raw 2-D projections using a summing program provided in Appendix 1. The images are essentially matrices whose entries represent signal intensity in arbitrary units. We typically then plot the image sums against the total pressure of gas in our tripling cell to find the conditions for maximal conversion efficiency.

5.2.2 Third harmonic generation in inert gases

The theory and technique of generating coherent 118.2 nm radiation is based on the concept of three 355 nm photons interacting with a dielectric medium (i.e. the inert gas) to produce a fourth, 118.2 nm, photon. The interaction is a nonlinear process that is traditionally modeled by expanding the induced polarization, $\vec{P}$, as a power series in electric field strength, $\vec{E}$ [23].

$$\vec{P} = \chi^{(1)} \cdot \vec{E} + \chi^{(2)} \cdot \vec{E}\vec{E} + \chi^{(3)} \cdot \vec{E}\vec{E}\vec{E} + \ldots \quad (1)$$

The expansion coefficients are known as nonlinear susceptibilities and measure how easily the gas mixture or nonlinear medium polarizes in response to the electric field. For third-harmonic generation, the third order nonlinear susceptibility $\chi^{(3)}$ is of utmost importance.

Substituting the expression for nonlinear polarization into Maxwell's equation and solving the set of coupled wave equations that result, we see that since the physical quantity we measure is the field intensity, the signal we observe will be proportional to $\left|\chi^{(3)}\right|^2$, the product of the three field intensities, and a phase-matching factor [23]. This last factor, the phase-matching factor, ensures efficient coupling between the UV photons. It allows for a proper phase relationship between the interacting waves, such that all the amplitude contributions are all in phase.

An effect that complicates phase-matching is the Kerr effect, which is a nonlinear optical effect in which the index of refraction changes in response to the intensity of an applied electric field. The induced index change is directly proportional to the square of the electric field.

To achieve phase-matching and efficient third-harmonic generation, we had an inert gas *mixture* in our tripling cell, namely a 1:10 Xe:Ar mixture. It has been shown that the conversion efficiency increases when one of the inert gases that make up the nonlinear medium is negatively dispersive [24]. This means that it has a refractive index at 355 nm (the fundamental) that is *greater* than its refractive index at 118.2 nm (the third-harmonic). Xe achieves negative dispersion by allowing the third-harmonic frequency (118.2 nm) to be greater than and relatively close to a transition that has a high oscillator strength (the $5p - 5d$ transition of Xe at 119.2 nm) [24]. With a negatively dispersive gas like Xe, we can add a positively dispersive gas like Ar to phase match and to allow tight focusing to the center of the tripling cell.

We calculated the power of VUV radiation from our NO ionization experiments using the equations on elastic and inelastic scattering in R.B. Bernstein's Chemical Dynamics via Molecular Beam and Laser Techniques [25]. We start with the general equation

$$I = n_1 n_2 v_r \Delta V \sigma \tag{2}$$

where I is the signal intensity, n_1 and n_2 are the number densities of Type 1 and Type 2 particles in the crossed beam zone of volume ΔV (in this case, the number density of VUV photons and NO molecules, respectively, in the VMI detection chamber), v_r the relative velocity (in this case, c, the speed of light), and σ is the integrated cross section for the ionization of NO ($1.24 \bullet 10^{-18}$ cm^2 at 121.6 nm).

We know our signal intensity I from our NO^+ images. It can be found by

$$I = \frac{x}{\Delta t} \tag{3}$$

where Δt is the interaction time and x is the number of NO^+ molecules detected per laser shot, defined by

$$x = \frac{\text{image sum}}{\text{\# of image frames} \cdot \text{ average count per ion}} \tag{4}$$

Thus

$$\frac{x}{\Delta t} = n_\gamma n_{NO} c V_{\text{int}} \sigma \tag{5}$$

or

$$n_\gamma = \frac{x}{n_{NO} c V_{\text{int}} \sigma \Delta t} \tag{6}$$

We can also find n_γ by

$$N_\gamma = n_\gamma V_\gamma \tag{7}$$

where N_γ is the number of VUV photons in a volume V_γ. Assuming the interaction between the NO molecule and the VUV photon occurs at the focus of the 118.2 nm, then the volume is given by

$$V_\gamma = \pi r_{bw}^2 c \Delta t \tag{8}$$

where r_{bw} is the beam waist radius of the 118.2 nm beam and given by

$$r_{bw} = \frac{\lambda f}{\pi a} \tag{9}$$

where f is the focal length of the lens and a is the radius of the beam on the lens.

We can thus find the number of VUV photons (and consequently the power of VUV) by

$$N_\gamma = \frac{x\pi r_{bw}^2}{n_{NO} V_{\text{int}} \sigma} \tag{10}$$

which is related to the power by

$$E_{VUV} = \frac{hc}{\lambda} N_\gamma \tag{11}$$

or

$$E_{118.2} = (1.68 \cdot 10^{-18}\,\text{Joules}) N_\gamma \tag{12}$$

The volume of the interaction region V_{int} can be found geometrically by estimating the region as two cones.

$$V_{\text{int}} = 2 \cdot (\tfrac{1}{3}\pi r^2 h) \tag{13}$$

where r can be found using similar triangles to give

$$r = \left(\frac{\tfrac{1}{2} \cdot \text{spot size of beam on } MgF_2 \text{ lens}}{44.5 \text{ cm}} \right) \cdot (\text{length of interaction region}) \tag{14}$$

For 202 pulses co-added, an image taken without phase matching, using an input power of 355 nm of ~ 3W, and having an image sum of 7.4 x 10^8 shots, we get

$x \sim 6.7 \times 10^4$

$r_{bw} \sim 2.9$ μm

$\eta_{NO} \sim 3.2 \times 10^9$ / cm^3

$V_{int} \sim 1.8 \times 10^{-4}$ cm^3

and ~ 40 nJ/pulse or 1.2 μW of 118 nm or a conversion efficiency of 4 x 10^{-7}.

5.2.3 Preliminary results using NO

Pressure studies are conducted to determine the experimental conditions under which optimal conversion efficiency is achieved. We collected images at increasing total pressure in the tripling cell (a metering valve allowed us to control the flow from the mixing cylinder into the gas cell), calculated the total counts of each image using the summing program described previously, and plotted the sum against the total pressure in the cell. We allowed 2 hours for the Xe and Ar to mix in the mixing cylinder prior to each pressure study. Figure 5 shows a sample plot of a pressure study conducted at 110 mJ/pulse of 355 nm. We achieved our optimal conversion efficiency ($2 \bullet 10^{-5}$) at 105-116 mJ/pulse of 355 nm with a total gas pressure of 150-200 torr Xe/Ar in 1:10 ratio. We estimate that this produces ~2.2 μJ/pulse (or ~10^{12} photons/pulse) 118.2 nm radiation. Figure 6 shows a raw image of NO^+ taken under these conditions.

5.2.4 Preliminary results using CN^-

Attempts were made at obtaining the photoelectron spectrum of CN^- at 118.2 nm before looking at InP clusters. We selected CN^- because its electronic structure is well characterized, it is easily made with our ion source, and its electron affinity (EA) is 3.862 eV, making the ion too high in energy to successfully detach at 355 nm (3.5 eV), but low enough to photodetach at 118.2 nm (10.5 eV). CN^- is thus a good molecule with which to calibrate our spectrometer. We were able to see 0.1-0.2% detachment at ~105 mJ/pulse and 100 torr Xe and Ar. Unfortunately, the photoelectron signal was overwhelmed by the large background signal from scattered radiation. Various attempts, including using the

modified VMI optics setup described in Section 4.2 in Chapter 4, were made to decrease the noise level with no success.

5.3 Conclusions

In conclusion, we have demonstrated the feasibility of generating coherent VUV radiation (118.2 nm) from tripling the 355 nm output of a Nd:YAG laser using a gas cell filled with Xe and Ar at a 1:10 ratio. NO^+ ions were imaged to determine the experimental conditions under which optimal maximum conversion is achieved. Unfortunately, due to significant background levels, we were unable to obtain a photoelectron spectrum of CN^- at 118.2 nm and consequently, we were unable to study the higher energy features of interest for InP clusters.

Acknowledgements

This work was supported by the National Science Foundation under grant number DMR-0505311.

References

1. Hatami, F., et al., *InP quantum dots embedded in GaP: optical properties and carrier dynamics.* Physical Review B (Condensed Matter and Materials Physics), 2003. **67**(8): p. 85306-1-85306-85306-8.
2. Kan, S., et al., *Synthesis and size-dependent properties of zinc-blende semiconductor quantum rods.* Nature Materials, 2003. **2**(3): p. 155-158.
3. Micic, O.I., et al., *Size-dependent spectroscopy of InP quantum dots.* Journal of Physical Chemistry B, 1997. **101**(25): p. 4904-4912.
4. Katz, A., ed. *Indium Phosphide and Related Materials: Processing, Technology and Devices*. 1992, Artech House: Norwood, MA.
5. Banin, U., et al., *Quantum confinement and ultrafast dephasing dynamics in InP nanocrystals.* Physical Review B, 1997. **55**(11): p. 7059-7067.
6. Fu, H.X. and A. Zunger, *Local-density-derived semiempirical nonlocal pseudopotentials for InP with applications to large quantum dots.* Physical Review B, 1997. **55**(3): p. 1642-1653.
7. Tomasulo, A. and M.V. Ramakrishna, *Quantum confinement effects in semiconductor clusters .2.* Journal of Chemical Physics, 1996. **105**(9): p. 3612-3626.
8. Alivisatos, A.P., *Perspectives on the physical chemistry of semiconductor nanocrystals.* Journal of Physical Chemistry, 1996. **100**(31): p. 13226-13239.
9. Ley, L., et al., *TOTAL VALENCE-BAND DENSITIES OF STATES OF III-V AND II-VI COMPOUNDS FROM X-RAY PHOTOEMISSION SPECTROSCOPY.* Physical Review B, 1974. **9**(2): p. 600-621.
10. Vesely, C.J. and D.L. Kingston, *VALENCE-BAND DENSITY OF STATES OF INP AND GASB AS DETERMINED BY X-RAY PHOTOEMISSION.* Physical Review B, 1973. **8**(6): p. 2685-2687.
11. Asmis, K.R., T.R. Taylor, and D.M. Neumark, *Electronic structure of indium phosphide clusters: anion photoelectron spectroscopy of InxPx- and Inx+1Px- (x=1-13) clusters.* Chemical Physics Letters, 1999. **308**(5-6): p. 347-354.
12. Meloni, G., et al., *Probing the connection between cluster and bulk electronic structure of InP using vacuum ultraviolet anion photoelectron spectroscopy.* Chemical Physics Letters, 2004. **392**(1-3): p. 90-94.
13. Meloni, G., et al., *Spectroscopic investigation of Al2N and its anion via negative ion photoelectron spectroscopy.* Journal of Physical Chemistry A, 2006. **110**(10): p. 3527-3532.
14. Sheehan, S.M., et al., *Spectroscopic characterization of the ground and low-lying electronic states of Ga2N via anion photoelectron spectroscopy.* Journal of Chemical Physics, 2006. **124**(6): p. 7.
15. Xu, C.S., et al., *Photoelectron spectroscopy of C-4(-), C-6(-), and C-8(-).* Journal of Chemical Physics, 1997. **107**(9): p. 3428-3436.
16. Xu, C.S., et al., *ANION PHOTOELECTRON-SPECTROSCOPY OF SMALL INDIUM-PHOSPHIDE CLUSTERS (INXPY-X,Y=1-4).* Journal of Chemical Physics, 1994. **101**(6): p. 5406-5409.
17. Rinnen, K.D., et al., *DIRECT INFRARED AND VISIBLE ABSORPTION-SPECTROSCOPY OF STOICHIOMETRIC AND NONSTOICHIOMETRIC*

CLUSTERS OF INDIUM-PHOSPHIDE. Journal of Chemical Physics, 1992. **96**(6): p. 4088-4101.
18. Chandler, D.W. and P.L. Houston, *TWO-DIMENSIONAL IMAGING OF STATE-SELECTED PHOTODISSOCIATION PRODUCTS DETECTED BY MULTIPHOTON IONIZATION.* Journal of Chemical Physics, 1987. **87**(2): p. 1445-1447.
19. Eppink, A. and D.H. Parker, *Velocity map imaging of ions and electrons using electrostatic lenses: Application in photoelectron and photofragment ion imaging of molecular oxygen.* Review of Scientific Instruments, 1997. **68**(9): p. 3477-3484.
20. Surber, E., R. Mabbs, and A. Sanov, *Probing the electronic structure of small molecular anions by photoelectron imaging.* Journal of Physical Chemistry A, 2003. **107**(40): p. 8215-8224.
21. Rathbone, G.J., et al., *Photoelectron imaging spectroscopy of Cu-(H2O)1,2anion complexes.* Chemical Physics Letters, 2005. **401**(4-6): p. 570-574.
22. Dribinski, V., et al., *Reconstruction of abel-transformable images: The Gaussian basis-set expansion abel transform method.* Review of Scientific Instruments, 2002. **73**(7): p. 2634-2642.
23. Thiel, C.W. *Four-Wave Mixing and its Applications*. **Volume**,
24. Kung, A.H., J.F. Young, and S.E. Harris, *GENERATION OF 1182-A RADIATION IN PHASE-MATCHED MIXTURES OF INERT-GASES.* Applied Physics Letters, 1973. **22**(6): p. 301-302.
25. Bernstein, R.B., *Chemical Dynamics via Molecular Beam and Laser Techniques*. 1982, New York, NY: Oxford University Press.

Figure 5.1 Anion photoelectron spectrometer

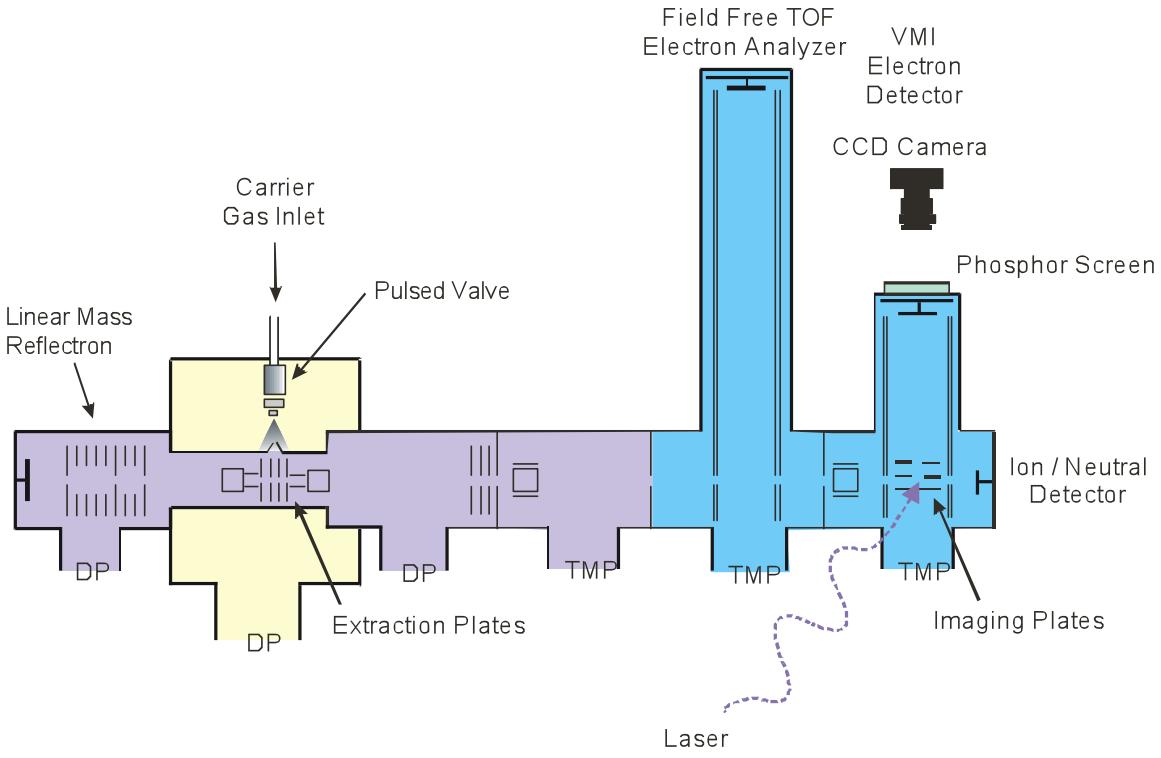

Figure 5.2 Velocity-map imaging optics setup to image NO^+

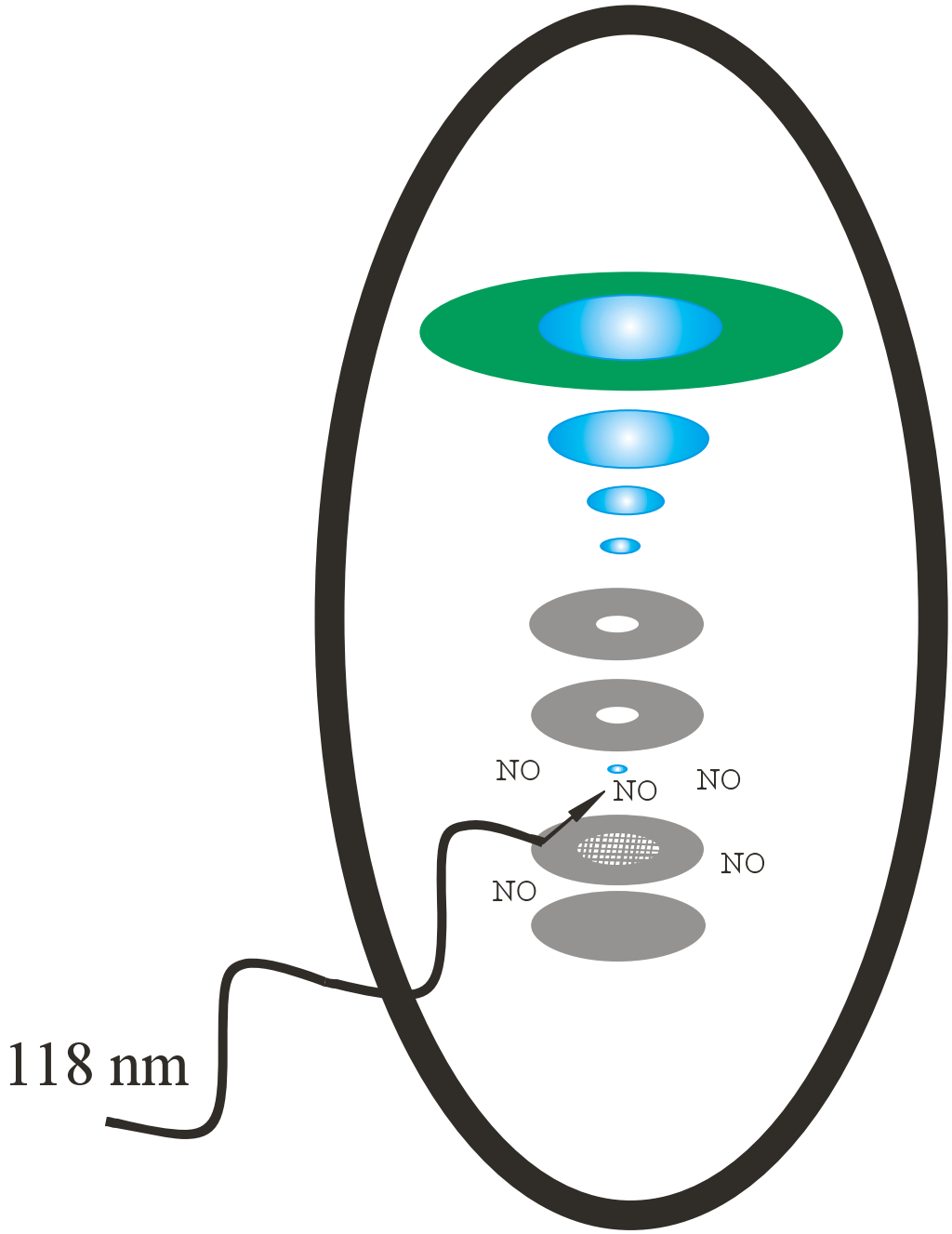

Figure 5.3 Schematic diagram of gas mixture tripling cell

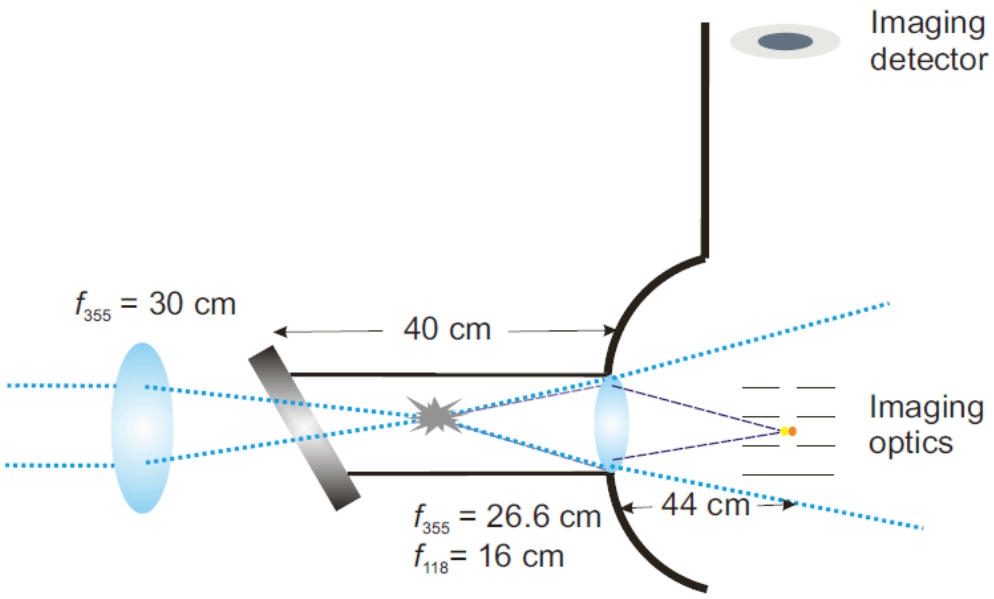

Figure 5.4 Schematic diagram of mixing cylinder

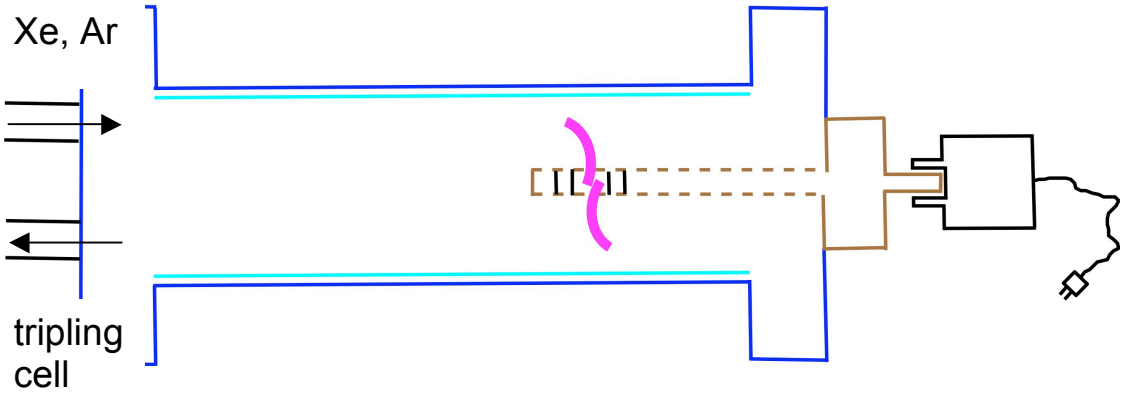

Figure 5.5 Pressure study for 1:10 Xe:Ar mix at 110 mJ/pulse of UV

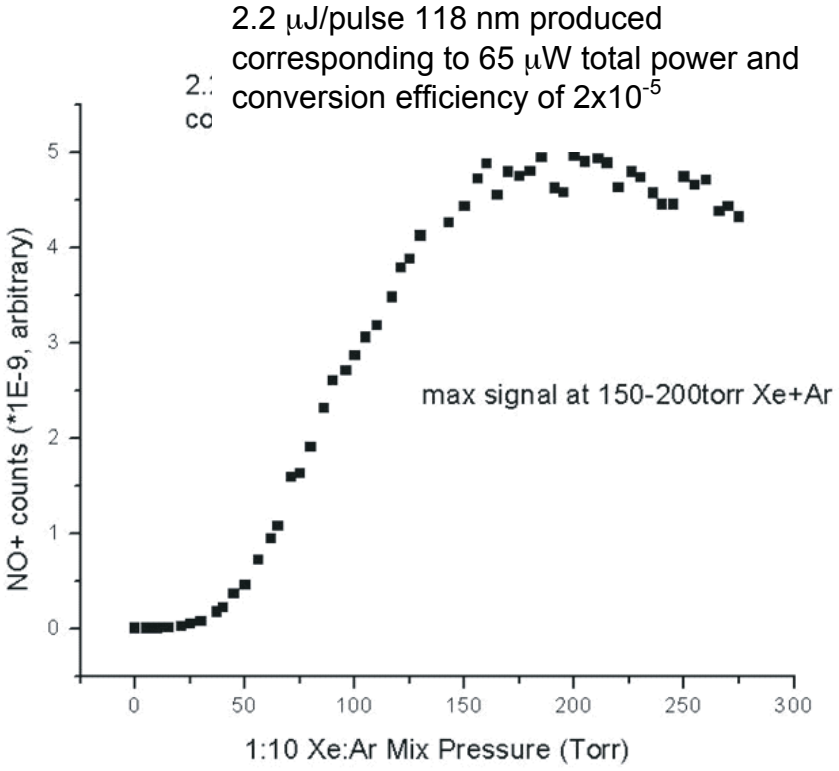

Figure 5.6 Sample raw image of NO^+ obtained with an input of 110 mJ/pulse 355 nm

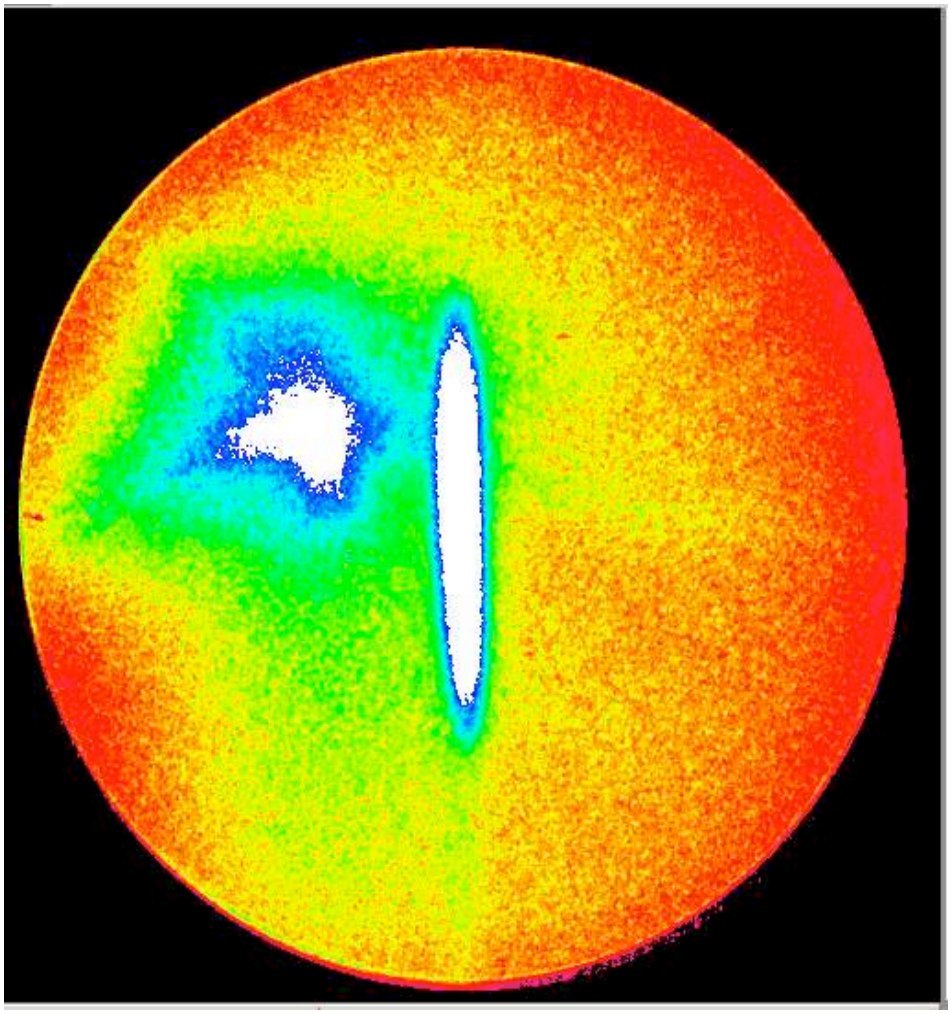

Chapter 6

Anion Photoelectron Spectroscopy of C_3N^- and C_5N^- *

Anion photoelectron spectroscopy of C_3N^- and C_5N^- is performed using slow electron velocity-map imaging (SEVI) and field-free time-of-flight (TOF), respectively. From the SEVI spectrum, we observe and assign well-resolved vibrational transitions from the linear C_3N^- ground state to the corresponding C_3N ground state. From the TOF spectra, we observe transitions arising from the linear C_5N^- ground state to the corresponding neutral ground and excited states. This study yields the adiabatic electron affinities of C_3N and C_5N to be 4.305±0.001 eV and 4.45±0.03 eV, respectively, and a term value of 560±120 cm^{-1} for the $\tilde{A}\,^2\Pi$ state of C_5N. Vibrational frequencies for the degenerate cis and trans bending modes of C_3N^- are also extracted.

* Published work

6.1 Introduction

The recent discoveries of the C_3N and C_5N radicals[1,2] and of the C_3N^- and C_5N^- anions[3,4] in circumstellar envelopes have prompted much interest in characterizing the properties of the linear carbon chains of the type $C_{2n+1}N$. In particular, the C_3N radical and C_3N^- anion are key cyanopolyacetylides and important drivers of interstellar chemistry. They are also potentially significant constituents of Titan's ionosphere.[5] The neutral C_3N and C_5N radicals and their anionic counterparts were discovered in the expanding circumstellar envelope of the carbon star IRC + 10216 and in the dark cloud TMC1 with radio telescopes. The interstellar detection of C_3N was confirmed by the observation of the radical in the low-pressure laboratory gas discharge of cyanoacetylene in nitrogen;[6] the corresponding anionic species, C_3N^-, has also been successfully made in the laboratory and has been the subject of a considerable amount of theoretical and experimental effort. Following theoretical predictions by Botschwina[7], the microwave spectrum of C_5N was measured,[8] yielding its rotational, fine and hyperfine constants; likewise, the assignment of the B1389 series garnered from the spectral line survey[4] of IRC +10216 to C_5N^- was significantly aided and confirmed by electronic structure calcuations.[9] The astrophysical relevance of the neutral and anionic species motivate the work described here, in which we report photoelectron spectra of C_3N^- and C_5N^-.

Neutral C_3N is the best-characterized of these species. Since Gottlieb et al.[6] found C_3N in the interstellar medium by characterizing the rotational spectrum of the $\tilde{X}\,^2\Sigma^+$ ground state of C_3N, several infrared and higher-resolution microwave studies have been performed.[3,10-13] Infrared vibrational transitions of C_3N^- produced in rare gas solids via cyanoacetylene dissociation have been reported,[14,15] while high-resolution rotational transitions of C_3N^- produced by discharging a HC_3N:HC_4H gas mixture were observed by McCarthy[12] using Fourier transform microwave spectroscopy. An earlier joint experimental/theoretical study[16] produced millimeter-wave rotational spectra of the ^{13}C isotopic species of C_3N. Endo[11] observed the $\tilde{B}\,^2\Pi$ - $\tilde{X}\,^2\Sigma^+$ transition by laser induced fluorescence spectroscopy (LIF) and the $\tilde{A}\,^2\Pi$ – $\tilde{X}\,^2\Sigma^+$ transition from dispersed fluorescence (DF). The origin of the $\tilde{A}\,^2\Pi$ state was determined to lie 1844(3) cm^{-1} above the ground state and the $\tilde{B}\,^2\Pi$ state was found to be 27929.985(2) cm^{-1} above the ground state. Graupner et al.[17] obtained an electron affinity of C_3N of 4.59±0.25 eV by dissociative electron attachment to HC_3N.

There have been several electronic structure calculations predicting the energetics, geometries, infrared vibrational frequencies, and microwave rotational transitions of C_3N and C_3N^-.[14,16,18-21] All predict linear structures for the $\tilde{X}\,^1\Sigma^+$ ground state of C_3N^- and the $\tilde{X}\,^2\Sigma^+$ ground state of C_3N. The equilibrium electron affinity of C_3N was recently calculated[14] to be 4.34 eV, ~0.25 eV lower than the experimental value;[17] inclusion of zero point energies in the calculation increases this discrepancy slightly.

Fewer spectroscopic studies have been reported for C_5N and C_5N^-. The microwave spectrum of C_5N measured by Kasai et al[8] showed that it was linear with an $\tilde{X}\,^2\Sigma^+$ ground state. Maier[22] obtained the electronic absorption spectrum of C_5N in a cryogenic matrix by deposition of mass-selected C_5N^- followed by ultraviolet photodetachment, yielding a band around 470 nm that was assigned to the $\tilde{B}\,^2\Pi \leftarrow \tilde{X}\,^2\Sigma^+$ transition of C_5N. The IR absorption spectra of C_5N^- generated from vacuum-UV photolysis of cyanodiacetylene (HC_5N) in solid argon has also been identified.[23]

Electronic structure calculations have been reported for C_5N and C_5N^-. Pauzat et al.[24] performed unrestricted Hartree-Fock self-consistent field (UHF-SCF) calculations on the radical that gave an electronic ground state with $^2\Pi$ symmetry. Subsequent coupled cluster calculations by Botschwina[7,21] disagreed with this result and predicted the electronic ground state of C_5N to have $^2\Sigma^+$ symmetry, with the $^2\Pi$ state lying ~500 cm^{-1} higher in energy. As for the C_5N^- anionic species, Zhan and Iwata[25,26] conducted calculations using Moller-Plesset (MP2) perturbation theory with a 6-31G(d) basis set for anions up to C_7N^- and reported harmonic vibrational frequencies, vertical detachment energies (VDEs), and equilibrium structures. From the optimized geometries of C_nN^- (n = 4 – 7) in their ground states, they found that only C_5N^- was linear in its ground state. Later work by Pascoli and Lavendy[27] using density functional theory disagreed with this result and found that all C_nN^- clusters have linear ground state structures. Very recently, Botschwina and Oswald[9] carried out an extensive theoretical study of the $C_{2n+1}N^-$ anions with n = 2 – 6 using coupled cluster theory in conjunction with a large basis set that confirmed a linear $^2\Sigma^+$ ground state of the C_5N radical and predicted the equilibrium geometry and the harmonic vibrational frequencies (among other spectroscopic constants) for C_5N^-. The electron affinity of C_5N was calculated to be 4.453 eV.[7]

In this paper, we report anion photoelectron spectra of C_3N^- and C_5N^- obtained with high-resolution slow velocity-map imaging (SEVI) and time-of-flight photoelectron (TOF-PE) spectroscopy. The C_3N^- SEVI spectrum was taken at the photodetachment wavelength 283 nm (4.382 eV) and shows well-resolved transitions to the neutral $\tilde{X}\,^2\Sigma^+$ ground state. Franck-Condon (FC) simulations were used to make vibrational assignments within this electronic transition. The TOF-PE C_5N^- spectrum was taken at 213 nm (5.822 eV) and shows broad transitions assigned to the neutral $\tilde{X}\,^2\Sigma^+$ ground and $\tilde{A}\,^2\Pi$ excited states. Experimental adiabatic electron affinities of C_3N and C_5N are determined, along with several anion and neutral vibrational frequencies.

6.2 Experimental

Photoelectron spectra of C_3N^- and C_5N^- were measured using two spectrometers that employ different electron detection techniques. In our time-of-flight photoelectron (TOF-PE) spectrometer, anions photodetached using a fixed-frequency laser and

photoelectrons detected at the end of a field-free time-of-flight (TOF) tube.[28,29] The slow electron velocity-map imaging (SEVI) spectrometer[30-32] yields higher-resolution spectra by photodetaching anions near threshold with a tunable laser and detecting resulting slow photoelectrons using collinear velocity-map imaging.[33] The TOF-PE instrument produces spectra over a wide range of electron kinetic energy with a resolution of 8-10 meV and can operate more easily at higher photon energy, while the SEVI spectrometer yields spectra over a more limited range of electron kinetic energy, but with a resolution as high as ~2 cm^{-1}. C_3N^- was investigated on the SEVI instrument, while the photoelectron spectrum of C_5N^-, with a somewhat higher electron binding energy, was taken on the TOF-PE spectrometer.

In the SEVI spectrometer, C_3N^- anions were produced from a gas mixture of 0.05% acetylene and 2% N_2O in a balance of argon, which was supersonically expanded into the source vacuum chamber through an Even-Lavie pulsed valve.[34] Anions were formed by a discharge source that has been described in detail in our previous work on $C_{2n}N^-$ ions.[35] Briefly, the gas mixture was passed through a pair of fine stainless steel meshes separated by 1 mm. An electric discharge was induced by the passage of the gas pulse. This grid discharge source generates cold ions, allowing SEVI to achieve high resolution.

The C_3N^- anions created in the source were injected into a Wiley-McLaren TOF mass spectrometer ($m/\Delta m = 400$)[36] and steered to the interaction region through a series of electrostatic lenses and pinholes. At the interaction region, anions were detached between the extractor and repeller plates of a collinear velocity-map imaging (VMI) stack by a Nd:YAG-pumped tunable dye laser. The resulting photoelectron cloud was then uniformly accelerated and mapped onto a chevron-mounted pair of time-gated, imaging quality MCPs coupled to a phosphor screen.[37] Electron hits were recorded using a charge-coupled device (CCD) camera and sent to a computer. Images were collected over 50,000 laser shots, quadrant symmetrized, and inverse-Abel transformed[38] to obtain a 2D slice through the reconstructed 3D photoelectron velocity distribution, and then angularly integrated to obtain the photoelectron spectra. The spectra presented here are plotted with respect to electron binding energy (eBE), which is the difference between the incident photon energy and the measured electron kinetic energy. The photoelectron angular distribution (PAD) is given by Eq. (1) below and was determined directly from the images.

In the TOF-PE spectrometer, C_5N^- anions were generated from cyanoacetylene (synthesized using standard methods[39]) entrained in 10 psi of a <1% acetylene: 4.7% NF_3: 94.3% Ar gas mixture. The gas was supersonically expanded through a pulsed piezoelectric nozzle followed by a high voltage discharge at ~-700-800V that was stabilized by a 1 keV electron beam. After collimation by a skimmer, anions were injected into a Wiley-McLaren/linear reflection time-of-flight mass spectrometer ($m/\Delta m = 2000$),[40] and photodetached at213 nm (5.82 eV), the 5th harmonic of a pulsed Nd:YAG laser. A small fraction of these electrons was detected by a pair of chevron-mounted microchannel plates (MCPs) at the end of a ~1 m long, magnetically shielded flight tube perpendicular to both the molecular and laser beams. A typical spectrum resulted from collecting 180,000 laser shots.

PAD's were obtained by measuring spectra at laser polarization angles θ = 0° or 90° with respect to the TOF axis. The PAD is given by[41,42]

$$\frac{d\sigma}{d\Omega} = \frac{\sigma_{total}}{4\pi}[1 + \frac{\beta}{2}(3\cos^2\theta - 1)] \quad (1)$$

where σ_{total} is the total photodetachment cross section. β is the anisotropy parameter, which varies from -1 to 2 and is given for each feature by

$$\beta = \frac{I_{0^\circ} - I_{90^\circ}}{\frac{1}{2}I_{0^\circ} + I_{90^\circ}} \quad (2)$$

where I_0° and I_{90}° are the intensities of the peak taken at laser polarization angles of 0° and 90° respectively.

6.3 Results

Figure 6.1 presents the SEVI spectrum of C_3N^- taken at 283 nm (4.381 eV), plotted in eBE from 4.240 to 4.360 eV. Peak X_0 at 4.305 eV dominates, followed by four small peaks *a-d* at slightly lower eBE and one smaller peak, X_1, lying at 35meV higher eBE than X_0. All peaks have anisotropy parameters of 0-5-0.6, as seen in Table 6.1.

TOF-PE spectra of C_5N^- taken at 213 nm are shown in Figure 6.2, with the spectrum at laser polarization angle of 0° (in gray) overlaid on the spectrum at 90° (in black). The spectra are plotted in eBE between 4.20 and 5.00 eV and intensities are scaled relative to the raw TOF data. No features were seen below 4.30 eV; at higher eBE, four fairly broad peaks, A, B, C and D are seen. Table 6.2 lists the anisotropy parameters of these peaks. Features A and D, centered at ~4.45 eV and ~4.80 eV respectively, are slightly more intense at θ = 0° with β=0.1-0.2, while peak B and the shoulder C at ~4.52 and ~4.76 eV isotropic (β=0) with intensities that are insensitive to the laser polarization angle.

6.4 Discussion

6.4.1 Vibrational assignments of SEVI spectrum of C_3N^-

In Figure 6.1, peak X_0 is clearly the vibrational origin, and the dominance of this feature indicates that there is relatively little geometry change upon photodetachment of C_3N^-. The smaller peaks can be assigned with reference to the previously calculated results for the anion and neutral summarized in Table 6.3. Peaks *a-d*, which occur at lower eBE than X_0, must arise from vibrationally excited anion levels, most likely the low-frequency ν_4 and ν_5 bending modes. In the photoelectron spectrum, only even $\Delta\nu$ transitions are allowed for these two non-totally symmetric modes, suggesting that these peaks are sequence band ($\Delta\nu$=0) transitions from bend-excited states whose displacement from the origin reflects differences in the anion and neutral vibrational frequencies.

To confirm this assignment, Franck-Condon (FC) simulations of the degenerate bending modes were employed. These simulations were carried out treating each mode as an independent harmonic oscillator and using the parallel mode approximation, which neglects Duschinsky rotation[43] between the modes. The vibrational temperature and the known calculated and experimental anion and neutral vibrational frequencies were used as inputs into the PESCAL program by Ervin and co-workers[44-46] This program uses the recursion relation method of Hutchisson[47] to calculate the FC factors and output a simulated photoelectron spectrum.

Figure 6.1 compares the SEVI spectrum with the stick and convoluted FC simulations of the $\tilde{X}\,^2\Sigma^+ \leftarrow \tilde{X}\,^1\Sigma^+$ transition. The origin of the simulation was chosen to match X_0, the expected vibrational origin of the spectrum. Table 6.1 gives peak assignments from the simulation. As inputs for the simulation, we used vibrational temperatures of 350 K for ν_4 and 100 K for ν_5, experimental values[11] for the ν_4 and ν_5 fundamental transitions in the ground state of the neutral C_3N, and, initially, calculated values[14] for ν_4 and ν_5 of the ground state of C_3N^- that were modified to produce a better fit. The optimized values for the ν_4 and ν_5 bending modes in C_3N^- obtained from this procedure are 538±8 cm^{-1} and 208±8 cm^{-1}, as listed in Table 6.3. These values agree with the RCCSD(T) calculations.[14]

The simulated spectrum matches our spectrum quite well with all the major peaks reproduced. Peaks *d*, *c*, *b*, and *a* are assigned to the $\Delta\nu$=0 sequence of ν_4 and ν_5, with peak *a* the 5_1^1 transition, peak *b* the 4_1^1 band, peak *c* the $4_1^1 5_1^1$ combination band, and peak *d* the 4_2^2 transition. Peak X_1, 274 cm^{-1} above the origin, is assigned to the 5_0^2 transition; this displacement agrees with that observed previously via dispersed fluorescence from the $\tilde{B}$ state of C_3N[11], within the error bars of our experiment. From the eBE of the band origin,

peak X_0, we obtain the electron affinity (EA) of C_3N, 4.305±0.001eV. As seen in Table 6.4, this value is close to but lower than the calculated equilibrium EA of 4.344 eV.[14]

6.4.2 Band assignments of TOF-PE spectrum of C_5N^-

The TOF-PE spectrum of C_5N^- can be tentatively assigned with reference to the experimental and calculated geometries and frequencies summarized in Table 6.5 and energetics in Table 6.6. Peaks A and B are separated by ~560 cm^{-1} and do not appear to be the start of a vibrational progression as there are only two peaks. However, the spacing is very close to the calculated energy splitting between the neutral $\tilde{X}\,^2\Sigma^+$ ground and $\tilde{A}\,^2\Pi$ excited states[7] of 500 cm^{-1} (Table 6.6). In addition, peaks A and B have slightly different PADs (Table 6.2). Hence, we attribute peaks A and B to the vibrational origins of the neutral $\tilde{X}\,^2\Sigma^+$ and $\tilde{A}\,^2\Pi$ states, respectively. This assignment of peak A gives EA (C_5N) = 4.45±0.03 eV, which is in close agreement with the calculated value of 4.453 eV (see Table 6.6).[7]

Peaks C and D then appear to be transitions to vibrationally excited levels of one or both of these states. To try to assign these features, and since no experimental or vibrational frequencies were available for the $\tilde{A}\,^2\Pi$ state, electronic structure calculations were performed on neutral and anionic C_5N. Density functional calculations were performed using the Becke three-parameter Lee-Yang-Parr exchange-correlation functional[48,49] (B3LYP) with the augmented correlation consistent polarized valence triple-zeta set[50] (aug-cc-pVTZ). All calculations were carried out using the GAUSSIAN03 program.[51] Table 6.5 compares our calculations to previous values; we report only the frequencies of the stretching modes of the $\tilde{A}\,^2\Pi$ state.

For the C_5N^- $\tilde{X}\,^1\Sigma^+$ state, our optimized geometry and calculated vibrational frequencies match up reasonably well with the values reported by Botschwina and Oswald[9] that were obtained using CCSD(T)/cc-pVQZ for all atoms plus the aug-cc-pVQZ for the terminal atoms. Our B3LYP frequencies are within 50 cm^{-1} and our bond lengths within 0.008 Å. Detachment from the nonbonding σ orbital on the terminal carbon leads to the neutral $\tilde{X}\,^2\Sigma^+$ state. Our optimized geometry and calculated harmonic vibrational frequencies for the stretching modes of this state C_5N match up with the RCCSD(T) calculations of Botschwina.[7] Our B3LYP frequencies for the five stretches of C_5N are within 50 cm^{-1} and our bond lengths within 0.01 Å. Detachment from a π orbital leads to the $\tilde{A}\,^2\Pi$ state of the neutral species which was also calculated to be linear.[7] Our optimized bond lengths for this state are within 0.02 Å of that work.

The spacing between peaks A and C is 0.31±0.015 eV (2500 cm^{-1}), which is larger than any fundamental frequencies of the neutral $\tilde{X}\,^2\Sigma^+$ state. However, our

calculated frequency of 1906 cm^{-1} for the ν_3 stretching mode of the neutral $\tilde{A}\,^2\Pi$ state is close to the spacing of 0.24±0.015 eV (1940 cm^{-1}) between peaks B and C. Peak D is 0.28±0.015 eV (2260) cm^{-1} higher in eBE than peak B, close to our calculated frequency of 2215 cm^{-1} for the ν_1 stretching mode. Moreover, Table 6.2 shows that B, C, and D have roughly the same PADs. We thus tentatively assign peaks B, C, and D as the vibrational origin, 3_0^1, and 1_0^1 photodetachment transitions to the $\tilde{A}\,^2\Pi$ state.

The peaks in the TOF-PE spectrum of C_5N^- are surprisingly broad, considering that the anion and neutral are expected to be linear.[7,9,22] The peak widths may reflect a high anion vibrational temperature, resulting in spectral congestion from Δv=0 sequence bands originating from vibrationally excited bending levels of the anion, several of which have quite low frequencies (Table 6.5, first row). The resulting sequence bands would not be resolved in the TOF-PE spectra, in contrast to the higher resolution SEVI spectrum of C_3N^-. In addition, the closely spaced $\tilde{X}\,^2\Sigma^+$ and $\tilde{A}\,^2\Pi$ states of C_5N will be vibronically coupled via the bending modes, all of which have π symmetry, resulting in activation of normally forbidden Δv=1 transitions in these modes for photodetachment to both neutral states.[52] Such transitions, again involving low-frequency modes, will result in further spectral congestion.

6.5 Conclusions

Photoelectron spectra of C_3N^- and C_5N^- were obtained using slow electron velocity-map imaging (SEVI) and TOF photoelectron (TOF-PE) spectroscopy, respectively. From the SEVI spectrum, vibrational transitions to the ground $\tilde{X}\,^2\Sigma^+$ state of neutral C_3N were resolved, allowing accurate experimental determinations of the electron affinity of C_3N, 4.305±0.001 eV as well as frequencies of the degenerate bending modes of C_3N^-. The poorer quality of the C_5N^- TOF-PE spectra allowed only a tentative assignment of the observed features to the ground $\tilde{X}\,^2\Sigma^+$ and low-lying $\tilde{A}\,^2\Pi$ states, as well as to vibrational features of the $\tilde{A}\,^2\Pi$ state. This assignment yields an electron affinity of 4.45±0.03 eV for C_5N and a term value of 560±120 cm^{-1} for the $\tilde{A}\,^2\Pi$ state.

Acknowledgements

This work was supported by the National Science Foundation under Grant No. CHE-0649647. E.G. thanks the National Science and Engineering Research Council of Canada (NSERC) for a post-graduate scholarship.

References

(1) Guelin, M.; Thaddeus, P. *Astrophys. J.* **1977**, *212*, L81.

(2) Guelin, M.; Neininger, N.; Cernicharo, J. *Astron. Astrophys.* **1998**, *335*, L1.

(3) Thaddeus, P.; Gottlieb, C. A.; Gupta, H.; Brunken, S.; McCarthy, M. C.; Agundez, M.; Guelin, M.; Cernicharo, J. *Astrophys. J.* **2008**, *677*, 1132.

(4) Cernicharo, J.; Guelin, M.; Agundez, M.; McCarthy, M. C.; Thaddeus, P. *Astrophys. J.* **2008**, *688*, L83.

(5) Coates, A. J.; Crary, F. J.; Lewis, G. R.; Young, D. T.; Waite, J. H.; Sittler, E. C. *Geophys. Res. Lett.* **2007**, *34*, 6.

(6) Gottlieb, C. A.; Gottlieb, E. W.; Thaddeus, P.; Kawamura, H. *Astrophys. J.* **1983**, *275*, 916.

(7) Botschwina, P. *Chem. Phys. Lett.* **1996**, *259*, 627.

(8) Kasai, Y.; Sumiyoshi, Y.; Endo, Y.; Kawaguchi, K. *Astrophys. J.* **1997**, *477*, L65.

(9) Botschwina, P.; Oswald, R. *J. Chem. Phys.* **2008**, *129*, 11.

(10) Guennoun, Z.; Couturier-Tamburelli, I.; Pietri, N.; Aycard, J. P. *Chem. Phys. Lett.* **2003**, *368*, 574.

(11) Hoshina, K.; Endo, Y. *J. Chem. Phys.* **2007**, *127*, 12.

(12) McCarthy, M. C.; Thaddeus, P. *J. Chem. Phys.* **2008**, *129*, 6.

(13) Crepin, C.; Moneron, L.; Douin, S.; Boye-Peronne, S.; Kolos, R.; Turowski, M.; Gronowski, M.; Sepiol, J.; Benilan, Y.; Gazeau, M. C. *Pol. J. Chem.* **2008**, *82*, 741.

(14) Kolos, R.; Gronowski, M.; Botschwina, P. *J. Chem. Phys.* **2008**, *128*, 11.

(15) Khriachtchev, L.; Lignell, A.; Tanskanen, H.; Lundell, J.; Kiljunen, H.; Rasanen, M. *J. Phys. Chem. A* **2006**, *110*, 11876.

(16) McCarthy, M. C.; Gottlieb, C. A.; Thaddeus, P.; Horn, M.; Botschwina, P. *J. Chem. Phys.* **1995**, *103*, 7820.

(17) Graupner, K.; Merrigan, T. L.; Field, T. A.; Youngs, T. G. A.; Marr, P. C. *New J. Phys.* **2006**, *8*, 17.

(18) Botschwina, P.; Horn, M.; Flugge, J.; Seeger, S. *J. Chem. Soc. Faraday Trans.* **1993**, *89*, 2219.

(19) Sadlej, J.; Roos, B. O. *Chem. Phys. Lett.* **1991**, *180*, 81.

(20) Francisco, J. S. *Chem. Phys. Lett.* **2000**, *324*, 307.

(21) Botschwina, P. *Phys. Chem. Chem. Phys.* **2003**, *5*, 3337.

(22) Grutter, M.; Wyss, M.; Maier, J. P. *J. Chem. Phys.* **1999**, *110*, 1492.

(23) Coupeaud, A.; Turowski, M.; Gronowski, M.; Pietri, N.; Couturier-Tamburelli, I.; Kolos, R.; Aycard, J. P. *J. Chem. Phys.* **2008**, *128*.

(24) Pauzat, F.; Ellinger, Y.; McLean, A. D. *Astrophys. J.* **1991**, *369*, L13.

(25) Zhan, C. G.; Iwata, S. *J. Chem. Phys.* **1996**, *104*, 9058.

(26) Zhan, C. G.; Iwata, S. *J. Chem. Phys.* **1996**, *105*, 6578.

(27) Pascoli, G.; Lavendy, H. *Chem. Phys. Lett.* **1999**, *312*, 333.

(28) Xu, C. S.; Burton, G. R.; Taylor, T. R.; Neumark, D. M. *J. Chem. Phys.* **1997**, *107*, 3428.

(29) Metz, R. B.; Weaver, A.; Bradforth, S. E.; Kitsopoulos, T. N.; Neumark, D. M. *J. Phys. Chem.* **1990**, *94*, 1377.

(30) Osterwalder, A.; Nee, M. J.; Zhou, J.; Neumark, D. M. *J. Chem. Phys.* **2004**, *121*, 6317.

(31) Zhou, J.; Garand, E.; Neumark, D. M. *J. Chem. Phys.* **2007**, *127*, 9.

(32) Neumark, D. M. *J. Phys. Chem. A* **2008**, *112*, 13287.

(33) Eppink, A.; Parker, D. H. *Rev. Sci. Instrum.* **1997**, *68*, 3477.

(34) Even, U.; Jortner, J.; Noy, D.; Lavie, N.; Cossart-Magos, C. *J. Chem. Phys.* **2000**, *112*, 8068.

(35) Garand, E.; Yacovitch, T. I.; Neumark, D. M. *J. Chem. Phys.* **2009**, *130*, 7.

(36) Wiley, W. C.; McLaren, I. H. *Rev. Sci. Instrum.* **1955**, *26*, 1150.

(37) Chandler, D. W.; Houston, P. L. *J. Chem. Phys.* **1987**, *87*, 1445.

(38) Hansen, E. W.; Law, P. L. *J. Opt. Soc. Am. A-Opt. Image Sci. Vis.* **1985**, *2*, 510.

(39) Miller, F. A.; Lemmon, D. H. *Spectrochim. Acta A-Molec. Spec.* **1967**, *A 23*, 1415.

(40) Markovich, G.; Giniger, R.; Levin, M.; Cheshnovsky, O. *J. Chem. Phys.* **1991**, *95*, 9416.

(41) Cooper, J.; Zare, R. N. *J. Chem. Phys.* **1968**, *48*, 942.

(42) Reid, K. L. *Annu. Rev. Phys. Chem.* **2003**, *54*, 397.

(43) Duschinsky, F. *Acta Physicochim. URSS* **1937**, *7*, 551.

(44) Ervin, K. M.; Ho, J.; Lineberger, W. C. *J. Chem. Phys.* **1989**, *91*, 5974.

(45) Ervin, K. M.; Ramond, T. M.; Davico, G. E.; Schwartz, R. L.; Casey, S. M.; Lineberger, W. C. *J. Phys. Chem. A* **2001**, *105*, 10822.

(46) Ervin, K. M. PESCAL (FORTRAN), 2001.

(47) Hutchisson, E. *Phys. Rev.* **1930**, *36*, 0410.

(48) Becke, A. D. *J. Chem. Phys.* **1993**, *98*, 1372.

(49) Lee, C. T.; Yang, W. T.; Parr, R. G. *Phys. Rev. B* **1988**, *37*, 785.

(50) Dunning, T. H. *J. Chem. Phys.* **1989**, *90*, 1007.

(51) M. J. Frisch; G. W. Trucks; H. B. Schlegel; et al. GAUSSIAN 03; Revision C.02 ed.; Gaussian, Inc.: Wallingford, CT, 2004.

(52) Zhou, J.; Garand, E.; Neumark, D. M. *J. Chem. Phys.* **2007**, *127*, 154320.

TABLES

Table 6.1.

	SEVI				
Peak	Energy (eV)	β	Displacement from X_0 (in cm^{-1})	Assignment	
d	4.273	0.6±0.1	-258	4_2^2	$\tilde{X}\ ^2\Sigma^+ \leftarrow \tilde{X}\ ^1\Sigma^+$
c	4.281	0.6±0.1	-194	$4_1^1 5_1^1$	
b	4.289	0.6±0.1	-129	4_1^1	
a	4.296	0.6±0.1	-73	5_1^1	
X_0	4.305	0.5±0.1	0	0_0^0	
X_1	4.339	0.5±0.1	274	5_0^2	

Peak positions in eV, anisotropy parameters, displacement of peaks from X_0, and vibrational and electronic assignments for the SEVI spectrum of C_3N^- taken at 283 nm. Vibrational modes: $\nu_1(\sigma)$ pseudosym stretch, ν_2 (σ) pseudoasym stretch, ν_3 (σ) middle C-C stretch, ν_4 (π) cis bend, ν_5 (π) trans bend.

Table 6.2.

		TOF-PE		
Peak	Energy (eV)	β	Displacement from A (in cm^{-1})	Tentative Assignment
A	4.45	0.2±0.1	0	0_0^0 $\tilde{X}\ ^2\Sigma^+$ <-- $\tilde{X}\ ^1\Sigma^+$
B	4.52	0±0.1	565	0_0^0 $\tilde{X}\ ^2\Sigma^+$ <-- $\tilde{A}\ ^2\Pi$
C	4.76	0±0.1	2500	3_0^1 $\tilde{X}\ ^2\Sigma^+$ <-- $\tilde{A}\ ^2\Pi$
D	4.80	0±0.1	2823	1_0^1 $\tilde{X}\ ^2\Sigma^+$ <-- $\tilde{A}\ ^2\Pi$

Peak positions in eV, angular distributions (PAD), displacement of peaks from A, and vibrational and electronic assignments for the TOF-PE spectrum of C_5N^- taken at 213 nm.

Table 6.3.

C_3N species		$r(C_1C_2)$	$r(C_2C_3)$	$r(C_3N)$	$\nu_1(\sigma)$	$\nu_2(\sigma)$	$\nu_3(\sigma)$	$\nu_4(\pi)$	$\nu_5(\pi)$
$^1\Sigma^+$ (anion)	CCSD(T)/aug-cc-pCV5Z (empirically corr.) [a]	1.252	1.366	1.171					
	CCSD(T)/aug-cc-pVQZ [a]				2210	1965	876	533	203
	expt. SEVI [b]	-	-	-	-	-	-	$538^{\pm}8$	$208^{\pm}8$
$^2\Sigma^+$ (neutral)	CASSCF [c]	1.217	1.388	1.160	-	-	-	-	-
	CEPA-1 (112cGTOs) [d]	1.214	1.385	1.162	$2280^{\pm}15$	$2090^{\pm}15$	$883^{\pm}15$	-	-
	RCCSD(T)/rec.[e **]	1.210	1.377	1.160	-	-	-	-	-
	RCCSD(T)/val [f]	-	-	-	2312	2117	885	414	147
	RCCSD/all+(T)/val / cc-pVQZ [f]	1.210	1.377	1.160	-	-	-	-	-
	RCCSD(T)/val/cc-pVTZ + expt.[f]	1.212	1.375	1.161	-	-	-	-	-
	expt. LIF [g]	-	-	-	-	-	1054	405	131

** recommended equilibrium structures based on calculations involving RCCSD(T)

[a]Reference 14
[b]This work
[c]Reference 19
[d]Reference 18
[e]Reference 23
[f]Reference 16
[g]Reference 11

Calculated geometries and vibrational frequencies of C_3N^- anion and C_3N radical from current and previous calculations and experiment. Vibrational modes: $\nu_1(\sigma)$ pseudosym stretch, $\nu_2(\sigma)$ pseudoasym stretch, $\nu_3(\sigma)$ middle C-C stretch, $\nu_4(\pi)$ cis bend, $\nu_5(\pi)$ trans bend. All frequencies except for the CEPA-1 (112cGTOs) of the $^2\Sigma^+$ state are harmonic frequencies.

Table 6.4.

Transition	ΔE(eV)	Method
$\tilde{X}\,^1\Sigma^+$ --> $\tilde{X}\,^{\Sigma^+}$ *	4.344 **	RCCSD(T)/aug-cc-pV5Z [a]
	4.59±0.25	expt. dissociative attachment [f]
	4.305±0.001	expt. SEVI [b]
$\tilde{X}\,^2\Sigma^+$ --> $\tilde{A}\,^2\Pi$	0.229 (1844 cm^{-1})	expt. LIF [c]
	0.267 (2150±150 cm^{-1})	RCCSD(T)/cc-pVTZ [d]
	0.186 (1500±50 cm^{-1})	CASSCF (148cGTOs)[e]
$\tilde{A}\,^2\Pi$ --> $\tilde{B}\,^2\Pi$	3.463 (27929.985cm^{-1})	expt. LIF [c]

[a]Reference 14
[b]This work
[c]Reference 11
[d]Reference 16
[e]Reference 18
[f]Reference 17

Calculated and experimental transition energies between selected states of the C_3N anion and neutral. Transitions marked with an asterisk can be observed in the photoelectron spectra; the remaining ones are neutral-neutral transitions. Numbers marked with a double asterisk are equilibrium energies; the unmarked ones are adiabatic energies.

Table 6.5.

* With the image size constraints, this table may be too small to read; I included a bigger copy of this table laid out in landscape mode on page 22

C_5N species		$r(C_1C_2)$	$r(C_2C_3)$	$r(C_3C_4)$	$r(C_4C_5)$	$r(C_5N)$	$\nu_1(\sigma)$	$\nu_2(\sigma)$	$\nu_3(\sigma)$	$\nu_4(\sigma)$	$\nu_5(\sigma)$	$\nu_6(\pi)$	$\nu_7(\pi)$	$\nu_8(\pi)$	$\nu_9(\pi)$
$^1\Sigma^+$ (anion)	CCSD(T)/vqz+** [a]	1.258	1.345	1.231	1.357	1.170	2236	2156	1951	1179	620	503	494	227	97
	expt. Far-UV irradiation of cyanodiacetylene (HC_5N) in solid argon [d]	-	-	-	-	-	2184	2111	1923	-	-	-	-	-	-
	B3LYP/aug-cc-pVTZ [b]	1.253	1.337	1.230	1.349	1.168	2275	2204	2001	1214	638	551	521	253	107
$^2\Sigma^+$ (neutral)	RCCSD(T)/180 cGTOs [c]	1.214 *	1.366 *	1.212 *	1.371 *	1.161 *	2319	2226	2098	1163	612	-	-	-	-
	RCCSD(T)/rec.[e] ***	1.214	1.365	1.212	1.371	1.162	-	-	-	-	-	-	-	-	-
	B3LYP/aug-cc-pVTZ [b]	1.209	1.355	1.211	1.361	1.157	2342	2275	2158	1206	634	543	1254	332	121
$^2\Pi$ (neutral)	RCCSD(T)/180 cGTOs [c]	1.296 *	1.328 *	1.229 *	1.362 *	1.164 *	-	-	-	-	-	-	-	-	-
	RCCSD(T)/rec.[e] ***	1.296	1.328	1.230	1.362	1.164	-	-	-	-	-	-	-	-	-
	B3LYP/aug-cc-pVTZ [b]	1.286	1.313	1.236	1.345	1.163	2215	2108	1906	1205	638	-	-	-	-

** cc-pVQZ at all atoms plus the diffuse s, p, d, f, g functions from the aug-cc-pVQZ for the terminal atoms
*** recommended equilibrium structures based on calculations involving RCCSD(T)

[a]Reference 9
[b]This work
[c]Reference 7
[d]Reference 23
[e]Reference 21

Calculated geometries and vibrational frequencies of C_5N^- anion and C_5N radical from current and previous calculations and experiment. Vibrational modes: $\nu_1(\sigma)$, $\nu_2(\sigma)$, $\nu_3(\sigma)$, $\nu_4(\sigma)$, $\nu_5(\sigma)$ are the various active stretching modes, while $\nu_6(\pi)$, $\nu_7(\pi)$, $\nu_8(\pi)$ and $\nu_9(\pi)$ are the active bending modes for the linear molecules. All frequencies calculated are harmonic frequencies. Bond lengths marked with an asterisk are empirically corrected values.

Table 6.6.

Transition	$^{\Delta}$E(eV)	Method
$\tilde{X}\,^{1}\Sigma^{+}$ --> $\tilde{X}\,^{2}\Sigma^{+}$ *	4.453 **	RCCSD(T)/234 cGTOs
	4.45±0.03	expt. TOF-PE [b]
$\tilde{X}\,^{2}\Sigma^{+}$ --> $\tilde{A}\,^{2}\Pi$	0.062 (500 cm^{-1}) **	CCSD(T)/cc-pVTZ [a]
	560±120 cm^{-1}	expt. TOF-PE [b]

[a]Reference 7
[b]This work

Calculated and experimental transition energies between selected states of the C_5N anion and neutral. Transitions marked with an asterisk can be observed in the photoelectron spectra; the remaining ones are neutral-neutral transitions. Numbers marked with a double asterisk are equilibrium energies; the unmarked ones are adiabatic energies.

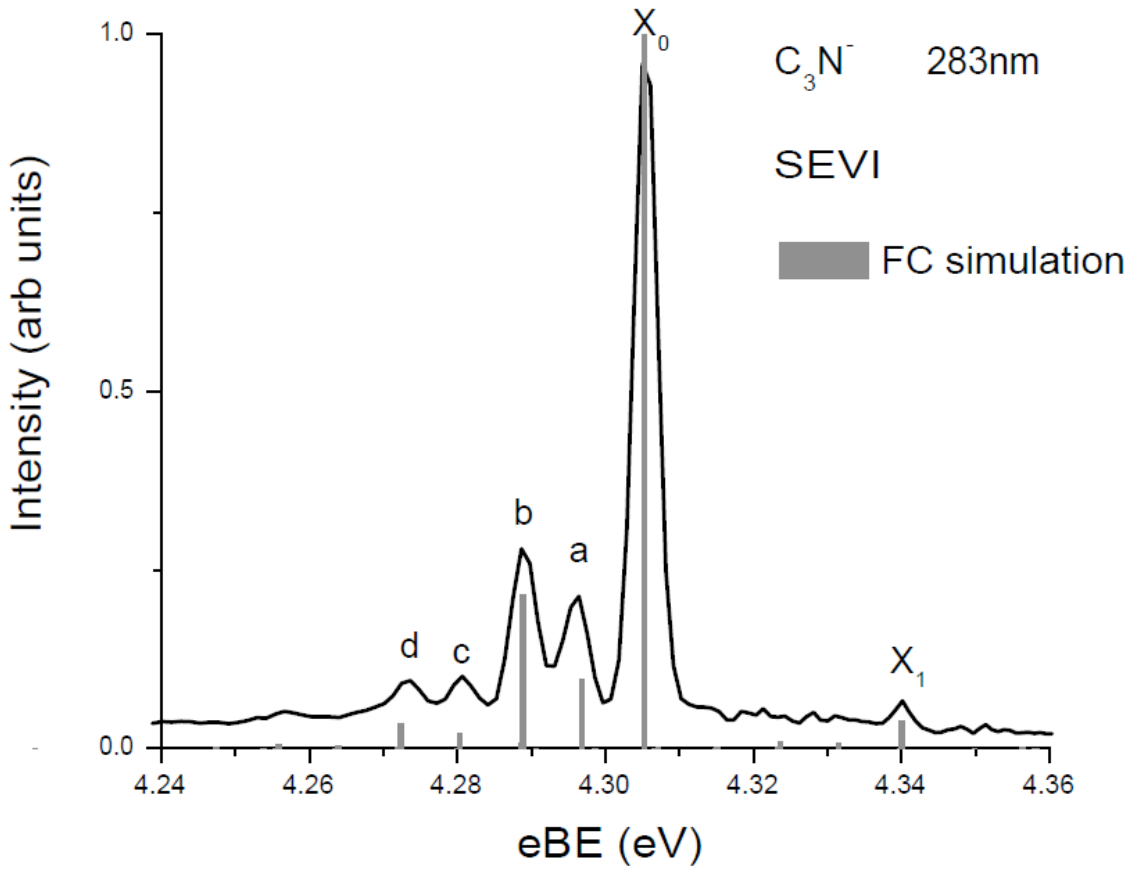

FIGURE 6.1 SEVI photoelectron spectrum of C_3N^- at 283 nm (4.382 eV) and plotted in eBE. Overlapped with the spectrum is the Franck-Condon simulation of the peaks in gray.

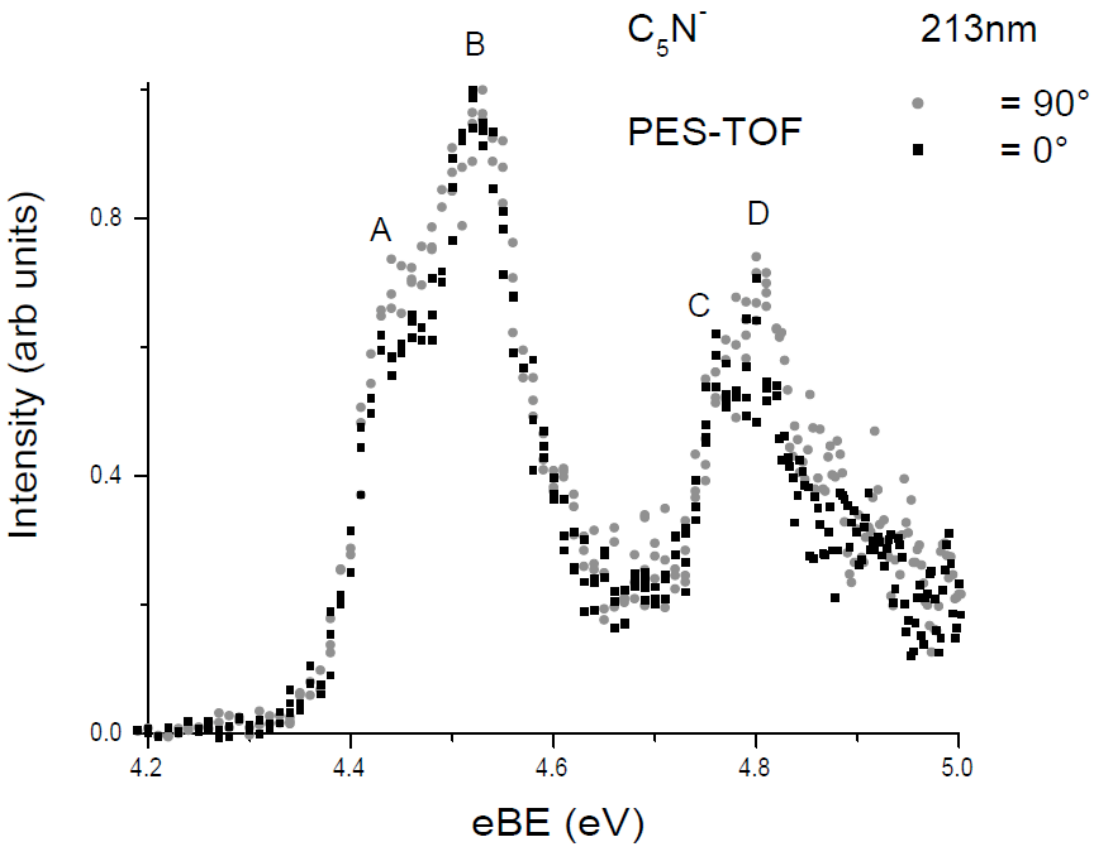

FIGURE 6.2 TOF-PE spectra of C_5N^- at 213 nm (5.822 eV) plotted in eBE. The trace and trace are taken at laser polarization angles of 0° and 90° respectively.

C_5N species		$r(C_1C_2)$	$r(C_2C_3)$	$r(C_3C_4)$	$r(C_4C_5)$	$r(C_5N)$	$\nu_1(\sigma)$	$\nu_2(\sigma)$	$\nu_3(\sigma)$	$\nu_4(\sigma)$	$\nu_5(\sigma)$	$\nu_6(\pi)$	$\nu_7(\pi)$	$\nu_8(\pi)$	$\nu_9(\pi)$
$^1\Sigma^+$ (anion)	CCSD(T)/vqz+** [a]	1.258	1.345	1.231	1.357	1.170	2236	2156	1951	1179	620	503	494	227	97
	expt. Far-UV irradiation of cyanodiacetylene (HC_5N) in solid argon [d]	-	-	-	-	-	2184	2111	1923	-	-	-	-	-	-
	B3LYP/aug-cc-pVTZ [b]	1.253	1.337	1.230	1.349	1.168	2275	2204	2001	1214	638	551	521	253	107
$^2\Sigma^+$ (neutral)	RCCSD(T)/180 cGTOs [c]	1.214 *	1.366 *	1.212 *	1.371 *	1.161 *	2319	2226	2098	1163	612	-	-	-	-
	RCCSD(T)/rec.[e] ***	1.214	1.365	1.212	1.371	1.162	-	-	-	-	-	-	-	-	-
	B3LYP/aug-cc-pVTZ [b]	1.209	1.355	1.211	1.361	1.157	2342	2275	2158	1206	634	543	1254	332	121
$^2\Pi$ (neutral)	RCCSD(T)/180 cGTOs [c]	1.296 *	1.328 *	1.229 *	1.362 *	1.164 *	-	-	-	-	-	-	-	-	-
	RCCSD(T)/rec.[e] ***	1.296	1.328	1.230	1.362	1.164	-	-	-	-	-	-	-	-	-
	B3LYP/aug-cc-pVTZ [b]	1.286	1.313	1.236	1.345	1.163	2215	2108	1906	1205	638	-	-	-	-

** cc-pVQZ at all atoms plus the diffuse s, p, d, f, g functions from the aug-cc-pVQZ for the terminal atoms
*** recommended equilibrium structures based on calculations involving RCCSD(T)

[a]Reference 9
[b]This work
[c]Reference 7
[d]Reference 23
[e]Reference 21

Table 6.5 (magnified)

Appendix 1

Summing program used in generation of 118.2 nm

```
#include <stdio.h>

main( int argc, char *argv[] )
{
 FILE *ifp;
 char *mode = "r";

 int count;
 float sum = 0.00;

 if( argc == 2 ) //name of program is 1, name of file is 2
 {
  ifp = fopen(argv[1], mode);
  if (ifp == NULL)
   {
    fprintf(stderr, "Can't open input file\n");
    exit(1);
   }

 while(fscanf(ifp, "%d", &count)!= EOF)
   {
   sum = sum + count;
   }
 }
 else if( argc > 2 )
  { printf( "Too many arguments provided\n" ); }
 else
  { printf( "Please specify a filename\n" ); }

 printf(argv[1]);
 printf(" sum = %f\n", sum, "\n");
 fclose(ifp);

}
```